CHAPTER 1

INTRODUCTION

Overview

Breast cancer is a major and important disease with heavy clinical and personal burden. This year alone the predicted number of new breast cancer cases in the United States will reach a record high of approximately 200,000 individuals, and despite the decline in overall mortality from breast cancer, approximately 20% of those diagnosed will succumb to the disease (Jemal et al., 2009). In view of this high statistic, there are pressing needs that must be addressed in breast cancer research including: the need for appropriate models to study, the need for continued molecular understanding of the disease, and the need for *in vivo* imaging to follow cellular and metabolic processes at the molecular level.

While there are many models currently employed, mice carrying the mouse mammary tumor virus (MMTV) have served as one of the oldest and most established models for human breast cancer (Cardiff and Kenney, 2007). MMTV is a transforming retrovirus that causes mammary tumorigenesis in mice which can be inherited as an endogenous retrovirus through the germline or acquired exogenously via transmission through the milk (Ross, 2008). There has been extensive analysis of the molecular genetics of the virus and the mechanisms underlying tumorigenesis for the last seventy years. However, despite its importance as a model, there has been relatively little done to address the physiological and metabolic progression of these mammary tumors,

particularly in an *in vivo* context (Gabrielson et al., 2008). The advent of *in vivo* imaging allows us to address these important issues of longitudinal monitoring of molecular processes for this key and often utilized model.

Here we use *in vivo* gamma imaging with radioiodine combined with molecular biology assays targeting the sodium iodide symporter (NIS) to address specific questions: 1.) Do MMTV tumors display a unique radioiodine metabolic pattern? 2.) Does the presence of a mammary tumor influence other aspects of physiology/metabolism? Many have shown that NIS, the protein that facilitates radioiodine transport into cells, is upregulated in the majority of human and transgenic mouse mammary cancers (Knostman et al., 2004; Renier et al., 2009; Tazebay et al., 2000; Wapnir et al., 2003). Based upon these data, we hypothesize that there will be unique radioiodine accumulation patterns that are associated with NIS expression and that the metabolism of radioiodine in other tissues will be affected due to the presence of a tumor.

Epidemiology and Molecular Biology of Breast Cancer

Risk factors that have been associated with breast cancer development include early age at menarche, low birth rate, infertility, and advanced age at menopause (all reviewed in Cetin et al. (2008)). Additionally, greater breast density (Boyd et al., 2009), advanced age (Crivellari et al., 2007), obesity and increased circulating endogenous estrogens (reviewed in Cleary and Grossmann (2009)), and environmental factors, such as smoking at an early age (Ha et al., 2007) have also been linked with increased breast cancer risk.

Two genes, BRCA1 and BRCA2, are associated with “high risk” breast cancer

susceptibility, but mutations in these genes are rare and account for only 10% of breast cancer cases (Metcalfe, 2009). Current evidence suggests that along with mutated versions of the BRCA1 and BRCA2 genes, concomitant mutations in "low risk" breast cancer susceptibility genes, like checkpoint kinase (CHEK2), have been shown to double an individual's risk of breast cancer (Nevanlinna and Bartek, 2006).

The amplification of the c-Myc transcription factor has been linked to breast cancer because of its ability to regulate transcription of up to 15% of all genes (Bouchalova et al., 2009). Likewise, other molecular targets that are frequently associated with increased breast cancer risk include: mutation and overexpression of ras (Pylayeva et al., 2009) and src (Jin et al., 2008) signaling pathways, the inactivation of p53 (Golubovskaya et al., 2009) and overexpression of cyclin D1 (Butt et al., 2008), both of which control the cell cycle, and the loss of the adhesion molecule E-cadherin (Baranwal and Alahari, 2009).

Estrogen receptor-α (ERα), progesterone receptor (PR) and human epidermal growth factor receptor-2 (HER2/ErbB2) are the only biomarkers that are currently used for testing in breast biopsies in order to determine therapy options (Geyer et al., 2009). ERα and PR are both steroid receptors that when bound to their respective hormones become activated and bind as dimers to steroid responsive elements on the DNA to regulate gene transcription (Wei et al., 2009). ERα and PR breast cancer expression have been reported at higher levels in male breast cancer (90%) compared to female (75%) (Robinson et al., 2008). HER2 is an epidermal growth factor receptor tyrosine kinase that is expressed in approximately 30% of breast cancers (Pritchard et al., 2008). In clinical applications the receptor status of these three biomarkers is used as a tool to predict

treatment methods (tamoxifen for ERα and PR or trastuzumab for HER2) and long-term prognosis. In general, ERα and PR positive and HER2 negative breast cancers are more easily treated because they will respond to hormone therapy. HER2 positive cancers are harder to treat because of drug resistance, and ERα, PR, and HER2 negative tumors are some of the most aggressive with the poorest overall prognosis (Geyer et al., 2009; Renier et al., 2009).

Amphiregulin (AREG) is a member of the epidermal growth factor family that activates epidermal growth factor receptor (EGFR) related receptors such as HER2. In the normal mammary gland AREG has been shown to be critical for the outgrowth of mammary ducts into the fat pad (Lamarca and Rosen, 2007; Lawson, 2009). In breast cancer, ER-positive status has an influence on the expression of AREG. It has been reported that AREG mRNA is expressed in as much as 58% of breast carcinomas (Normanno et al., 1995). AREG has also been linked to breast cancer progression. Increased expression of AREG mRNA and protein were found in the tumors of four transgenic mice strains, such as HER2, which suggested that AREG had a role in tumor progression (Kenney et al., 1996).

Hypoxia-Inducible Factor-1 alpha (HIF-1α) is a transcription factor responsible for the cellular response to hypoxia. There are two subunits comprising the transcription factor, HIF-1α and HIF-1β (Kronblad et al., 2006). HIF-1β is constitutively expressed, but HIF-1α is degraded under normoxic conditions and during hypoxia it dimerizes with HIF-1β in order to bind to hypoxic responsive elements on the DNA to regulate gene transcription. HIF-1 complex has been shown to regulate genes involved with angiogenesis, glycolysis, cell survival and cell invasion (Semenza, 2003). In the

involuting mammary gland, mRNA hierarchal clustering analysis has been used to cluster genes into finite groups based on the time they are activated during the regression of the mammary gland post-weaning. This analysis identified the most overexpressed genes during involution were those with HIF-1 promoter binding sites, which suggests pathways involved with metastasis are activated during this time (Stein et al., 2009). HIF-1α can also be overexpressed in breast cancer. Kronblad et al. (2006) have demonstrated that poor prognosis and ultimately death in breast cancer is correlated with HIF-1α overexpression. Recently, HIF-1α overexpression in a transgenic model was not sufficient to induce mammary tumor growth, but it plays a role in tumor metastasis (Liao et al., 2007). Viola et al. (2008) have reported detecting the increase in HIF-1α expression in transplanted breast carcinomas.

Breast Cancer Models

Transgenic Models of Breast Cancer

An objective in the design of transgenic genetically engineered mouse (GEM) models has been to better understand the molecular mechanisms driving mammary tumorigenesis and progression especially as it may relate to human disease. The histopathology of most GEM models of breast cancer do not appear to resemble spontaneous tumors induced by the mouse mammary tumor virus or chemical carcinogens (Cardiff et al., 2000a), but GEM tumors do closely resemble human breast cancers especially in premalignant ductal carcinoma *in situ* (Cardiff and Wellings, 1999; Maglione et al., 2001). Although GEM and human tumors can have morphological similarity, the tumor biology of these species is different. These differences are evident

with regard to tumor composition, cell type, estrogen receptor status, and site of metastasis (reviewed in Marcotte and Muller (2008)). Nevertheless, transgenic models that imitate components of human breast cancer have and will continue to be useful tools for studying mammary tumorigenesis.

The development of transgenic mammary tumor models has employed promoter regions of the mouse mammary tumor virus (MMTV) long terminal repeat, Beta-lactoglobulin (BLG), C3 promoter, or the whey acidic protein (WAP) fused to oncogenes of interest to target mammary epithelia for expression (reviewed in Cardiff et al. (2000b)). These promoters are hormone responsive and generally require multiple pregnancy/lactation cycles in order to get significant transgene expression in the mammary glands. Transgenic models commonly employed for studying how disregulated pathways initiate and promote mammary tumorigenesis include: MMTV-TGFα, transforming growth factor α (growth factors), MMTV-ErbB2/neu, epidermal growth factor receptor (receptors), WAP-Int3, Notch (differentiation), MMTV-Myc (cell-cycle), and MMTV-PyVT, polyomavirus middle T antigen (signal transduction) (reviewed in Cardiff et al. (2000b) and Marcotte and Muller (2008)).

Currently, the MMTV-polyoma middle T antigen (PyVT) mouse is extensively used in breast cancer research because of the model's rapid tumor development and its metastatic ability. In the PyVT MT#634 mouse line, by three weeks of age multiple premalignant adenocarcinomas were detected; by five weeks of age highly fibrotic tumors developed in the entire mammary fat pad which inhibited lactation; by three months of age 94% of tumor-bearing females developed multiple metastatic adenocarcinoma foci of mammary origin in the lungs (Guy et al., 1992). At the molecular

level, PyVT binds and activates signal transduction pathways involved with cell proliferation, migration, and apoptosis. Specifically, PyVT activates both the c-Src family of tyrosine kinases (Guy et al., 1994) and the phosphatidylinositol 3-kinase (PI3K) (reviewed in Vivanco and Sawyers (2002)) signaling pathways, which have been shown to be critical for tumor initiation, but inefficient to drive the malignant phenotype in PyVT animals (Maglione et al., 2001). Much has been done to describe the discrete stages of tumor progression in the PyVT model beginning with hyperplasias and ending with carcinomas. Maglione et al. (2001) identified that the pre-dominant premalignancy lesions found in PyVT mice were ductal carcinoma *in situ* (DCIS) which were tumorigenic in transplant studies and gave rise to metastatic lesions. In addition, Lin et al. (2003) have reported that with PyVT tumor progression, there is a steady loss in estrogen and progesterone receptors and an overexpression of the ErbB2/neu receptor.

MMTV Model

Beginning in 1936, Dr. John Bittner demonstrated that viremic dams from mouse strains with high mammary tumor incidence secreted a "milk factor" causally associated with tumorigenesis both in progeny and in fostered pups from low incidence strains. These data along with later work suggested that the etiology of the maternal tumorigenic contribution stemmed from an infectious virus called the mouse mammary tumor virus (MMTV) (reviewed in Cardiff and Kenney (2007)). MMTV is a murine B-type retrovirus incorporating its DNA as a provirus into the genome of infected host cells. The infectious insertion of MMTV viral DNA occurs in two forms: exogenous transmission from mother to pup or in rare events endogenous transmission through the germline (Callahan and Smith, 2000).

Horizontal transmission of exogenous MMTV begins following pup ingestion of infected milk from viremic dams exposing MMTVs to B cell lymphocytes traveling through Peyer's patches in the gut. Subsequent incorporation of the exogenous provirus into B lymphocyte genomes trigger the expression of the MMTV sag gene encoding a superantigen (Acha-Orbea and MacDonald, 1995) in the long terminal repeat (LTR) sequence, which stimulates the recruitment and proliferation of MMTV infected T cell lymphocytes with Vβ receptors (Beutner et al., 1994). Infected lymphocytes expose MMTVs to neonatal mammary gland epithelia leading to viral quiescence. The exact mechanism for virion binding to the host is unknown, but cell-to-cell interaction (Callahan and Smith, 2000) or interaction with acidic receptors such as mouse transferrin receptor 1 (Ross et al., 2002) are the prime candidates.

Recently, studies have suggested that because MMTV tumors are clonal the initial viral infection targets mammary precursor/stem cells which can differentiate into all mammary epithelia cell types (Callahan and Smith, 2008; Medina, 2005). Dormancy is interrupted during puberty when under hormone regulation mammary epithelia begin to proliferate forming the ductal structures of the breast. Once again the proviral LTR encodes mammary specific enhancers (Mink et al., 1992; Mok et al., 1992) or hormone response elements interacting with glucocorticoids, androgens and progesterone/prolactin during pregnancy (reviewed in Gunzburg and Salmons (1992)) to stimulate MMTV virion production and infection of new mammary epithelia. Estrogen does not specifically affect expression of viral DNA (Bocchinfuso et al., 1999; Otten et al., 1988), but there is a positive correlation with estrogen activity and MMTV virus levels (Bradlow et al., 1985).

As the MMTVs continue to infect mammary epithelia, tumorigenesis occurs via insertional mutagenesis constitutively activating adjacent proto-oncogenes (Theodorou et al., 2007). During oncogenesis MMTVs activate a wide range of ectopic genes not normally expressed in the mammary gland such as Wnt1/Int1 (Nusse et al., 1984), Fgf3/Int2 (Mester et al., 1987; Shackleford et al., 1993), and Notch4/Int3 (Politi et al., 2004; Uyttendaele et al., 1996), which have been shown to act in combination with one another to promote tumorigenesis (Mester et al., 1987). Furthermore, MMTVs activate genes involved with Wnt, MAPK, Notch, Hedgehog, FGF, and EGF signaling pathways (Callahan and Smith, 2008; Theodorou et al., 2007).

Many inbred mice strains and some feral mice have vertically transmitted or the endogenous MMTV provirus in their genomes acting under the constraints of Mendelian gene assortment (Michalides et al., 1981; Varmus et al., 1972). Compared with the exogenous form, endogenous MMTV is less virulent and rarely causes tumorigenesis (Ponta et al., 1985). Endogenous MMTV has also been shown to provide critical resistance to exogenous MMTV infection when the exogenous and endogenous viruses stimulate the same type of Vβ T cells (Beutner et al., 1994; Golovkina et al., 1997). Additionally, endogenous and exogenous MMTVs are secreted during lactation and have been shown to undergo recombination to mitigate virulence, though without the exogenous form the endogenous provirus is inert (Golovkina et al., 1994; Golovkina et al., 1997; Hook et al., 2000).

The MMTV model is currently used for breast cancer research because of the homology between murine and human development and maturation of mammary glands, as well as, the model's apparent spontaneous ability for tumor development (Cardiff and

Kenney, 2007; Cardiff and Wellings, 1999). Like the majority of human breast cancers, spontaneous MMTV tumors are estrogen receptor positive compared to transgenic breast cancer mouse models whose tumors are overwhelmingly estrogen receptor negative (Kordon, 2008). MMTV study also offers insight into viral tumorigenesis that may be linked to some human breast cancers (Lawson et al., 2001), though the data remains equivocal (Lawson, 2009). MMTV-infected mouse models have also been used to describe the effect that endocrinology, viruses, signaling and oncogenes have on neoplastic progression (reviewed in Cardiff and Kenney (2007)).

In Vivo Imaging of Breast Cancer

Early detection, diagnosis, and treatment of breast cancer provide the best survival strategy against the disease (Prasad and Houserkova, 2007). Imaging modalities such as mammography and magnetic resonance imaging (MRI) are most widely employed for breast cancer screening and early detection in the clinical setting. While these technologies provide critical anatomical information about lesion location, they lack the capacity to convey any functional information (Bartella et al., 2007). Implementing functional imaging modalities, such as positron emission tomography (PET) and single photon emission computed tomography (SPECT), would complement current screening technologies because of the added information about the biology of the tumor (Culver et al., 2008).

Mammography

Mammography remains the most widely employed method for screening and diagnosing breast cancer throughout the world (Skaane, 2009). This detection modality

uses a controlled amount of ionizing X-rays to record breast density variation as the radiation waves pass through the tissues (Matveeva et al., 2009). The image produced from this screen can identify dense masses within the breast tissue that would appear abnormal and warrant further testing. Currently, many clinics are shifting from the standard screen-film mammography to full-field digital mammography which has been shown to be just as effective at breast screening (Skaane, 2009; Vinnicombe et al., 2009). However, since the effectiveness of mammography relies on lower breast density for abnormal mass detection, more dense breasts are difficult to accurately screen. This diagnostic problem can lead to false positive or inappropriate negative results, although it has recently been shown that breasts with a density of 75% have a higher likelihood of cancer development (Boyd et al., 2009). While mammography is reliable at detecting anatomical anomalies within the breast, it does not convey any type of functional information about putative tumors.

Magnetic Resonance Imaging

MRI is an imaging modality with excellent spatial resolution for anatomical imaging and is used in adjunct to mammography. MRI now possesses potential functional imaging capability, but lacks any molecular or metabolic information (Prasad and Houserkova, 2007). With the aid of radiowaves, a MRI scan measures the protons in water and can distinguish between tissue types based on differences in water concentrations (Lyons, 2005). In addition, dense areas with higher blood supply are more easily imaged with MRI. In many cases contrast agents containing gadolinium are used to enhance image quality (Mortellaro et al., 2009).

Although in the clinical setting MRI remains primarily used for anatomical scans, new advances are coming to the forefront. Specifically in breast cancer imaging studies, MRI not only provides anatomical information, but also has showed promise in functional analysis. MRI has been shown to detect choline in breast cancers that is generally undetectable in normal breast tissue (Tozaki, 2008). Differences between imaging kinetics of choline detection in estrogen receptor (ER) positive and negative breast cancers have been evaluated (Chen et al., 2008). Additionally, MRI was shown to have greater ability at detecting lesions in older patients with HER2 receptor negative breast cancers (Moon et al., 2009). MRI has also been employed for axillary lymph node monitoring for possible metastasis since lymph nodes of receptor negative breast cancers have been shown to be larger than receptor positive breast cancers (Mortellaro et al., 2009). However, despite these advances, MRI still has remained an anatomical tool for detecting breast lesions without any functional information about the tumor metabolism.

Positron Emission Tomography

Positron emission tomography (PET) has become the primary modality for functional and molecular imaging using positron-emitting radioisotopes, such as ^{15}O, ^{13}N, ^{11}C, and ^{18}F (Benard and Turcotte, 2005). The most utilized radiotracer for PET is 2-Deoxy-2-[^{18}F] fluoro-D-glucose (^{18}F-FDG), which can detect elevated glucose metabolism in breast cancer (Almubarak et al., 2009). Briefly, the mechanism behind ^{18}F-FDG breast cancer imaging involves the glycolytic pathway. Within cancer cells ^{18}F-FDG is phosphorylated by hexokinase into ^{18}F-FDG -6-phospate, and from this point ^{18}F-FDG -6-phosphate can neither be released from cells nor further broken down for metabolism. In practice, breast cancer cells have a higher glycolytic rate than

surrounding normal tissue which PET can detect due to greater positron emission (Lavayssiere et al., 2009).

In contrast with imaging modalities, such as mammography or MRI, PET provides *in vivo* functional information about the differences between normal and tumor glucose metabolism. This functional application for PET has led to studies correlating ^{18}F-FDG uptake with other tumor parameters, such as HER2 (Dijkers et al., 2009), ER and PR receptor status (Basu et al., 2008; Mavi et al., 2007), tumor size (Buck et al., 2002), and tumor histology (Mavi et al., 2006). Small animal PET imaging with ^{18}F-FDG has also been demonstrated as a useful tool for longitudinal monitoring of mammary tumor development in transplant studies (Abbey et al., 2006). In addition, small animal PET imaging has become a useful tool to target angiogenesis (Chen et al., 2004), and examine both tumor treatment response (Kesner et al., 2007) and therapy options (Aliaga et al., 2007; Hsueh et al., 2006; Parry et al., 2009).

However, despite the increasing number of radiotracers that have been evaluated for PET imaging, such as targeting estrogen (^{18}F-fluoroestradiol (Dehdashti et al., 2009; Peterson et al., 2008)) or treatment options with 4-[^{18}F]fluoropaclitaxel (Hsueh et al., 2006; Kurdziel et al., 2007), in all clinical applications ^{18}F-FDG is used. Therefore, there is a need for other PET radiotracers for general imaging applications (Ballinger, 2008). PET tracers also have very short half-lives and require a cyclotron to produce the complicated radiochemistry (Rahmim and Zaidi, 2008). False negative results can occur due to the poor resolution of PET to detect both low ^{18}F-FDG accumulation in lobular carcinomas and small tumors (0.4-1.5 cm) (Benard and Turcotte, 2005; Zytoon et al., 2008). False positive results can occur with PET in benign inflammations and

fibroadenomas of the breast. Multiple studies have demonstrated that lesions with higher concentrations of inflammatory cells, such as neutrophils and activated macrophages, also have elevated ^{18}F-FDG uptake, which can be misdiagnosed as malignancy in patients with proven or suspected cancer (Fenchel et al., 2002; Zhung and Alavi, 2002). While PET imaging with ^{18}F-FDG provides greater *in vivo* functional applications, limitations on tracer availability, specificity, and resolution require have opened the door to other imaging techniques with gamma emitters.

Scintimammography / Single Photon Emission Computed Tomography (SPECT)

As with PET, scintimammography (including planar and SPECT) relies on gamma ray emitting tracers, such as ^{99m}Tc-sestamibi, ^{123}I, ^{125}I, and ^{131}I, tagged to ligands for targeted molecular analysis. Compared with PET imaging, SPECT has lower sensitivity, but with the aid of pinhole collimators can achieve submillimeter spatial resolution (Mariani et al., 2008; Rowland and Cherry, 2008). Additionally, there are many commercially available iodinated ligands for targeted *in vivo* molecular imaging with SPECT (Weisenberger et al., 2003). The longer half-lives of isotopes used in SPECT are beneficial for longitudinal studies and for detecting slow biological processes (Rahmim and Zaidi, 2008).

In the clinical setting nuclear breast imaging via gamma cameras are employed with ^{99m}Tc-sestamibi because of increased sestamibi uptake in breast tumors compared with normal breast tissue (Gommans et al., 2007). Also there are conflicting reports on the usefulness of sestamibi washout as a predictor of poor chemotherapy response (Cwikla et al., 1999; Fuster et al., 2002; Tiling et al., 2004; Travaini et al., 2007). Currently, clinical gamma imaging is primarily used with equivocal mammograms due to

breast density (Zhou et al., 2008), and have been shown to have higher sensitivity at detecting occult breast lesions (Brem et al., 2008; Brem et al., 2007). The use of double gamma cameras has been shown to more accurately quantify lesion size and depth away from the collimator (Hruska and O'Connor, 2008).

SPECT imaging has been adapted for other targeted imaging of apoptosis markers (Kim et al., 2007a; Mandl et al., 2004), VEGF (vascular endothelial growth factor)(Collingridge et al., 2002), endoglin (Fonsatti et al., 2000), EGFR (Fernandes et al., 2007), anti-HER2 antibody (Orlova et al., 2007), and ER (Nayak et al., 2008). For small animal imaging studies there are now commercially available imaging devices dedicated to SPECT imaging, such as nanoSPECT (BioScan Inc.) (Garrood et al., 2009), X-SPECT (Gamma Medica Inc.) (Kim et al., 2007a) and U-SPECT-II (Molecular Imaging Laboratories) (van der Have et al., 2009). Recently, it has been shown that small animal SPECT imaging can be accomplished without the use of collimators and with a resolution of 7 mm (Mitchell and Cherry, 2009).

The transmembrane protein, sodium iodide symporter (NIS), has become a significant molecular target for SPECT imaging approaches due to its expression in organs such as the thyroid, stomach, lactating mammary glands, and in many human breast cancers (Carrasco, 1993; Dohan et al., 2006; Wapnir et al., 2004; Zuckier et al., 2001). NIS facilitates the transport of iodine into the cells in which it is expressed. Gamma ray emitting isotopes, such as radioiodine, can directly target the molecular expression and function of NIS (Zuckier et al., 2004). In addition to the utility of NIS for *in vivo* imaging, it has also been used as a target for gene therapy (Dadachova and Carrasco, 2004; Fan et al., 2004).

The Sodium Iodide Symporter and Breast Cancer

NIS is a transmembrane protein responsible for the cellular transport of iodine from the blood. NIS is primarily expressed in the thyroid for organification of thyroid hormones, but is also expressed in the gastric mucosa, lactating mammary glands and certain breast cancers (Spitzweg and Morris, 2002). Tazebay et al. (2000) were the first to establish in rats that lactating mammary glands had the specificity to accumulate ^{125}I compared to non-lactating rats. Physiologically, iodine secretion into the milk substrate has been shown to be critical for neonatal thyroid hormone development and storage, as well as, preventing impaired neurological development (Azizi and Smyth, 2009).

NIS Expression in Mouse Mammary Tumors

NIS expression and *in vivo* function, via scintigraphic imaging with ^{99m}Tc-pertechnetate, was first described in the Her-2/neu and v-Ha-ras transgenic mouse models (Tazebay et al., 2000). Research has shown that the polyomavirus middle T antigen (PyVT) mouse model has increased radioiodine uptake in mammary tumors when NIS mRNA expression was induced with all-trans retinoic acid (Kogai et al., 2004). NIS protein localization in breast cancer tissues has significant differences from the normal expression patterns in the basolateral surface of lactating alveolar cells. Knostman et al. (2004) identified endogenous NIS protein expression in the PyVT, MMTV-Cox-2, Ubi-hCGβ, and MMTV-neu transgenic mouse models. NIS in these transgenic samples was sometimes expressed on the plasma membrane and sometimes compartmentalized intracellularly. *In vivo* function of NIS was analyzed in PyVT mice using scintigraphy to

monitor tumor growth inhibition with radioiodine (^{131}I) and perrhenate ($^{188}ReO_4^-$) treatment (Dadachova et al., 2005).

NIS Expression in Human Breast Cancer

In human breast cancer NIS is expressed in many mammary carcinomas. Tazebay et al. (2000) found that 87% of invasive carcinomas, 83% of ductal carcinomas *in situ*, and 23% of noncancerous samples in the vicinity of the tumors expressed NIS protein. Next, a massive immunohistochemical study of 371 human breast cancer samples revealed that NIS was expressed in IHC 88% of ductal carcinomas, 76% of invasive carcinomas, and 87% of normal breast samples were negative (Wapnir et al., 2003). The high prevalence of NIS expression in mammary carcinomas compared with normal tissue overwhelming suggests that NIS could be used as a biomarker in this type of cancer. The current accepted biomarker for breast cancer, HER2, has very low (33%) positivity with this cancer type, which suggests that NIS positivity in tandem with isotope accumulation would be a sufficient biomarker in mammary carcinomas (Dohan et al., 2003). Recently, NIS expression has been identified in 65% of breast cancer samples that were negative for the three most common breast cancer markers, estrogen receptor (ER), progesterone receptor (PR), and HER2, further implicating the applicability of NIS as an efficient biomarker (Renier et al., 2009). Functional NIS has been evaluated using ^{99m}Tc-pertechnetate scintigraphy in human primary breast tumors and isotope accumulation was positively correlated with NIS mRNA levels (Moon et al., 2001; Upadhyay et al., 2003).

In the ER+ human breast cancer cell line, MCF-7, all-trans retinoic acid has been shown to induce NIS mRNA expression and radioiodine uptake (Kogai et al., 2004; Kogai et al., 2008). Others have indicated that enhanced induction of NIS expression is

accomplished with all-trans retinoic acid in addition to dextamethasone (Unterholzner et al., 2006; Willhauck et al., 2008). NIS activity and radioiodine accumulation have been stimulated by prostaglandins (PGE2), human chorionic gonadatropin (hCG), and phosphatidylinositol 3-kinase (PI3K) in MCF-7 cells. In contrast, cAMP, involved with NIS activity in the thyroid, stimulated NIS promoter activity but was not sufficient to induce radioiodine accumulation in MCF-7 cells (Knostman et al., 2004). Recently, studies have further found that PI3K in MCF-7 cells directly facilitates all-trans retinoic acid induction of NIS expression (Kogai et al., 2008; Ohashi et al., 2009). In the human ER- breast cancer cell line, MDA-MB-231, agents that have induced NIS expression in MCF-7 cells, such as all-trans retinoic acid and PI3K, do not effect NIS levels in this cell line (Knostman et al., 2007b; Kogai et al., 2004).

Current research suggests that there is a troubling disparity between the number of breast cancers that are positive for NIS protein versus their ability to accumulate any detectable radioiodine. Although up to 80% of human breast cancers have been shown to be positive for NIS (Wapnir et al., 2003), as few as 25% of these positive tumors have the ability functionally accumulate radioiodine in a manner useful for imaging or ablation with ^{131}I (Beyer et al., 2008). Many have observed that NIS localization in breast cancers is intracellular, which suggests impairment of cell surface trafficking. In the MCF-7 cell line, upregulation of NIS expression via the PI3K pathway has been shown to produce underglycosylated NIS which cannot be trafficked to the cell surface. In addition, PI3K activation of NIS has inhibited endogenous NIS expression and function at the cell membrane (Knostman et al., 2007b). Peyrottes et al. (2009) have designed and tested new

antibodies against NIS and have implied that the majority of intracellular NIS localization can be attributed to non-specific staining.

Goals of Project and Hypothesis

The goals of this work were to validate the efficacy of a novel second generation gamma camera (Bradley et al., 2006) as a high-performance imaging modality specifically for breast cancer research, and to address the need for *in vivo* imaging techniques which monitor the physiological and metabolic progression of mammary tumors. Specifically we wished to address important questions on MMTV biology: 1.) Do MMTV tumors display a unique radioiodine metabolic pattern? 2.) Does the presence of a mammary tumor influence other aspects of physiology/metabolism? The gamma camera was used to monitor the dynamic uptake of ^{125}I through the functional activity of NIS in spontaneous mammary tumors induced by the expression of the mouse mammary tumor virus (C3H/HeN MMTV+) as well as transgenic mammary tumors induced by the expression of the polyomavirus middle T antigen (FVB/N-Tg (MMTV-PyVT)^{634Mul}). Many studies have shown that in both human and transgenic mammary tumors NIS is upregulated (Knostman et al., 2004; Renier et al., 2009; Tazebay et al., 2000; Wapnir et al., 2003), and based upon these findings we hypothesize that in the MMTV model we can detect the unique ^{125}I accumulation patterns that provide information about where NIS protein is expressed. Additionally, based on other studies we hypothesize that the metabolism of ^{125}I in other tissues will be affected when a mammary tumor is present.

CHAPTER 2

MATERIALS AND METHODS

Animal Models

Mice (24-33 g body weight) six months and older were derived from the C3H/HeN MMTV+ strain (National Cancer Institute, Frederick, Maryland), and characterized by tumor development due to exogenous transmission of the MMTV virus. The C3H/HeN breeding founders were generously donated by Dr. Tatyana Golvkina. This study also integrated the smaller (22-29 g body weight) C57BL/J6 strain (Jackson Laboratory, Bar Harbor, ME) mice for comparative studies of radioiodide uptake in normal nulliparous, lactating, and multiparous mammary glands.

Heterozygous male FVB/N mice (National Cancer Institute, Frederick, Maryland) expressing the polyomavirus middle T antigen (FVB/N-Tg (MMTV-PyVT) ^{634Mul}) under the control of the mammary-specific mouse mammary tumor virus long terminal repeat promoter were bred with wild type females. Both wild type and heterozygous transgenic females (27-42 g body weight) five weeks and older were used for *in vivo* studies. For transgenic screening studies two groups of weaned pups, the first at 5 weeks old and the second at 7 weeks old, were selected at random from litters. Mice were screened for 10 minutes using the compact gamma camera fifty minutes after the radioiodine was administered. Mice were returned to their cage following imaging and later sorted into groups based on how they accumulated radioiodine.

All murine studies were performed in accordance with protocols approved by the College of William & Mary IACUC animal committee. Anesthesia of animals was performed using sodium pentobarbital (50-90 mg kg^{-1} body mass) injected into the *peritoneal cavity.* Spontaneous and transgenic tumor palpability in mature mice was evaluated bi-weekly. Following anesthesia an animal selected for imaging was subcutaneously injected in the femoral bicep with 0.52 MBq (14 μCi) $Na^{125}I$ (PerkinElmer, Waltham, MA) in 0.10 ml 0.9% saline as described in (Bradley et al., 2006). The animal was oriented supine on the detector during the imaging period and monitored throughout for rhythmic breathing.

In Vivo Gamma Imaging and Data Acquisition

The compact second generation gamma camera developed for "mouse-sized" biological planar imaging by (Bradley et al., 2006) was used for this study (Fig. 2.1). The compact detector incorporating a pair of 2-in square Hamamatsu H8500 positron sensitive photomultiplier tubes (PSPMTs) was installed on a gantry. The PSPMTs were optically coupled to a pixellated NaI(Tl) crystal array, each element measuring 1 x 1 x 5 mm^3 separated by 0.2 mm reflective walls. A 5 mm thick CuBe collimator designed for imaging 30 keV photons emitted from ^{125}I was employed with 0.55-mm square openings separated by 0.11 septa. This collimation provides a spatial resolution (FWHM) of 2.5 mm on contact with the collimator with an effective area of about 46 x 96 mm^2. The detector and related data acquisition instruments were interfaced to a computer. Each photon detected by the gamma camera was referred to as an "event". A program

developed with data acquisition software Kmax (Sparrow Inc., Sierra Vista, Arizona) recorded the time, energy and computationally determined coordinates of every event sorted into event files.

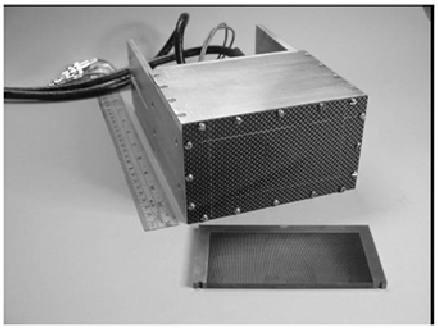

Figure 2.1. The second generation compact gamma camera developed for biomedical imaging applications.

Image Analysis

An analysis program developed with data processing and visualization language IDL (Research Systems Inc, Boulder, Colorado) was used to group event files into five-minute intervals recorded as two-dimensional matrices (referred to as "timecuts"). Each imaging session produced timecuts representing twelve five-minute digitized gamma images. The digital coordinates of each pixel (1.2 x 1.2 mm^2) correspond with the planar position where the counts of isotope decay in the mouse as visualized by the detector. The total counts that were recorded at each pixel represent the radioactivity detected at that location over the five-minute interval.

The IDL program was further used to visualize the total events in a designated region of interest (ROI). In order to compare the radioactivity contained in the tissues of interest, we normalized the values by expressing the ROI data as a percentage of the total injected dose (%ID) as defined by an ROI with 2880 pixels covering the entire body of the mouse. Tumors and glands of interest were analyzed with rectangular or square ROIs

of variable pixel dimension to contain the entire area of interest, while excluding nearby organs such as the heart, thyroid, or salivary glands. In addition, baseline radioactivity was subtracted within the ROI to derive the actual size and morphology of the tissues of interest. The baseline radioactivity was defined as the mean value of radioactivity in a four-pixel ROI that was placed over an area either in the abdomen or thorax that had a constant level of radioactivity throughout the imaging period. Tumor size was calibrated for each of the five minute timecuts as the total number of non-zero pixels in the tumor region after baseline radioactivity was subtracted (negative pixels were set to zero). The final tumor size (in pixels) was established during the 50-55 minute timecut, but the time to reach maximum size could occur at early or later times. This time frame was selected because some tumors continued to accumulate isotope throughout the imaging period. The total counts within the baseline radioactivity corrected ROIs were regarded as the net uptake of isotope, and were visualized as 13-level contour maps corresponding to the actual radioactive count matrices.

Difference Plots

Contour plots of the difference between raw tumor ROIs without threshold deduction were used to measure the changes in radioactivity that occurred within a tumor over time. Differences were analyzed with raw tumor ROIs between three different time intervals: 0-5 min vs. 5-10 min, 25-30 min vs. 30-35 min, and 50-55 min vs. 55-60 min. The difference between each set of tumor ROIs was calculated by subtracting the earlier raw tumor ROI from the later. The total difference values were then compared. The absolute positive and negative values for these “difference ROIs” were also visualized as

both a positive plot (counts increase over time) and a negative plot (counts decrease over time). A radioactive region in a positive difference plot represents radioiodine accumulation while the negative plot represents loss of radioactivity for the location within that time period.

Specimen Fixation and Whole Mount Immunofluorescence

Following the imaging process, selected mice were euthanized with an overdose of sodium pentobarbital. In order to preserve specimen orientation, silk surgical string was threaded through tumor tissues to identify medial, lateral, anterior, and posterior regions. Tissues were excised and fixed in 4% paraformaldehyde between 2 -12 hours at 4^{o}C. After fixation, tissues were rinsed in phosphate buffered saline (PBS) and stored at 4^{o}C. The whole-mount immunofluorescence technique used in this study was slightly modified from (Johnstone et al., 2000; Sillitoe and Hawkes, 2002). All incubations were performed with gentle agitation and wash periods were refreshed every hour unless specified below. Tissues were permeabilized with Triton-X-100 in PBS and non-specific binding was blocked with 2% serum in PBS for 6-8 hours. Tissues were incubated with 0.5 to 3 μg/mL polyclonal IgG rabbit anti-rat NIS (Alpha Diagnostic Int, San Antonio, Texas) primary antibody for 60 hours at 4^{o}C, and then rinsed with blocking solution for 4 hours. Control tissues were incubated in blocking solution. All tissues, including controls, were incubated with 0.5 to 2 μg/mL fluorescent goat anti-rabbit Alexa 488 secondary antibody (Invitrogen, Eugene, Oregon) overnight at 4^{o}C followed by rinsing in blocking solution for 4 hours. Bright field and fluorescein filtered photos were captured

with an Olympus MagnaFire DP71 digital camera and overlay images were created using Adobe Photoshop CS3 extended.

Immunohistochemistry

Cryosectioned specimens were placed in a humidified chamber to prevent drying and incubated for one hour with 2% Bovine Serum Albumin (BSA) + PBT to block non-specific immunoglobulin binding. Once the blocking procedure was completed the specimens were incubated with a specific primary antibody including: polyclonal IgG rabbit anti-rat NIS (Alpha Diagnostic, Inc., San Antonio, TX), polyclonal IgG rabbit anti-mouse Amphiregulin (Santa Cruz Biotechnology, Inc., Santa Cruz, CA), or polyclonal IgG rabbit anti-mouse HIF-1α (R&D Systems, Inc., Minneapolis, MN). Antibody concentrations ranged from 2 to 5 µg/mL. Tissues were incubated in the primary antibody at room temperature for two hours. Control specimens were incubated in blocking solution. Following the primary incubation the diluted antibody solution was stored at 4^{o}C for subsequent usage not exceeding four incubations. The specimens were rinsed in a series of five two-minute washes in blocking solution.

Sectioned tissues were incubated in an Alexa fluorescent-labeled secondary antibody, goat anti-rabbit Alexa 488 or goat anti-rabbit Alexa 555 (Invitrogen, Eugene, OR), diluted in blocking solution at room temperature for one hour in a dark humidified container. Secondary antibody concentrations ranged from 1 – 5 µg/ml. Specimens were rinsed in a series of five two-minute washes in PBT.

Excess PBT was tapped off and slides were mounted with nuclear stain Vectorshield with DAPI (Vector Laboratories, Burlingame, CA) and dried at 4^{o}C for two

hours or until photographed. Immunofluorescent tissue sections were photographed with an Olympus IX50 inverted fluorescent microscope equipped with an Evolution MP digital camera using fluorescein (488 nm) or rhodamine (555 nm) depending on the secondary antibody. UV filtered light was used also for DAPI visualization. Composite figures of fluorescent and DAPI images were created using Adobe Photoshop CS3 Extended Version 10.

Apoptosis and Necrosis Staining

Cryosectioned mammary tumors were stained for apoptosis and necrosis using a kit (Biotium Inc, Hayward, CA) and performed per manufacturer's instructions. Briefly, tissues were rinsed two times for 10 minutes in 1x Annexin V binding buffer provided in the kit. Following the wash, tissues were stained with a combination staining solution provided in the kit targeting Annexin V (apoptosis) and dye Ethidium Homodimer III (stains DNA). Tissues were incubated with the staining solution for 10 minutes and subsequently rinsed with 1x binding buffer. Tissue Slides were coverslipped and imaged with Olympus MagnaFire DP71 digital camera and overlay images were created using Adobe Photoshop CS3 extended.

Statistics

Images of PyVT tumors from immunohistochemistry and tumor contour plots were converted to 32-bit grayscale and pixel luminescence was calibrated using ImageJ 1.40g. The PyVT immunohistochemical images were resized to the scale of the contour plot image for analysis. Statistical analysis consisted of Student's t-test and Principle

Component Analysis (PCA) which were performed using Statistical Package for the Social Sciences (SPSS) software. Factor variables that were considered for the PCA test were as following: the age of the animal (in years) at the time of imaging; the body weight of the animal (in grams) prior to imaging; the number of identified tumors in each animal; the size of the tumor (as determined at 55 min into the imaging session); the percent of injected dose of radioiodine the tumors accumulated (overall tumor accumulation at 55 min into the imaging session); the uptake pattern of the tumor (center to edge = 1, multi-spot = 2, and ring =3); the location of the primary tumor (cervical =1, upper thoracic =2, lower thoracic =3, inguinal =4, and abdominal =5); and the pregnancy status of the animal (pregnant =1 and never pregnant =0). All PCA variables were scale values except for pregnancy, tumor pattern, and tumor location which were nominal values. Linear regression analysis was used to evaluate possible correlations between selected data sets. Data was considered statistically significant at the 95% ($p<0.05$) confidence level.

CHAPTER 3

RESULTS

MMTV Tumor Distribution

For the current study 58 MMTV mice with a total of 88 tumors were imaged and analyzed. Within this population the majority of mice presented one (n=36, 62%) or two tumors (n=18, 31%) at the time of imaging, and in very few cases (n=4, 7%) more than two tumors were imaged (Fig. 3.1a). Tumor formation on the left side (n=47, 53%) of the body was slightly more than on the right side (n=41, 47%) with the majority of tumors manifesting in the thoracic mammary glands (n=56, 64%) compared to other gland locations (Fig. 3.1b).

MMTV mice bearing multiple tumors (n=22, 38%) represent over half of the tumors (n=50, 57%) analyzed in this study. In cases where multiple tumors are present there is a bias toward tumor development in the left thoracic (n=16, 73%), right thoracic (n=13, 59%), and right inguinal (n=12, 55%) mammary glands compared to the left inguinal (n=6, 27%) location. Also, mice bearing multiple tumors have a slight bias for the largest tumor presented at the time of imaging to be located the right thoracic (n=8, 36%), left thoracic (n=6, 27%), and right inguinal (n=5, 23%) glands compared to the left inguinal (n=3, 14%) mammary gland location.

Imaging Radioiodine Uptake *In Vivo* Correlates with NIS Protein Expression in Normal Mammary Glands and Mammary Tumors of the MMTV and PyVT Models

In order to validate the efficacy of the gamma camera to detect functional NIS activity *in vivo*, NIS protein expression was analyzed by immunohistochemistry (IHC) in normal mammary and mammary tumor tissues. The initial step was to validate whether the gamma camera could detect functional NIS and radioiodine uptake in mammary glands under non-tumor conditions. Studies have shown that NIS is expressed and will transport radioiodine during lactation (Cho et al., 2000; Tazebay et al., 2000). Therefore, mice (n=6) from a low mammary tumor incidence strain, C57BL/J6 (Freund et al., 1992), were imaged at three different stages of normal mammary development, which included the nulliparous (virgin) mouse (n=2), the lactating mouse (n=2), and the multiparous (previously lactating) mouse (n=2) mammary stages (Fig. 3.2). Following the imaging process the nulliparous (n=5), lactating (n=4) and multiparous (n=5) mammary glands were analyzed for NIS expression. The gamma camera detected significant ($p<0.01$) radioiodine accumulation only during the lactating stage of mammary development (Fig. 3.2d) which was verified with IHC localization of NIS (Fig. 3.2b). Also, there was no radioiodine accumulation visualized in the mammary glands of nulliparous or multiparous mice which was further supported by negative IHC findings (Fig. 3.2a and c).

MMTV tumors also accumulate radioiodine throughout the imaging period which implicates functional NIS activity. NIS protein expression was analyzed via IHC in MMTV tumors (n=18) and detectable levels of NIS protein were demonstrated. These NIS locations were coincident with the locations of radioiodine uptake in the gamma

images of tumors (example in Fig. 3.3a). Unexpectedly, during the imaging session of a nulliparous MMTV tumor bearing mouse the gamma camera detected elevated radioiodine accumulation in a seemingly normal mammary gland (Fig. 3.3b). At necropsy, a small (3 mm) non-palpable tumor was located at the end of the mammary gland (Fig. 3.3b1). IHC localized NIS protein in the tumor which was coincident with the radioiodine accumulation pattern detected by the gamma camera.

In order to reaffirm that radioiodine accumulation was a function of NIS expression in the PyVT model, the protein was localized in tumor tissue using an anti-NIS antibody via indirect immunohistochemistry (Fig. 3.4). The left inguinal tumor was excised and assessed for NIS whole mount expression (Fig. 3.4b-d). Both the gamma image and NIS protein were highly associated (Fig. 3.4e).

Three dimensional gray scale luminescence models were made for both the contour plot, made from a region of interest (ROI) around the tumor in the gamma image, and the fluorescent NIS optical image (Fig. 3.5). The contour plot (Fig. 3.5a) provided topographical data of the ROI gamma counts from radioiodine within the tumor at the 50-55 minute time cut which was our best estimate of overall tumor size. The three dimensional images of both the contour plot and optical fluorescent image (Fig. 3.5b) were also highly similar. However, the optical protein localization intensity suggested that there was more NIS protein in the lower part of the tumor compared to the intensity of the amount of radioiodine that accumulated in the same area.

In early PyVT tumorigenesis (Fig. 3.6) gamma imaging detected localized areas with increased radioiodine accumulation in the inguinal mammary glands. However, upon whole mount localization for NIS protein (Fig. 3.6b-d), there appeared to be

discrete expression patterns for NIS during early tumorigenesis that the gamma camera can detect, but with less resolution. The high power (7x) localization suggests that NIS is expressed in isolated groups of cell clusters (Fig. 3.6f). The apparent amalgamation of the radioiodine uptake within these cluster groups appeared on the gamma camera as a compact area of uptake. This further supports the applicability of the gamma camera to detect early tumorigenesis in the PyVT model with radioiodine targeting of NIS function.

In Vivo Screening for PyVT Mice and Mammary Tumors Using Gamma Imaging

At parturition approximately 25% of female progeny carry the PyVT transgene based on Mendelian genetics (Guy et al., 1992). In order to non-invasively identify which individuals were transgenic, pups were screened using the gamma camera. By five weeks pups were selected at random (n=6) from candidate litters and injected with 0.52 MBq (14 μCi) $Na^{125}I$. Fifty minutes after $Na^{125}I$ administration, pups were imaged supine for 10 minutes. By screening individual animals, wild type mice (Fig. 3.7a) and PyVT candidates (Fig. 3.7b) were identified based on radioiodine accumulation in nulliparous mammary glands. To ensure that the radioiodine uptake was not solely in response to mammary maturation due to endocrine stimuli, PyVT candidates were re-imaged a week later and continued to incorporate radioiodine in the mammary glands (Fig. 3.7c). In all cases mice identified as PyVT candidates from *in vivo* screening developed palpable tumors in all mammary glands which were detected with radioiodine gamma imaging (Fig. 3.7d).

A measure of the percent injected dose of radioiodine was assessed between all wild type and PyVT screened mammary glands. PyVT individuals exhibited greater

radioiodine accumulation in a minimum of three mammary gland locations compared to wild type siblings (Fig. 3.8a, PyVT marked with *). Further analysis indicated that the overall mammary gland radioiodine accumulation in PyVT animals was significantly greater ($p<0.01$) than the mammary glands of wild type siblings (Fig. 3.8b).

The Unique Biodistribution of Radioiodine in MMTV Tumors

Region of interest analysis of MMTV tumors revealed that the biodistribution of radioiodine could be classified into three discrete patterns of uptake. The first uptake pattern in which MMTV tumors (n=28) would accumulate radioiodine was a "center to edge pattern". This pattern was characterized as a central active core which becomes less intense toward the edge of the tumor (Fig. 3.9a). The second pattern classification was the "multi-spot pattern" which was most prevalent (n=63) in MMTV tumors. The multi-spot pattern was characterized as having multiple centers within the tumor that were active (Fig. 3.9b). The final classification type was a special multi-spot pattern called the "ring". This pattern was rarely observed in MMTV tumors (n=5) and was characterized because the tumor center shows less activity than the surrounding edges (Fig. 3.9c).

Relationship Between Tumor Size, Uptake Patterns, and Radioiodine Accumulation in MMTV and PyVT Tumors

In order to assess a possible relationship between radioiodine uptake patterns and tumor size or the radioactive dose tumors would accumulate, tumors falling into a specific classification were compared. Using Student's t-test the uptake patterns were significantly ($p<0.01$) correlated with tumor size in all groups (Fig. 3.10a). When

compared with the percent injected dose, the uptake patterns significantly ($p<0.01$) correlated with center to edge and multi-spot groups, however the ring group was not a significant ($p>0.05$) distinguishable from the multi-spot group (Fig. 3.10b).

Once we established that the radioiodine uptake patterns correlated with tumor size and percent injected dose from box plot analyses, all three categories were plotted together and the data indicate that tumor size correlates with overall total radioiodine accumulation in a MMTV tumor (Fig. 3.11a). The data further suggested that the center to edge pattern was present in smaller (less than 75 pixels), with less total radioactivity. By comparison, the multi-spot pattern exists throughout the entire tumor size range, but is predominant in larger (greater than 75 pixels) tumors. The ring pattern was predominantly associated with very large (>200 pixels) tumors. At the pixel level, which is as close to the cellular level as the gamma camera can resolve radioiodine, the center to edge and ring pattern tumors continued the same overall trend of more radioactivity associated with increased tumor size (Fig. 3.11b). However, the multi-spot tumor pattern showed no correlation between tumor size and per pixel radioactivity.

Based on the correlation data in figure 3.11, there appeared to be two trends of radioiodine uptake across various sized tumors. The first “High” trend can be represented tumors that accumulated high levels of radioiodine with increased tumor size. The second “Low” trend is characterized by tumors that only reached a low plateau of radioiodine with increased tumor size. These trends were most obvious at the pixel level (see Fig. 3.11b).

From the entire tumor data set, three groups (ten tumors in each group with similar size) were randomly selected from small, moderate, and large tumors (Fig.

3.12.1). Within each cohort group the first 30 minutes of the radioiodine uptake was averaged to get one “high” trend and one “low” trend and the rates of uptake were compared between each groups. The small tumor cohort (Fig. 3.12.2a) had a rate of radioiodine accumulation 1.5 times greater in the “high” trend group compared with the “low” trend. In the moderate and large tumor cohort (Fig. 3.12.2b and c), the rate of radioiodine accumulation was two times greater in the “high” trend groups compared with the “low” trends. These data suggest that tumors within the moderate to large size range that have similar uptake patterns could be grouped separately based on the rate of radioiodine accumulation.

A principal component analysis (PCA) was used as a guide to observe how coherently the variables collected at the time of imaging related to overall MMTV tumorigenesis. Eight variables were considered in the PCA test including: age, body weight of the mouse, tumor size, percent of radioiodine accumulated in the tumor, uptake pattern, pregnancy, tumor location on the body, and the number of tumors presented. Three principal components were extracted from the data variables which explained 64% of the total variance between the variables. The three components extracted were the percent injected dose component (PC 1), the pregnancy component (PC 2), and the gland location component (PC 3). These components were named based on the highest scoring component coefficient (TABLE 3.1), which represented the weights used to compute the factor scores to each variable. The extracted components also indicated which variables were correlated along with the principal components (Fig. 3.13).

The first component, the percent injected dose, was highly correlated with tumor size (Fig. 3.14a) which validated our previous findings (Fig. 3.11a). The second

component, pregnancy, was negatively correlated with animal age, which suggested that MMTV animals with tumors were more likely to be young and pregnant/previously pregnant or older virgin mice (Fig. 3.14 b). Pregnancy also correlated with the number of tumors an animal had at the time of imaging. These data suggested that in the MMTV model parity increased the likelihood of both tumor formation and the number of tumors that would manifest (Fig. 3.15a). The third component, mammary gland location, was correlated with the animal's body weight. In the MMTV model it appeared that larger tumors, which would also contribute to overall body weight, were located in the lower thoracic and inguinal/abdominal regions of the body (Fig. 3.15b).

Nine PyVT mice with twenty-six tumors in total were sorted into two groups based on the way they accumulated radioiodine over the hour imaging period. The first group was the center to edge pattern which is characterized by a central hot mass spreading out towards the edge of the tumor. The second group was the multi-spot pattern with multiple areas within the tumor that are active. A comparison between the two groups shows that there was a significant ($p<0.01$) difference both in terms of tumor size (pixels) (Fig. 3.16a) and the overall percent of the injected dose that these tumors accumulated (Fig. 3.16b). This suggests that the uptake patterns are uniquely different and can be used as predictors of tumor size and radioactivity.

Further analysis comparing tumor size (in pixels) at the 50-55 minute time cut, the percent injected dose, and tumor uptake patterns indicated that there was a positive correlation between the size of the whole PyVT tumors and the percent of the injected dose these tumors accumulated (Fig 3.17a). Also tumors falling into the center to edge ^{125}I uptake pattern were predominant in small tumors (<50 pixels). At the pixel level,

which is as close to the cell level as the gamma camera can detect there was no relationship between the size of the tumors and radioactive dose (Fig 3.17b). This suggests that in the PyVT model there is a uniform accumulation rate throughout the tumor at the pixel level.

Difference Plots

The difference plots revealed specific areas within each tumor that were actively incorporating (Fig. 3.18, color scale) or not incorporating (Fig. 3.18, grayscale) radioiodine at the beginning (Fig. 3.18a), mid-point (Fig. 3.18b) and end (Fig. 3.18c) of imaging sessions. There was profound heterogeneity in these accumulation patterns throughout the MMTV population, but these plots suggested that the greatest amount of activity change in tumors occurred during the first 10 minutes of the imaging session immediately following radioiodine administration (Fig. 3.18a). Areas that continue to accumulate radioiodine throughout the imaging session were generally next to or within the area that was originally very active. Negative difference plots indicated that radioisotope loss within the tumor occurred primarily in the last half of imaging (Fig. 3.18b and c). The data indicate that the majority of tumors (n=63 out of 88) lose radioisotope toward the end of the imaging session.

The yellow arrows in Fig. 3.18a, b, and c represent a presumed pathway of radioiodine transfer in a mammary tumor. The suspected pattern indicates that radioiodine transfer occurred from the outer edge of the tumor toward the central mass of the tumor. In some cases areas of active radioiodine uptake and loss correlate with the

expression patterns of NIS (Fig. 3.18d) suggesting that the difference plots may provide critical information about the sites within the tumor where functional NIS is expressed.

In Vivo Imaging of MMTV and PyVT Tumor Growth and Development

Repetitive *in vivo* gamma imaging can possibly be employed for targeting the molecular signatures of tumors for longitudinal studies lasting throughout tumor development. In order to determine whether tumor growth and development displayed unique signatures that could be assessed with the gamma camera, a subset of the MMTV population (n=7) were imaged two (n=5) or three (n=2) times. Between each imaging session the overall change in tumor size (in pixels) was calculated and divided by the time lag (in days) between imaging sessions to calculate tumor growth rates (TABLE 3.2). There were two cases (mice 4 and 6) of apparent tumor size reduction, but the growth rate for these two animals was not significant ($p>0.05$). The rest of the tumors analyzed (n=11) all increased in size. However, no correlation between tumor growth rates and the initial size, location and pattern of the tumor was detected. In two cases (mice 5 and 7) there was a change in radioiodine uptake in subsequent imaging sessions. In both circumstances a center to edge tumor pattern was identified as a multi-spot pattern accumulation pattern by the next imaging session. There were no cases of multi-spot pattern tumors changing their pattern of radioiodine uptake which further suggests that the center to edge pattern appears specific to smaller tumors.

Early screening for PyVT mice identified individuals in the population as candidates to track and monitor for early tumor progression. In figure 3.19a the right thoracic tumor was analyzed as early as five weeks of age, and there was a shift from a

center to edge pattern (figure 3.19a1) when the tumor was first detected to a multi-spot pattern on subsequent imaging sessions (Fig. 3.19a2 and Fig. 3.19a3). There was a positive correlation with the size of the tumor and the amount of the radioiodine dose the tumor accumulated as seen previously in (Fig. 3.17a), but at the pixel level monitoring tumor progression had a negative correlation (Fig. 3.19b) which implies that ^{125}I transport in groups of cells decreases with tumor progression. This was a point of difference compared to the finding in (Fig. 3.17b) that there was no relationship and uniform cellular ability to accumulate ^{125}I.

MMTV Tumorigenesis Influences ^{125}I Accumulation in the Mammary Glands

During the imaging process many apparently non-tumor mammary glands were observed to accumulate radioiodine when a primary MMTV tumor was present in the animal. Previous studies have reported that normal radioiodine accumulation occurs in mammary glands during lactation (Tazebay et al., 2000; Wapnir et al., 2003; Zuckier et al., 2001), which was further validated by this study using the gamma camera. In addition to this expected finding, the imaging data here suggest that the majority of MMTV mice also accumulate radioiodine in one (n=50, 87%) or two (n=43, 75%) mammary glands which were not originally detected as the site of the primary tumor.

NIS protein expression was analyzed for mammary glands (n=16) that accumulated radioiodine but were not specified as the site of the primary tumor based on gamma imaging. The majority of these glands (n=12, 75%) that were analyzed for NIS expression were positive by immunohistochemistry. In Fig. 3.20, the inguinal mammary gland was analyzed for NIS expression in a mouse with a mammary tumor (Fig. 3.20a)

and a different mouse happening to develop a non-mammary tumor (Fig. 3.20b). In both cases there were detectable levels of radioiodine accumulation identified by the gamma camera imaging which correlated with the localization of NIS protein in the mammary glands (Fig. 3.20a3 and b3). Moreover, these data suggest that the presence of a tumor (mammary based or not) influences the biology of non-involved mammary glands to become receptive to radioiodine accumulation.

Comparisons of the Radioiodine Accumulation in Spontaneous (MMTV) and Transgenic (PyVT) Tumor Models

Once it was confirmed that the gamma camera was also capable of imaging mammary tumors in the PyVT model, a comparison was made between the overall radioiodine uptake patterns in transgenic mice compared with those observed in spontaneous MMTV animals. Since PyVT mice (n=9) develop tumors in all mammary glands, these animals were compared with MMTV mice (n=11) also bearing more than one tumor to control for radioiodine signal dispersal in multiple mammary tumor sites. A fixed region of interest (ROI) (9 pixels) was placed over the hottest area of uptake in all mammary tumors and analyzed for the percent injected dose of radioiodine. Figure 3.21a shows that the size range of tumors was similarly distributed for both MMTV (n=24 tumors) and PyVT (n=26 tumors) mice. Student's t-test further supported that the average tumor size was not significantly (p=0.65) different between the two groups. Similar distributions control for tumor size in both groups that could bias radioiodine accumulation measurements since we have shown that tumor size and radioiodine accumulation are related (see Fig. 3.17a). The overall average percent injected dose of

radioiodine in the PyVT model was significantly ($p<0.01$) more than the spontaneous MMTV model bearing multiple tumors (Fig. 3.21b). Interestingly there is also a factor of two greater average rate of ^{125}I accumulation in the PyVT model compared to the average rate in the MMTV model.

a

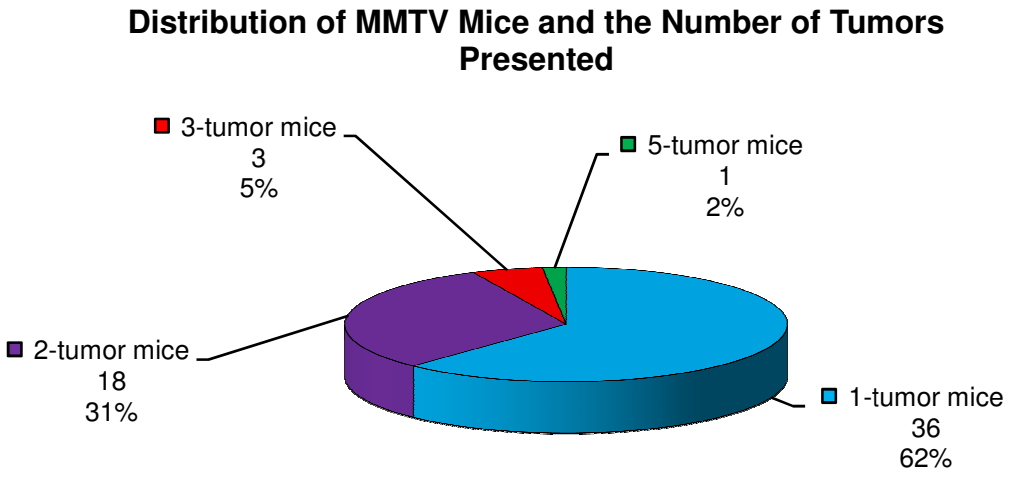

b

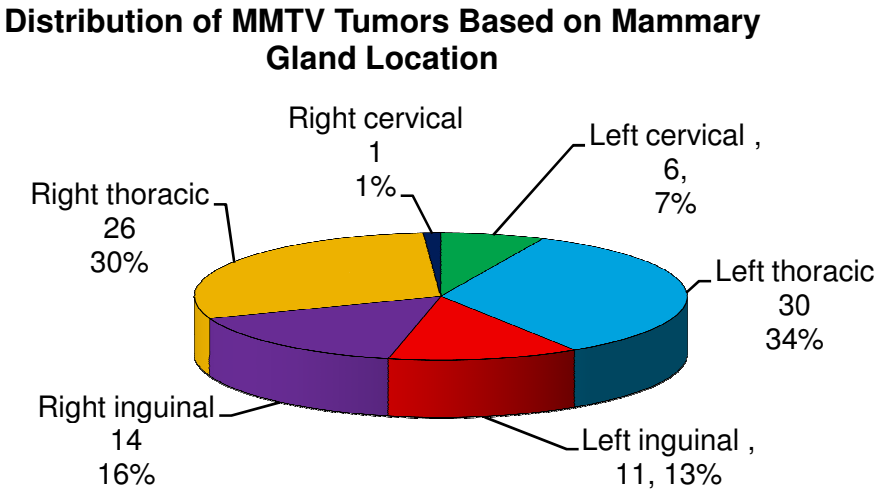

Figure 3.1. (a) The distribution of MMTV mice used for the *in vivo* gamma imaging project and the number of tumors presented at the time of imaging. (b) The distribution of MMTV tumors and the mammary gland site of tumorigenesis.

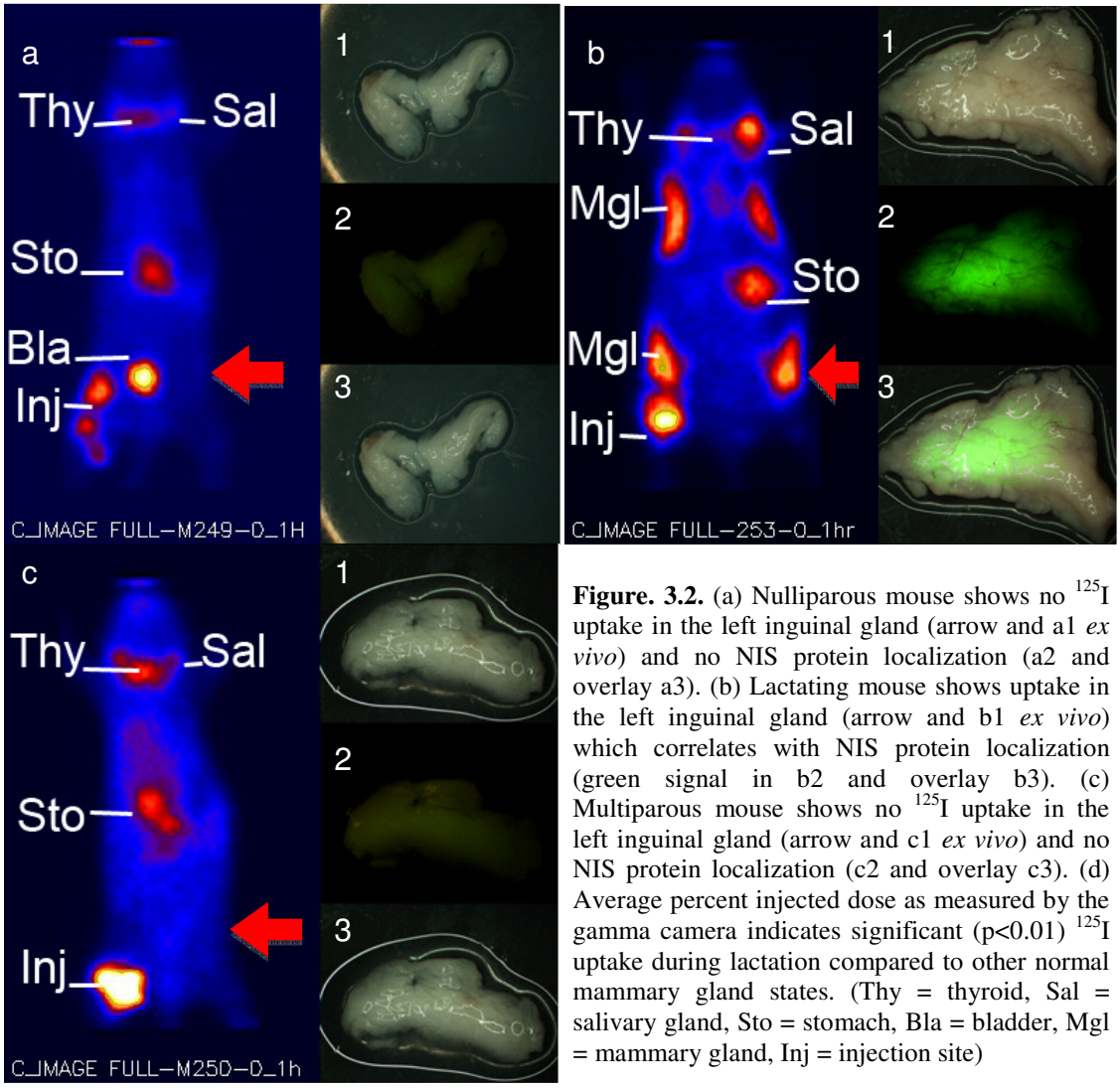

Figure. 3.2. (a) Nulliparous mouse shows no ^{125}I uptake in the left inguinal gland (arrow and a1 *ex vivo*) and no NIS protein localization (a2 and overlay a3). (b) Lactating mouse shows uptake in the left inguinal gland (arrow and b1 *ex vivo*) which correlates with NIS protein localization (green signal in b2 and overlay b3). (c) Multiparous mouse shows no ^{125}I uptake in the left inguinal gland (arrow and c1 *ex vivo*) and no NIS protein localization (c2 and overlay c3). (d) Average percent injected dose as measured by the gamma camera indicates significant ($p<0.01$) ^{125}I uptake during lactation compared to other normal mammary gland states. (Thy = thyroid, Sal = salivary gland, Sto = stomach, Bla = bladder, Mgl = mammary gland, Inj = injection site)

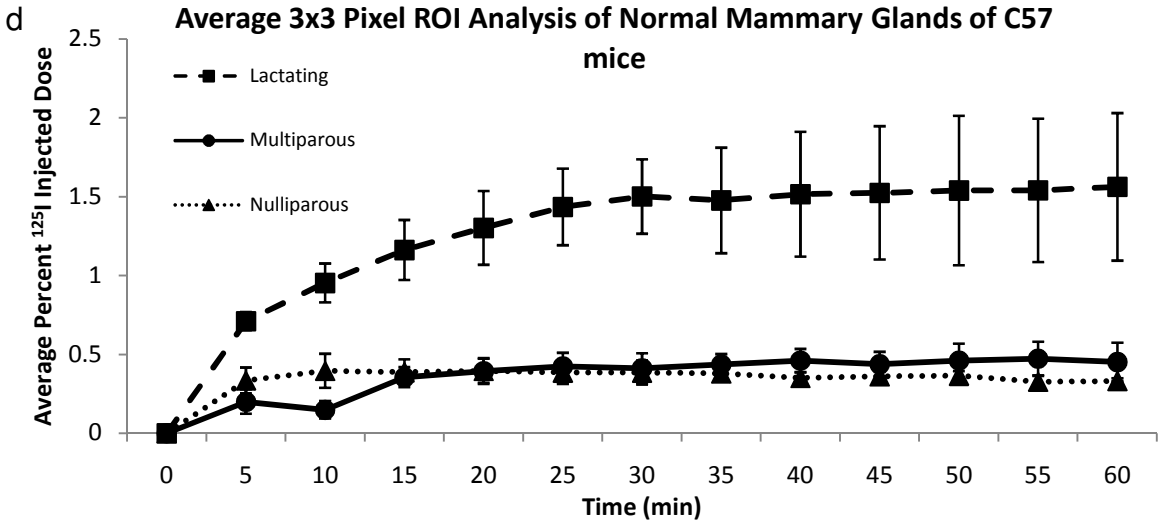

a

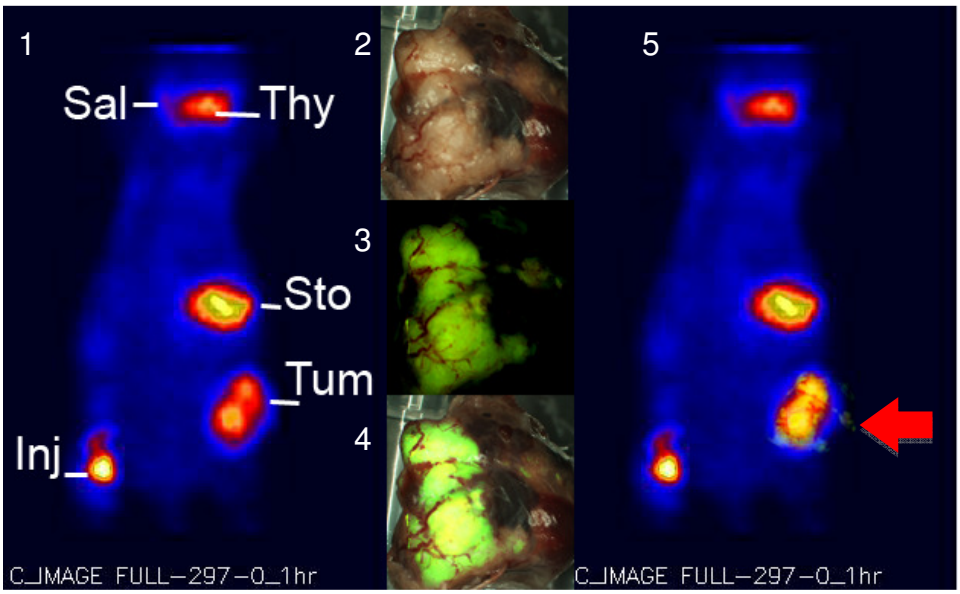

b

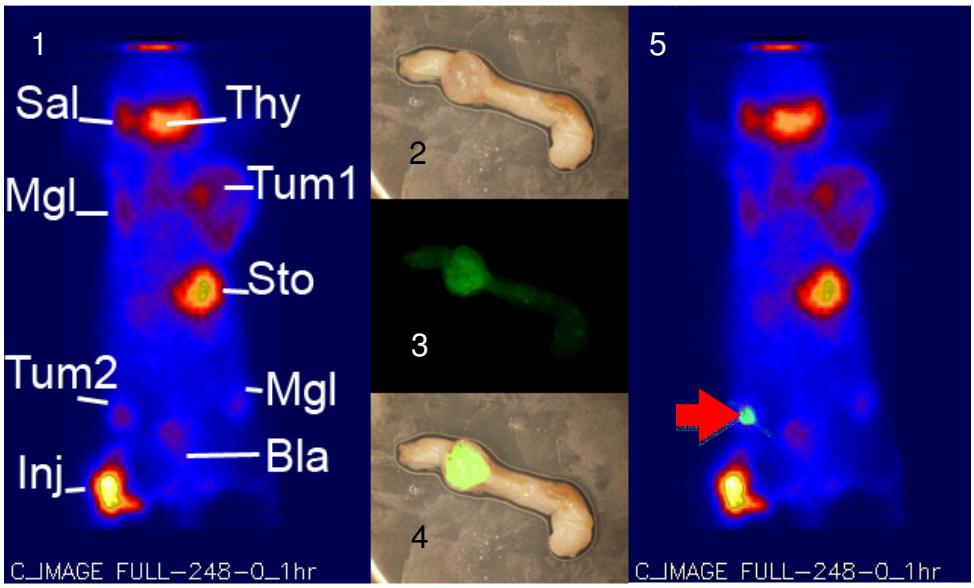

Figure 3.3. (a) Gamma camera detects ^{125}I uptake in a MMTV left inguinal primary tumor (a1). The primary tumor (a2 *ex vivo*) also localizes NIS protein in the non-necrotic portion of the tumor (green signal in a3 and a4 overlay). Both the ^{125}I accumulation and NIS protein localization are highly associated (a5 arrow). (b) The gamma camera can detect MMTV tumors at an early stage of tumorigenesis. The right inguinal tumor (b1, Tum2) was detected based on elevated ^{125}I accumulation. NIS protein was localized in the secondary tumor (b2 *ex vivo*) predominantly in the 3 mm tumor at the end of the mammary gland (green signal in b3 and b4 overlay). A composite of the gamma image and the NIS immunohistochemistry image of the small tumor are highly similar (b5 arrow). (Thy = thyroid, Sal = salivary glands, Sto = stomach, Bla = bladder, Inj = injection site, Mgl = mammary gland, Tum = tumor)

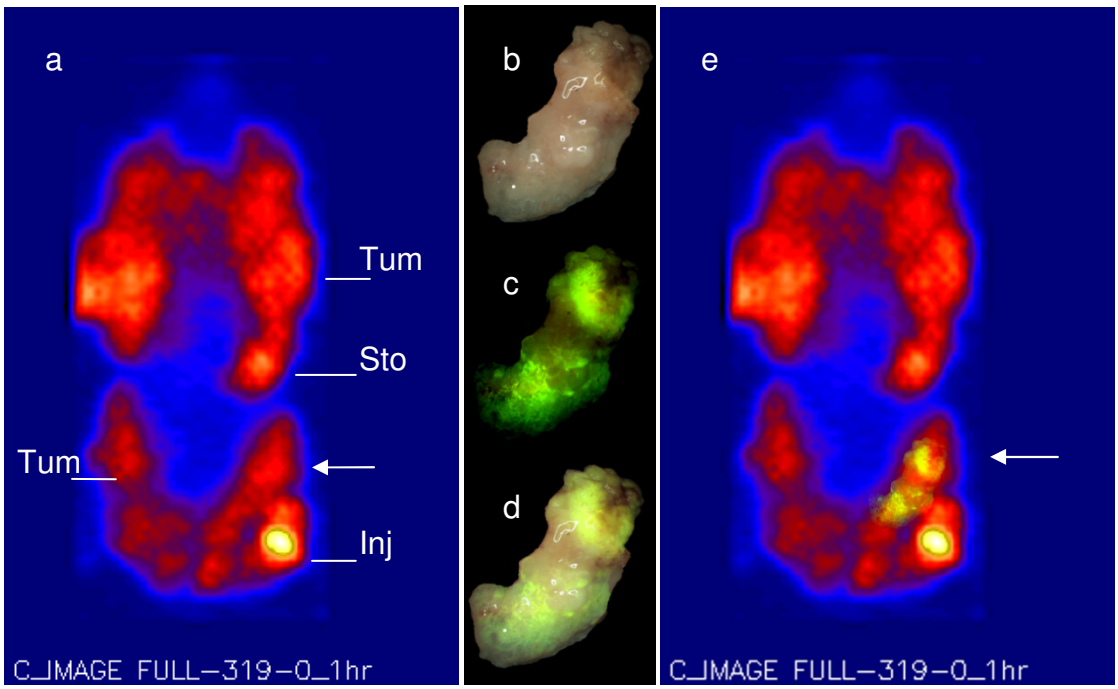

Figure 3.4. (a) PyVT gamma image from a sixty minute imaging session. (b) Brightfield image of the left inguinal tumor (arrow a). (c) Indirect whole mount NIS localization in the left inguinal tumor (green signal) using an anti-NIS primary antibody. (d) Overlay image of the bright (b) and fluorescent (c) images identifying the areas in the tumor where NIS is expressed. (e) An overlay of the PyVT gamma image (a) with NIS localization (c). The NIS image was scaled down and mimics the radioiodine trend seen in the gamma image (arrow, yellow signal). (Tum = tumor; Inj = injection site; Sto = stomach)

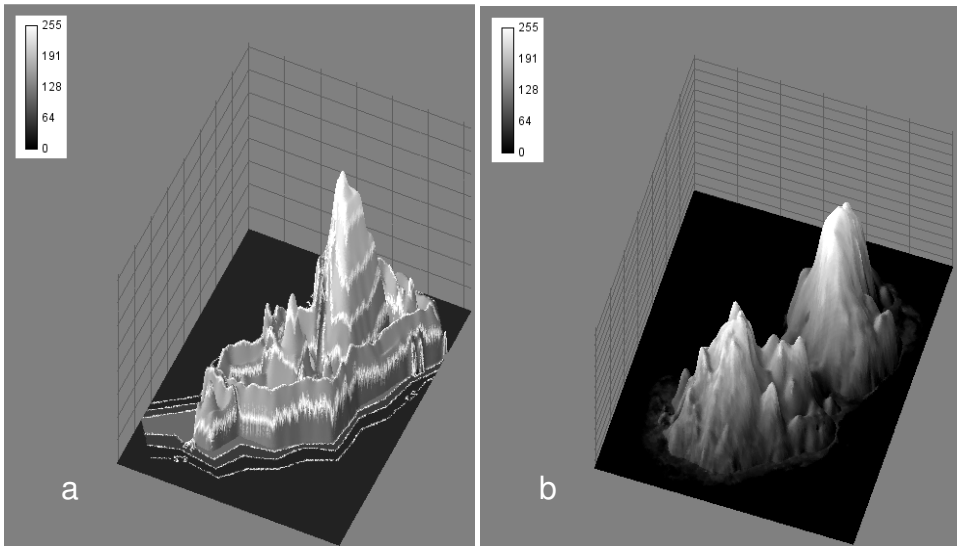

Figure 3.5. (a) Gray scale three dimensional pixel luminescence profile of the 50-55 minutes time cut contour plot of the gamma image for the left inguinal tumor. (b) Gray scale three dimensional pixel luminescence profile of fluorescent NIS localization in the left inguinal tumor. (inset luminescence scale)

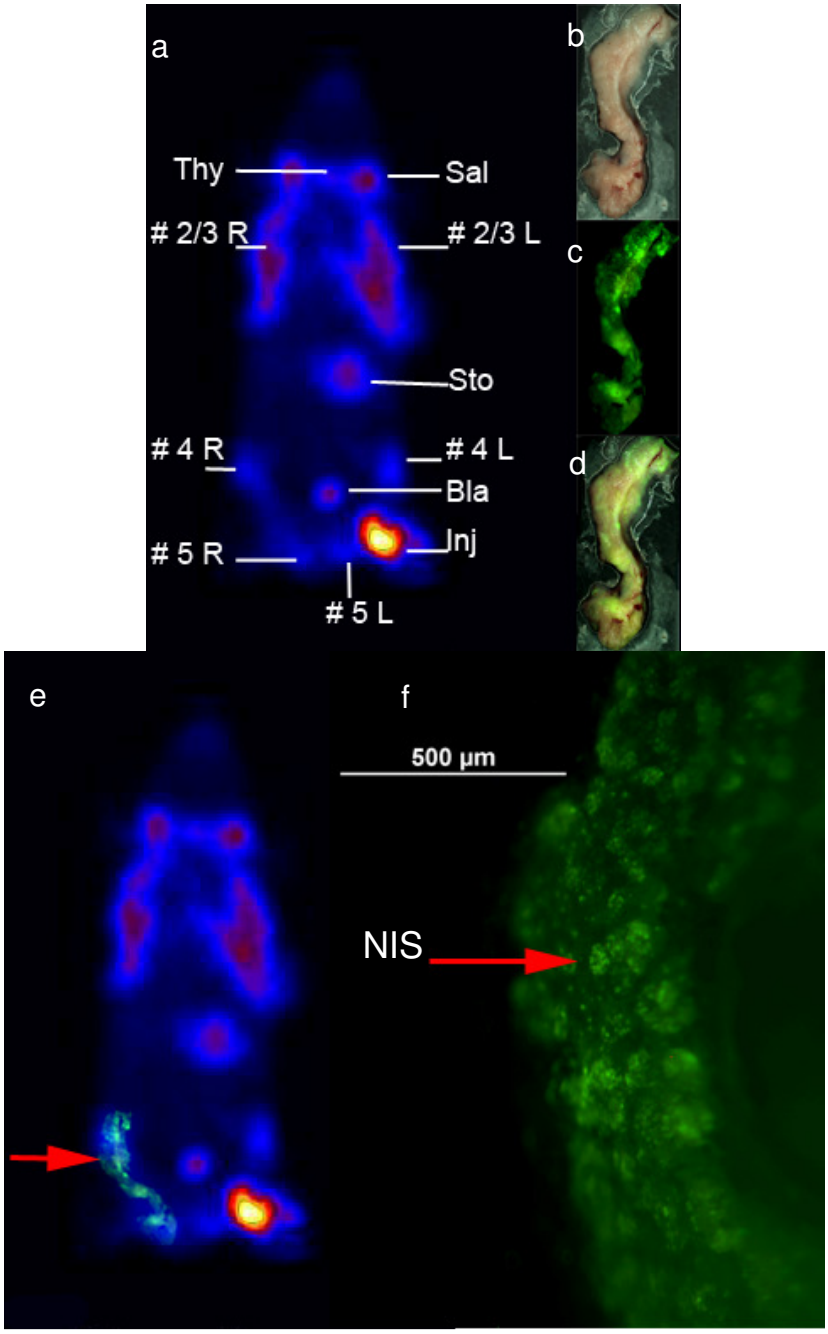

Figure 3.6. NIS expression patterns in an early PyVT tumor. (a) The gamma image of early tumorigenesis in a PyVT mouse with ^{125}I accumulation in all mammary gland sites. (b) *Ex vivo* bright field image of the right inguinal gland (#4 R upper, with early lesions) connected to the right abdominal tumor (# 5 R, lower). (c) NIS localization indicates discrete expression patterns in the inguinal gland, and more significant staining in the abdominal tumor area. (d) Overlay image of (b) and (c). (e) Overlay of NIS localization (c) and the gamma image (a) suggests that the discrete pattern of NIS expression was detectable in the gamma image as a localized area of activity. (f) A 7x view of the acini expression patterns of NIS in the right inguinal mammary tumor (#4 R). (Thy = thyroid, Sal = salivary glands, Sto = stomach, Bla = bladder, Inj = injection site, # 2/3 = thoracic tumors, # 4 = inguinal tumors, # 5 = abdominal tumors)

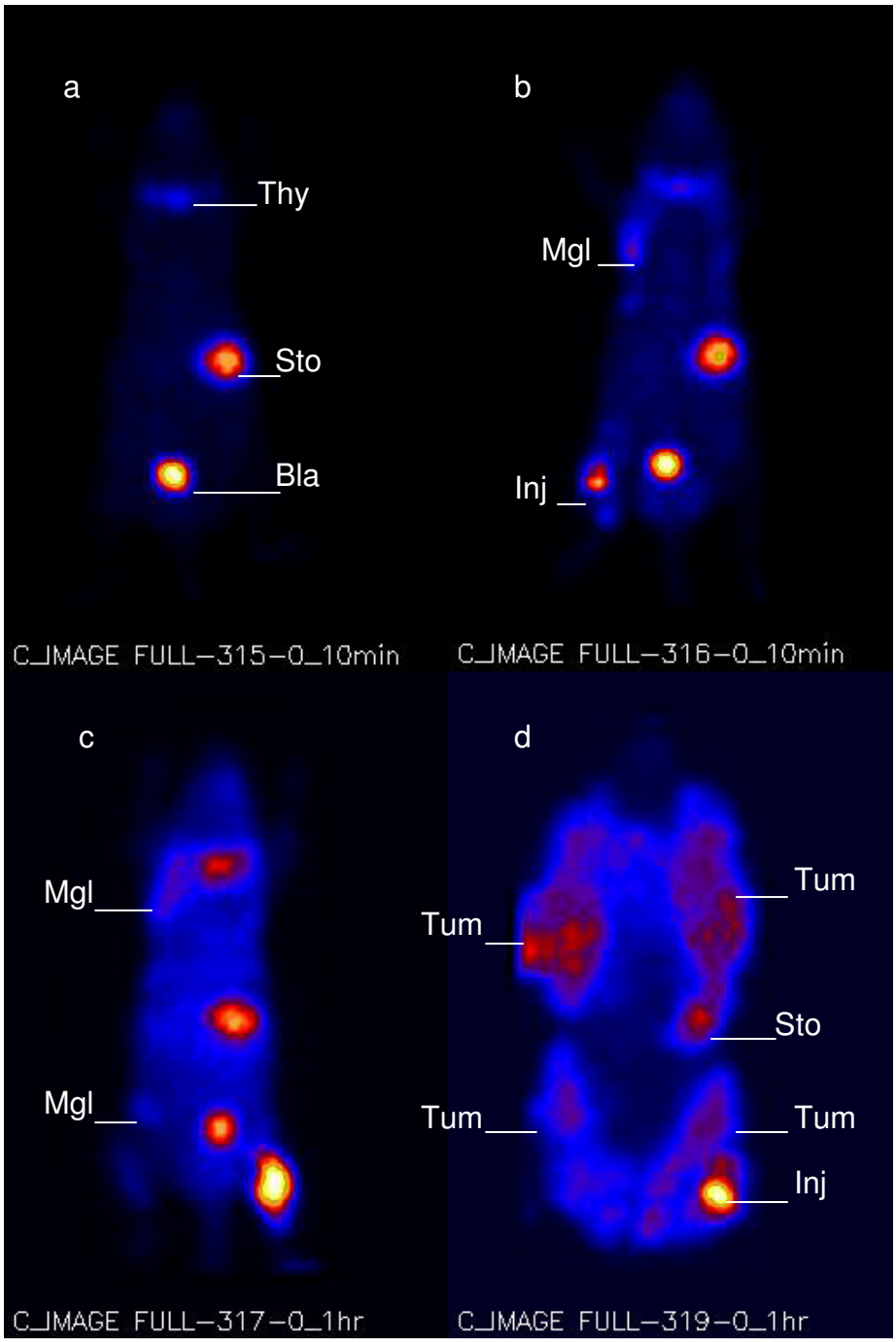

Figure 3.7. Example of gamma camera screening of the PyVT model with ^{125}I. (a) A 10 min. screen identifying a wild type FVB/N littermate showing no mammary accumulation at 5 weeks. (b) A 10 min. screen at 5 weeks identifying a PyVT mouse showing ^{125}I accumulation in the right thoracic mammary gland. (c) One hour imaging of PyVT mouse (b) at 6 weeks with accumulation in putative tumor mammary, but uptake was evident in other glands as well. (d) One hour imaging of PyVT mouse (b and c) at 16 weeks with mammary tumors in all glands. (Thy = thyroid, Sto = stomach, Mgl = mammary gland, Tum = tumor, Inj = injection site, Bla = bladder)

a

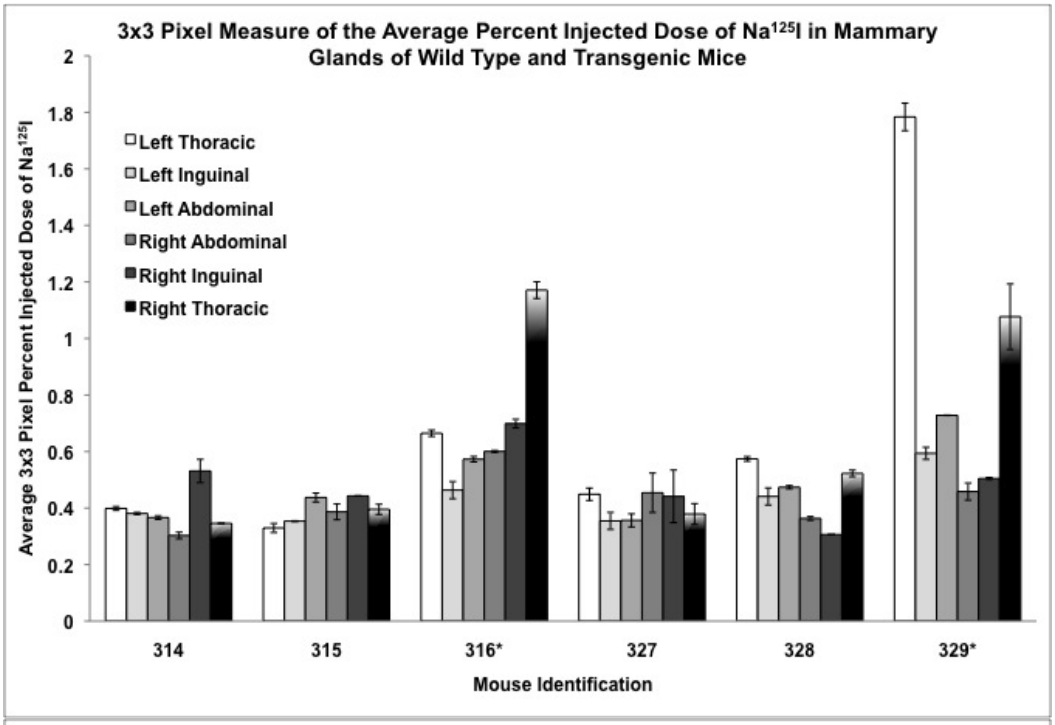

b

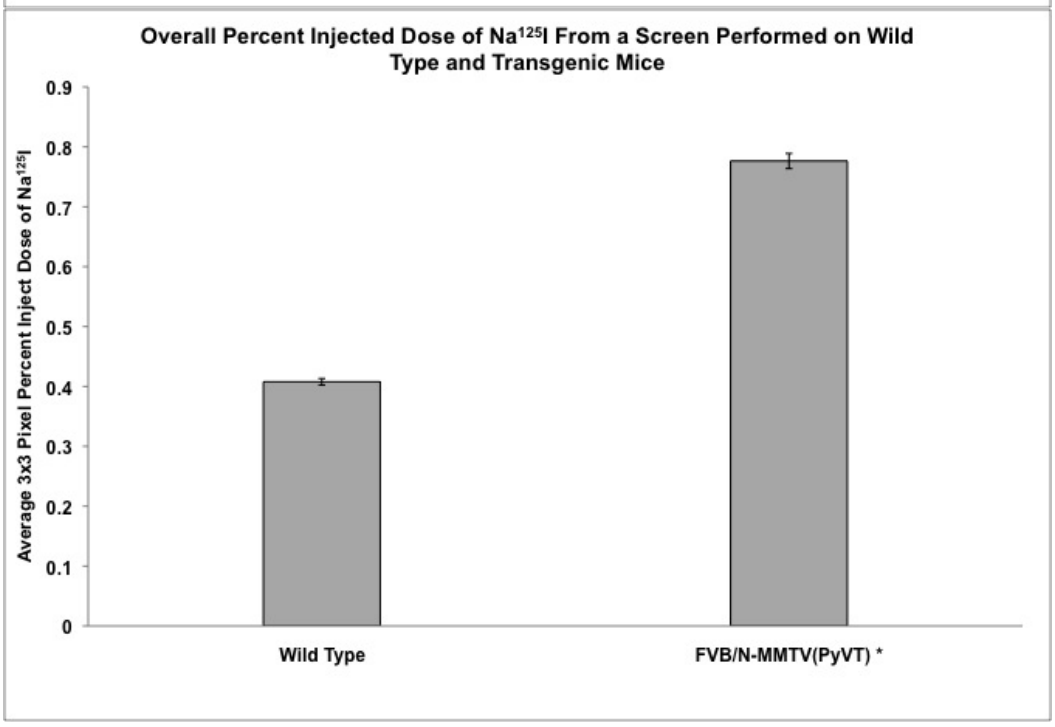

Figure 3.8. PyVT mammary gland ^{125}I uptake from screening studies. (a) Radioiodine accumulation in all mammary glands of mice screened for PyVT transgene expression (Mice 314-316 screened at 5 weeks and Mice 327-329 screened at 7weeks). (b) Overall radioiodine uptake was significantly different ($p<0.01$) in PyVT mice compared to wild type siblings.

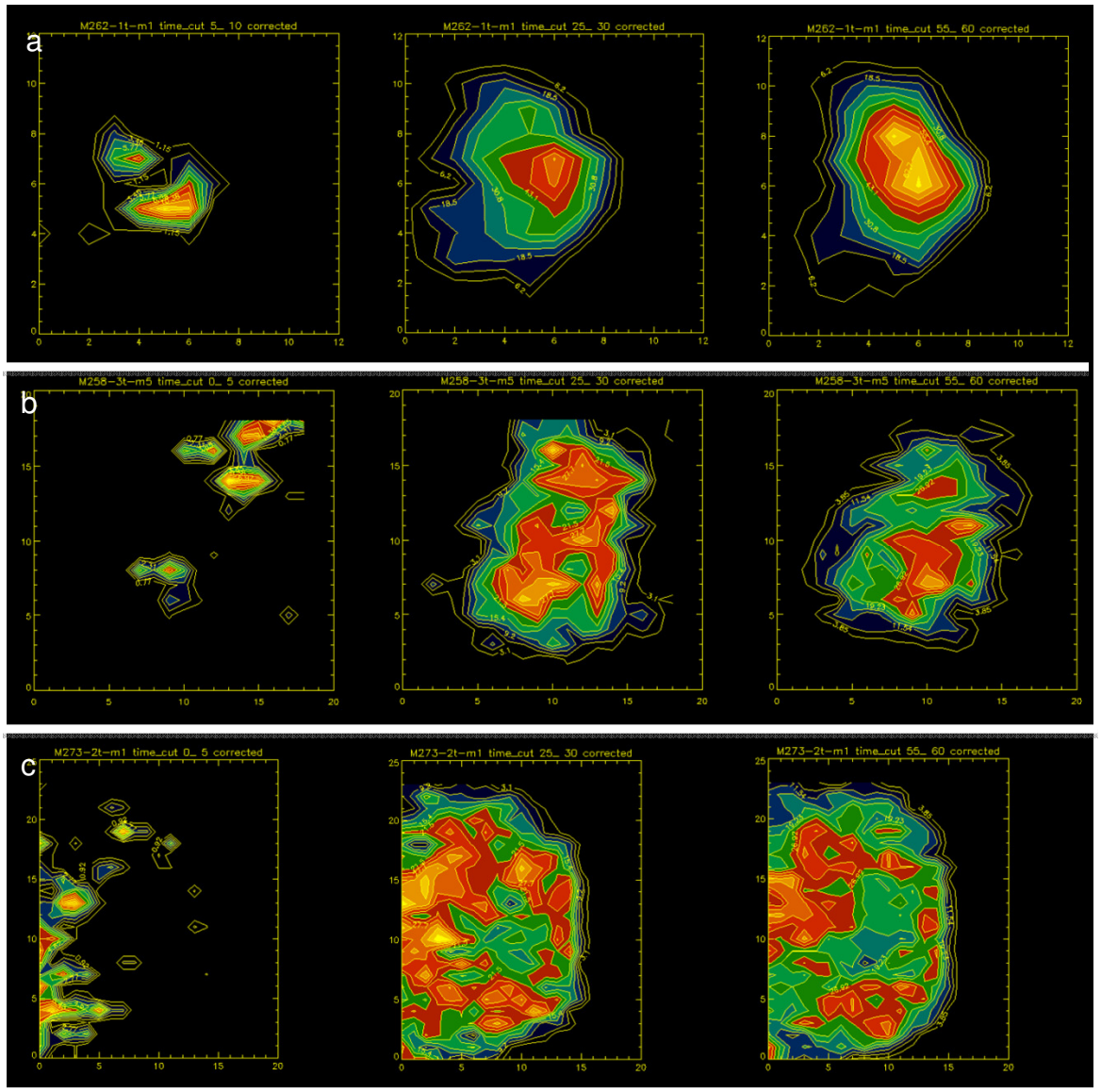

Figure 3.9. Contour plots of the three types of ^{125}I distribution observed in MMTV tumors at three different times during the imaging period (the left panel measures at 0-5 min, the center panel measures at 25-30 min, and the right panel measures at 55-60 min). (a) A center to edge accumulation pattern characterized by a central active core which spreads to the tumor edges. (b) A multi-spot pattern characterized by many active areas within the tumor. (c) The ring pattern is characterized as a special case of multi-spot in which the core of the tumor is less active than the surrounding edges of the tumor.

a

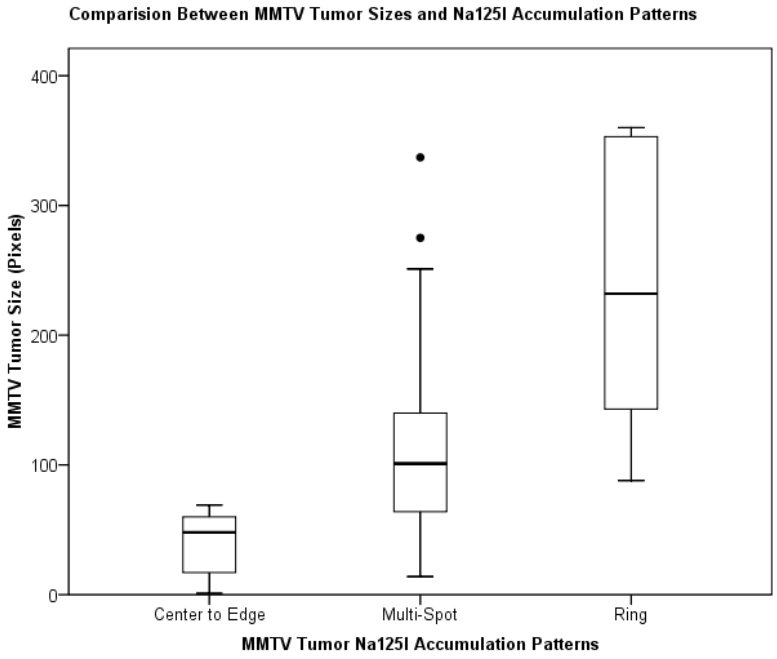

b

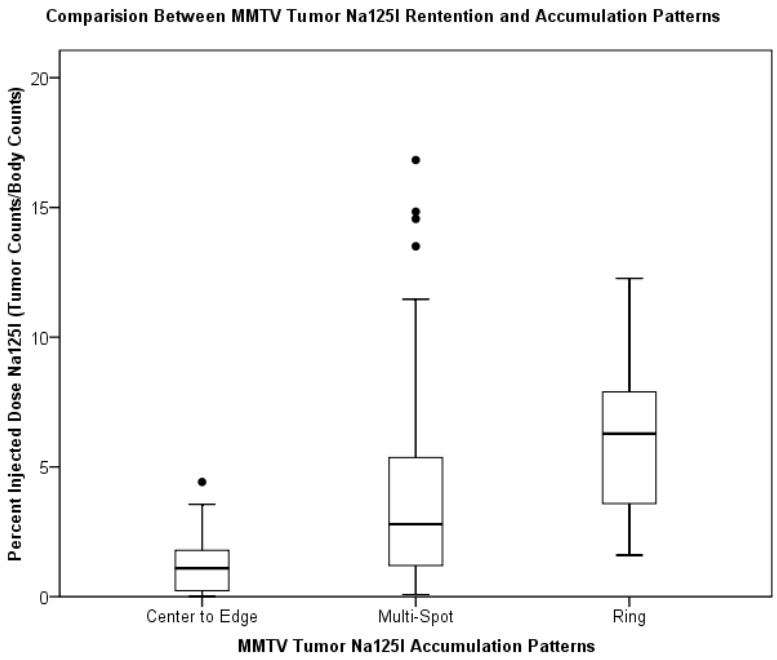

Figure 3.10. (a) Box plot analysis, comparing MMTV tumor size with the three radioiodine accumulation patterns, indicates that each uptake pattern is a significant ($p<0.01$) to specific tumor size ranges. (b) Box plot comparison between the three radioiodine accumulation patterns and the percent of injected dose for MMTV tumors suggests that the center to edge and multi-spot uptake patterns significantly ($p<0.01$) predict radioactivity in tumors. The percent injected dose between the multi-spot and ring pattern was not significant ($p>0.05$). (The dots represent outliers.)

a

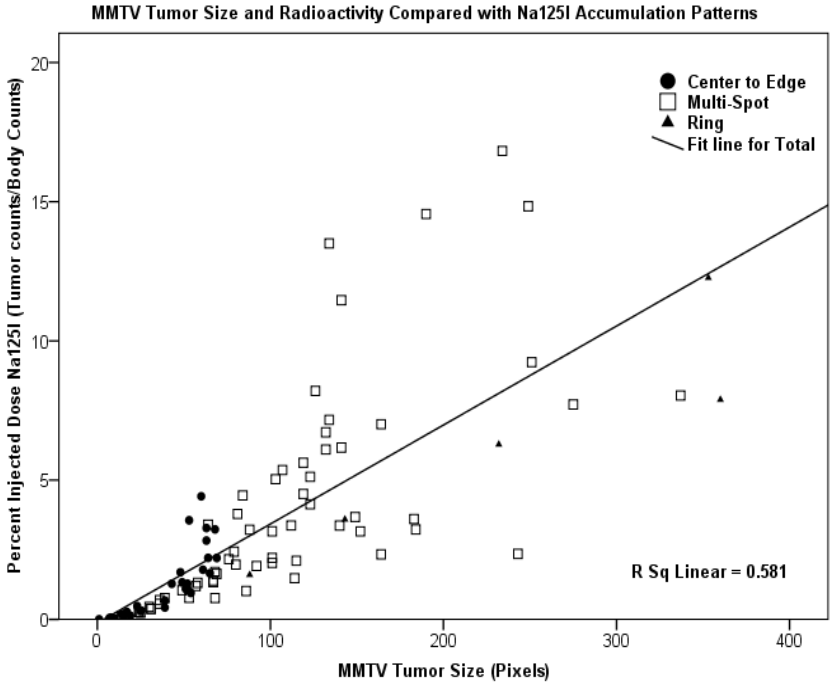

b

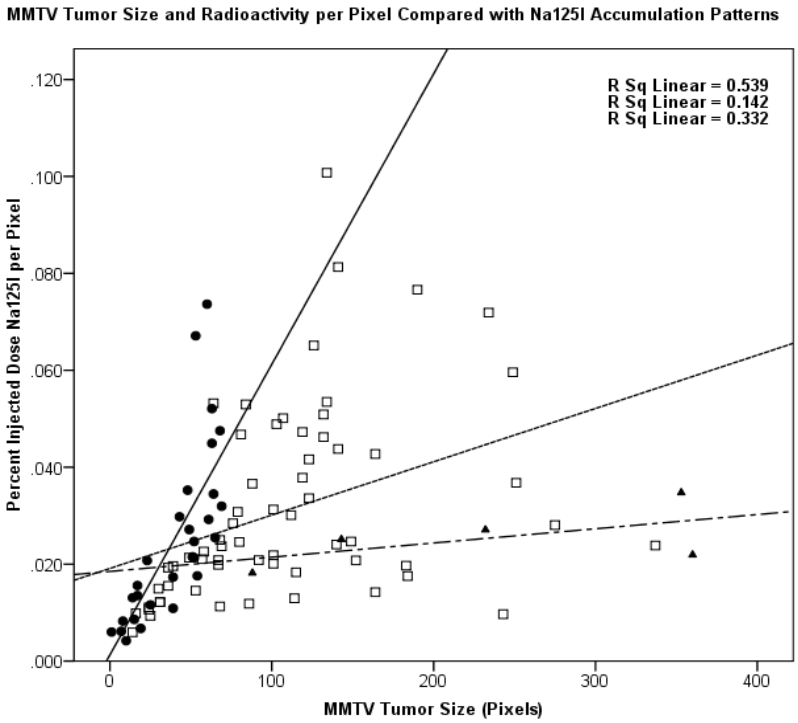

Figure 3.11. (see next page for caption)

Figure 3.11. (see previous page for figure) (a) MMTV tumor size positively correlates with tumor radioactivity based on the percent of injected dose taken in by tumors ($R^2 = 0.581$). The correlation further supports the box plot analysis (Fig. 3.10) suggesting that center to edge accumulation pattern predominates in small, less active tumors. (b) At the pixel level, center to edge pattern ($R^2 = 0.539$, solid line) tumors also positively correlate with tumor size and percent injected dose. The multi-spot pattern ($R^2 = 0.142$, dotted line) tumors appear to have no correlation between size and radioactivity. The ring pattern ($R^2 = 0.332$, dash line) tumors have a slight correlation between tumor size and radioactivity.

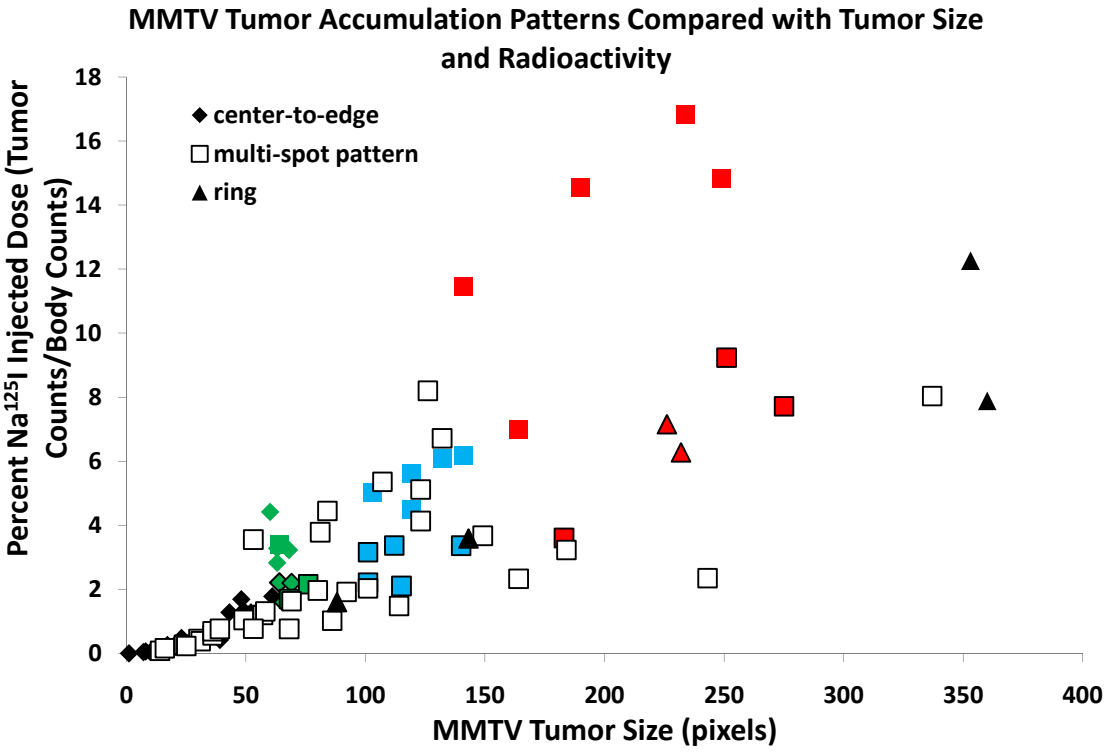

Figure 3.12.1. Based on the correlation data in Fig. 3.11, there appeared to be two trends of ^{125}I uptake as tumors increased in size. Three groups (ten tumors in each group) were selected from small (green), moderate (blue), and large (red) tumors and each cohort had to have similar size range. Trend 1 or "High" trend (green, blue or red data points without a black outline) was a steady increase in ^{125}I uptake regardless of size. Trend 2 or "Low" trend (green, blue or red data points with a black outline) was a plateau or decrease in ^{125}I uptake as tumor size increased.

Figure 3.12.2. (see next page for figure) Each cohort's dynamic ^{125}I uptake was averaged based on the High or Low trend (described in Fig. 3.12.1) within the first 30 minutes of their imaging period. (a) Small tumors (60-80 pixels) average ^{125}I accumulation were significantly ($p<0.05$) higher and the rate of accumulation was 1.5 times greater in the high trend group compared to the low trend group. (b) Moderate tumors (100-140 pixels) average ^{125}I accumulation were significantly ($p<0.05$) higher and the rate of accumulation was two times greater in the high trend group compared with the low trend group. (c) Large tumors (140-250 pixels) average ^{125}I accumulation were significantly ($p<0.05$) higher and the rate of accumulation was also two times greater in the high trend group compared with the low trend group.

a

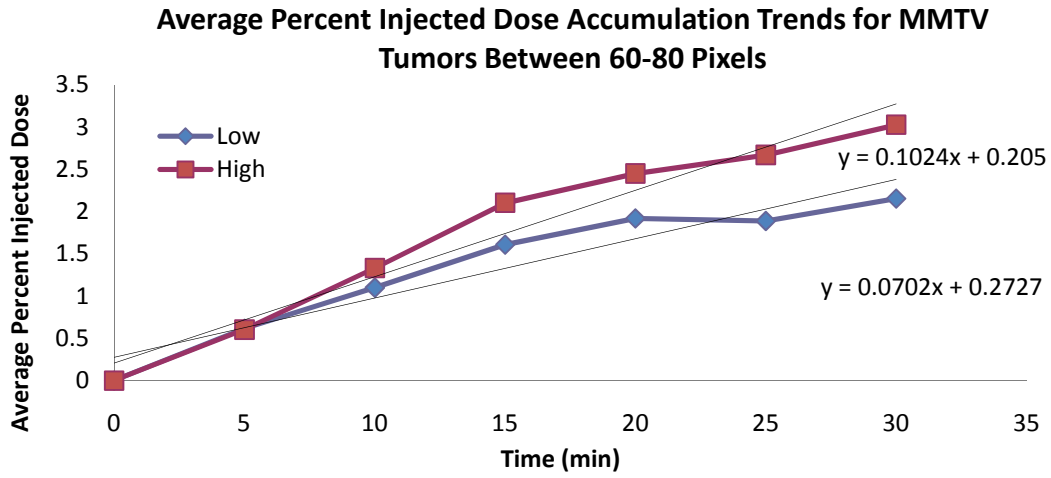
Average Percent Injected Dose Accumulation Trends for MMTV Tumors Between 60-80 Pixels
Average Percent Injected Dose
Time (min)
Low
High
y = 0.1024x + 0.205
y = 0.0702x + 0.2727
0
0.5
1
1.5
2
2.5
3
3.5
0
5
10
15
20
25
30
35

b

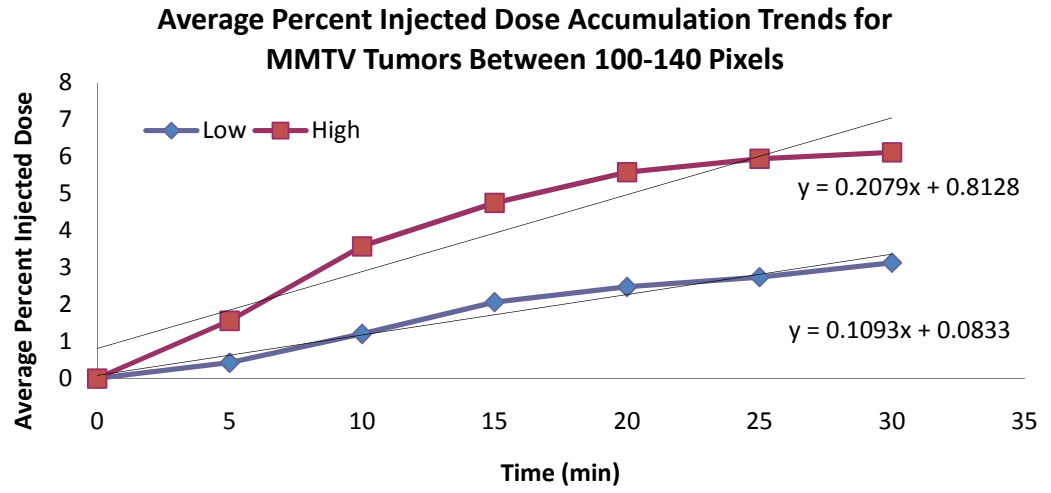
Average Percent Injected Dose Accumulation Trends for MMTV Tumors Between 100-140 Pixels
Average Percent Injected Dose
Time (min)
Low
High
y = 0.2079x + 0.8128
y = 0.1093x + 0.0833
0
1
2
3
4
5
6
7
8
0
5
10
15
20
25
30
35

c

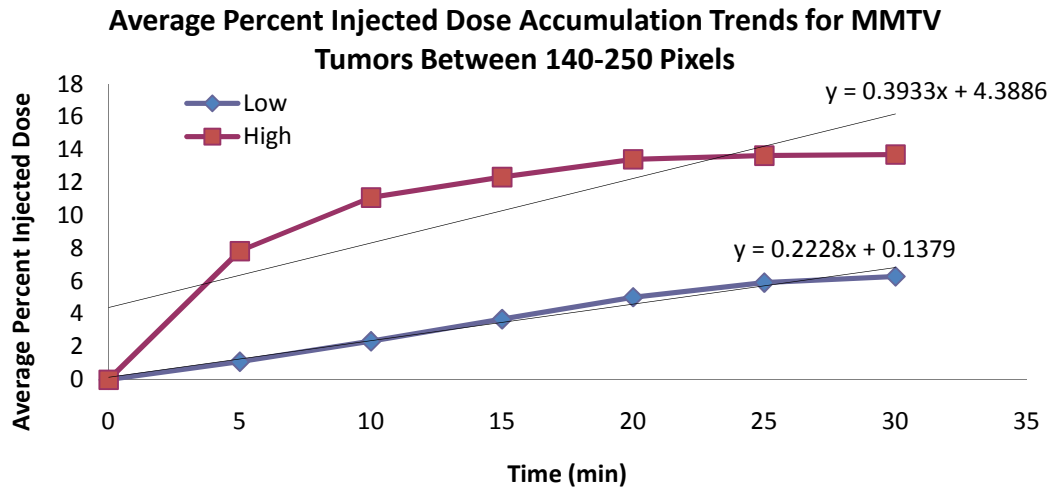
Average Percent Injected Dose Accumulation Trends for MMTV Tumors Between 140-250 Pixels
Average Percent Injected Dose
Time (min)
Low
High
y = 0.3933x + 4.3886
y = 0.2228x + 0.1379
0
2
4
6
8
10
12
14
16
18
0
5
10
15
20
25
30
35

TABLE 3.1. Component Scores for Extracted Components

	Component		
	1	2	3
Age	-.035	-.410	.025
Weight	.055	-.020	.476
Tumor #	-.062	.399	.247
Pattern	.280	-.038	.159
Tumor %ID	.435	.048	-.241
Gland	-.128	-.023	.621
Pregnancy	.083	.587	-.194
Size	.410	.048	-.017

Extraction Method: Principal Component Analysis.
Rotation Method: Varimax with Kaiser Normalization.
Component Scores.

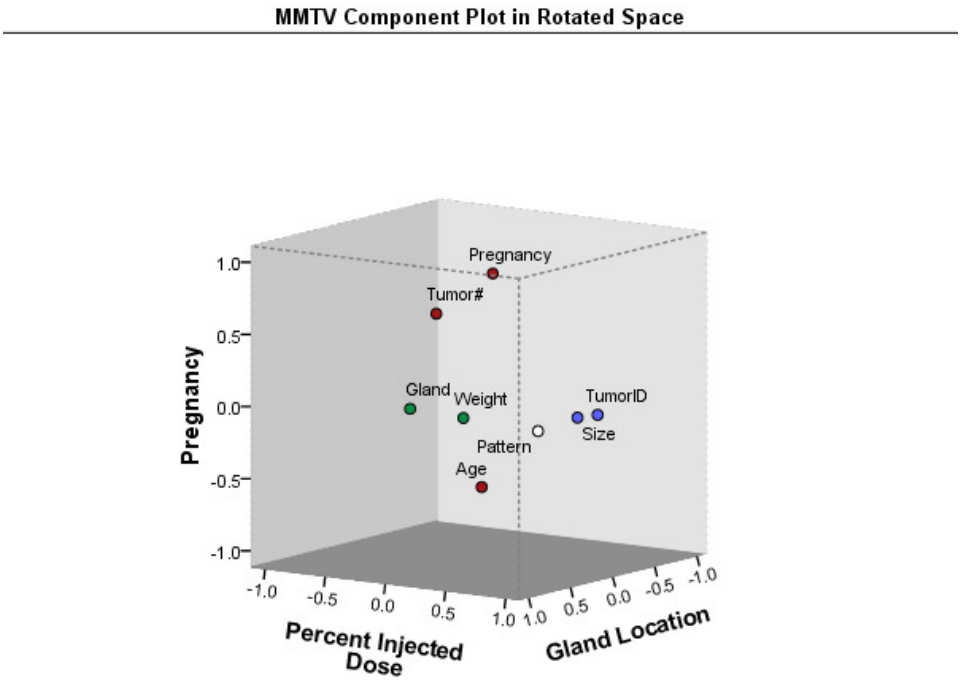

Figure 3.13. Clustered variables based on the coefficient matrix in TABLE 3.1. Three components were extracted: the percent of the injected dose tumors accumulated; the pregnancy component; and the location of the tumor at the time of imaging.

a

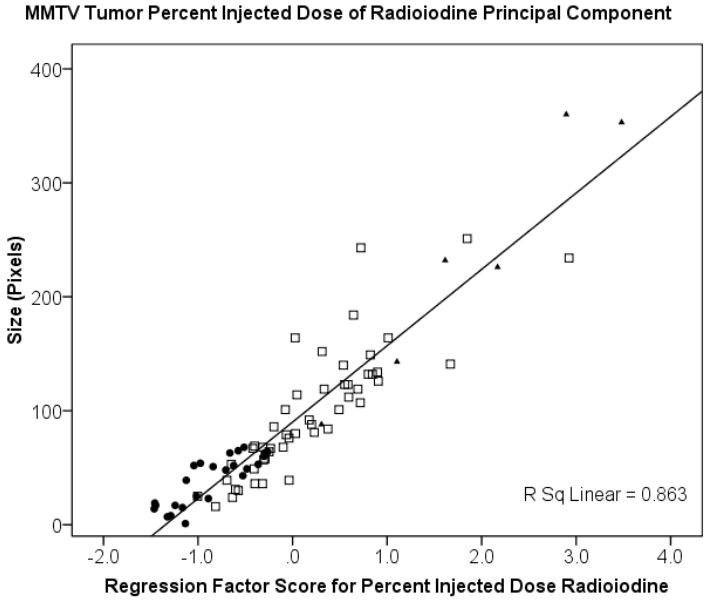

b

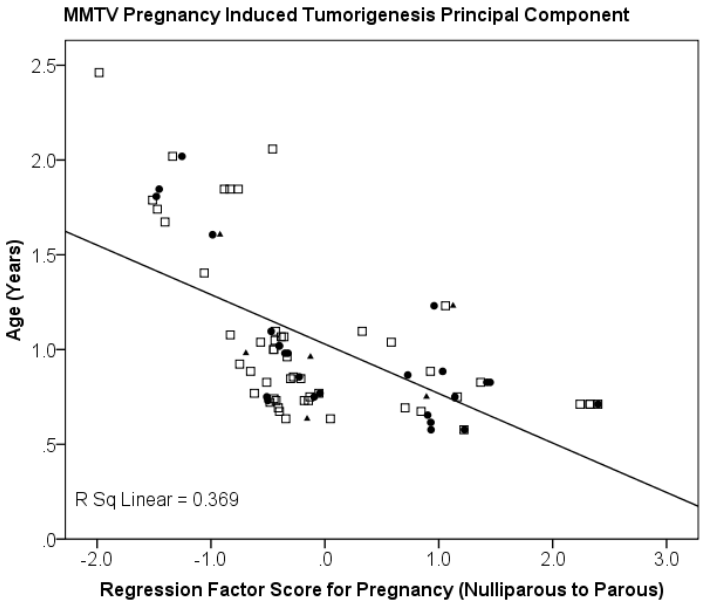

Figure 3.14. (a) The first component extracted from the PCA test suggested the percent injected dose factor scored best with tumor size (see TABLE 3.1, component 1). The graph of the factor score for component 1 with tumor size shows that tumor size is correlated with the radioactivity of the tumor (R^2= 0.863), which verifies the correlation made previously in Fig. 3.11a. (b) The second component extracted from the PCA test was the pregnancy component (see TABLE 3.1, component 2). This component scored negatively for the age of the animal. The graph of the factor score of component 2 with age suggests a negative correlation with pregnancy (R^2 = 0.369); therefore, the data indicate that MMTV tumors were imaged with mice who were older and never pregnant (left half of the graph) or with mice who were younger and pregnant/previously pregnant.

a

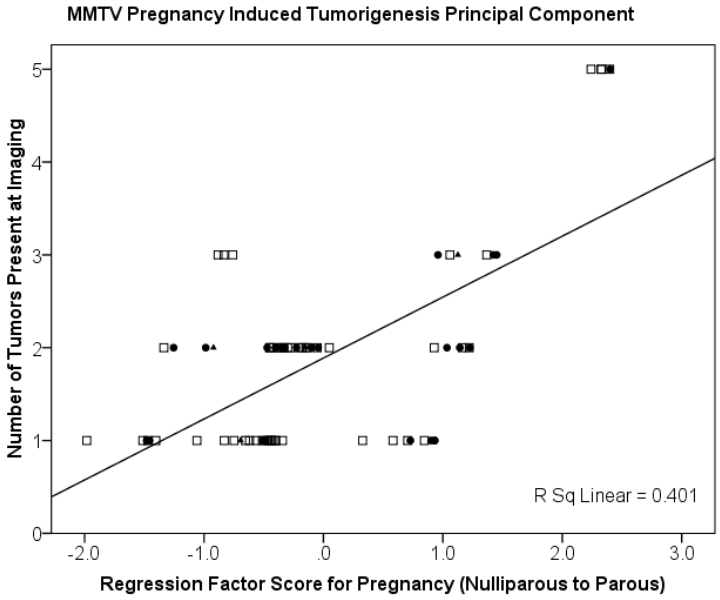

b

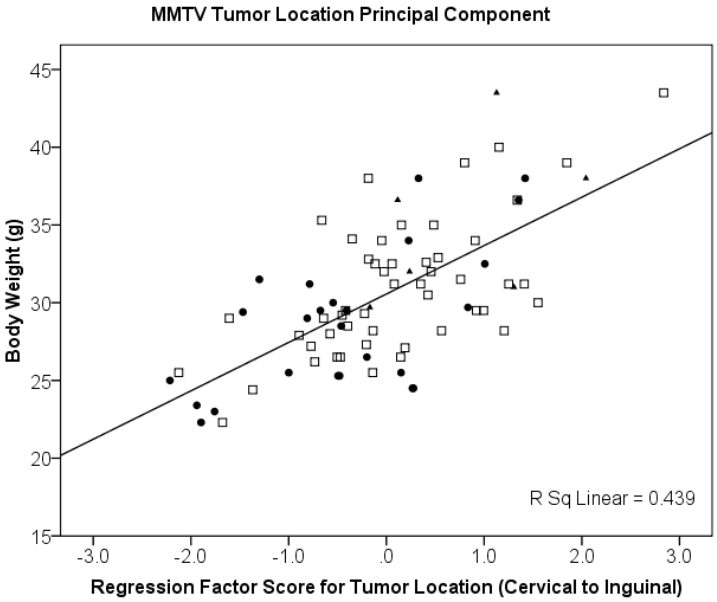

Figure 3.15. (a) The second component extracted from the PCA test was the pregnancy component (see TABLE 3.1, component 2). This component scored well with the number of tumors presented during the time of imaging. The graph of the factor score of component 2 positively correlates pregnancy with overall number of primary tumors ($R^2 = 0.401$), which suggests that pregnant MMTV mice (right side of the graph) are more likely to develop multiple tumors compared to nulliparous mice. (b) The third component extracted from the PCA test was the mammary gland component or the location of the primary tumor (see TABLE 3.1, component 3). The component scored well with the body weight of the animal. The graph indicates that there is a positive correlation with the body weight of the animal and the location of the primary tumor ($R^2 = 0.439$). These data indicate that tumors in the lower thoracic and inguinal (right side of the graph) locations of the body contribute more to the overall body weight of the animal at the time of imaging.

a

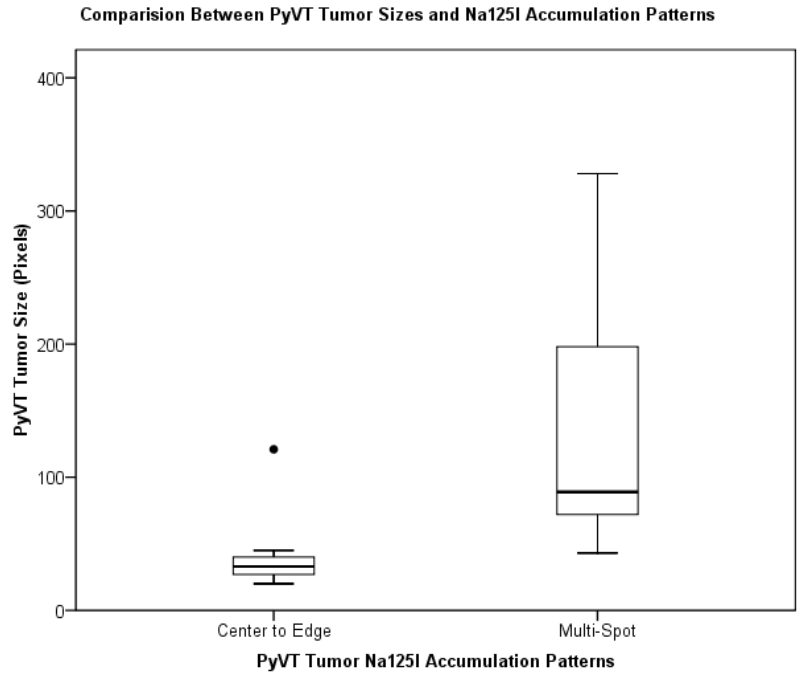

b

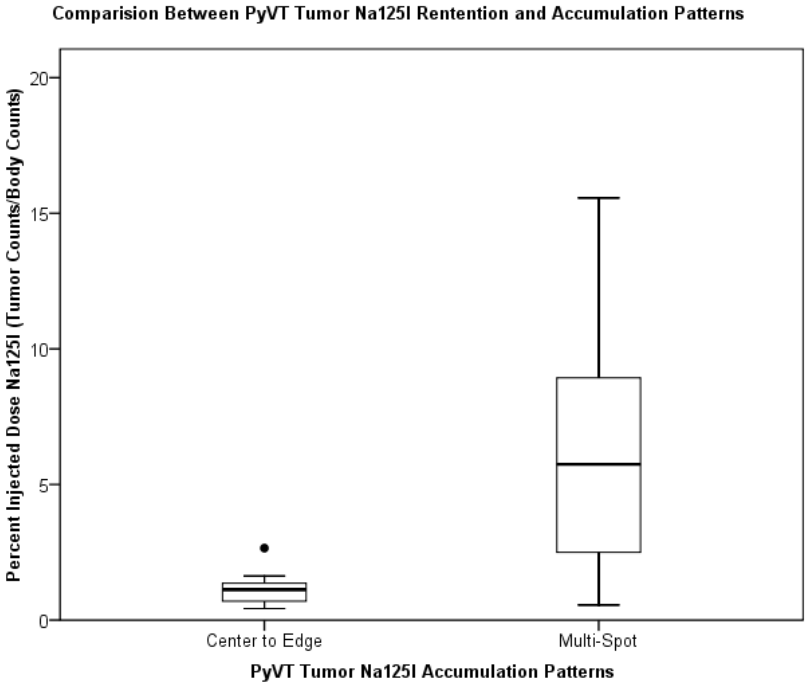

Figure 3.16. (a) Box plot analysis, comparing PyVT tumor size with two radioiodine accumulation patterns, indicates that the uptake pattern is a significant ($p<0.01$) predictor of tumor size. (b) Box plot comparison between two radioiodine accumulation patterns and the percent of injected dose for PyVT tumors suggests uptake patterns significantly ($p<0.01$) predict radioactivity in tumors as well. (The single dot represents an outlier within the center to edge group.

a

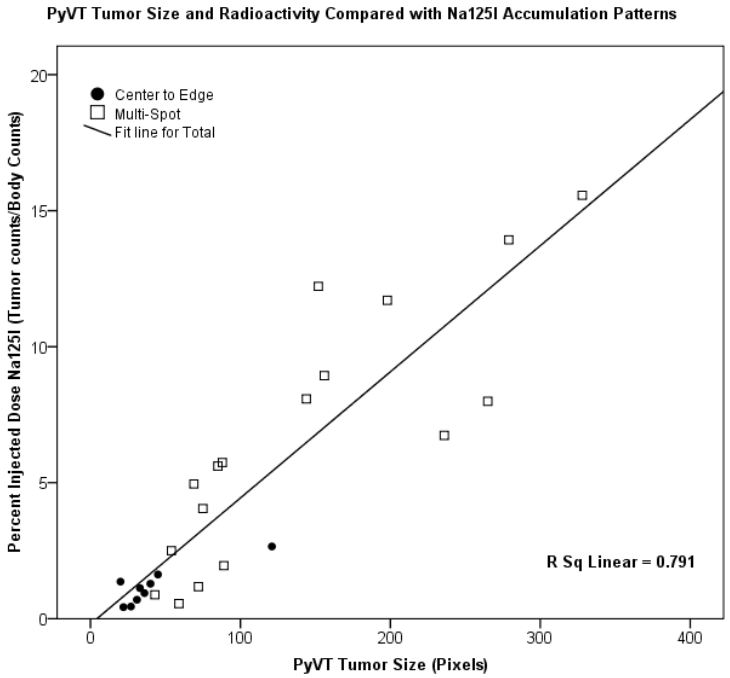

b

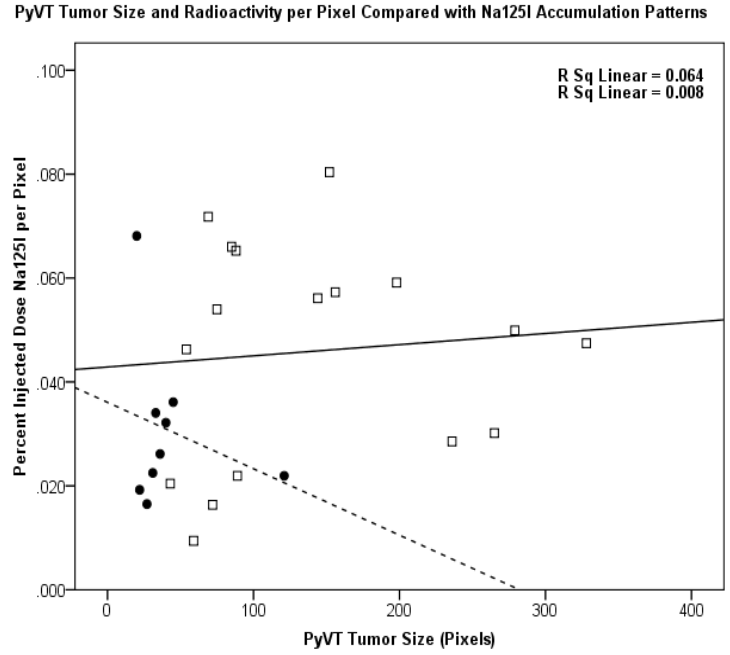

Figure 3.17. (a) PyVT tumor size positively correlates with tumor radioactivity based on the percent of injected dose taken in by tumors ($R^2 = 0.791$). The correlation further supports the box plot analysis (Fig.3.5) suggesting that center to edge accumulation pattern predominates in small, less active tumors. (b) At the pixel level, center to edge ($R^2 = 0.064$, dotted line) and multi-spot ($R^2 = 0.008$, solid line) tumors appear to have no correlation between tumor size and radioactivity, which suggests a uniform radioiodine distribution in the cells of both patterns.

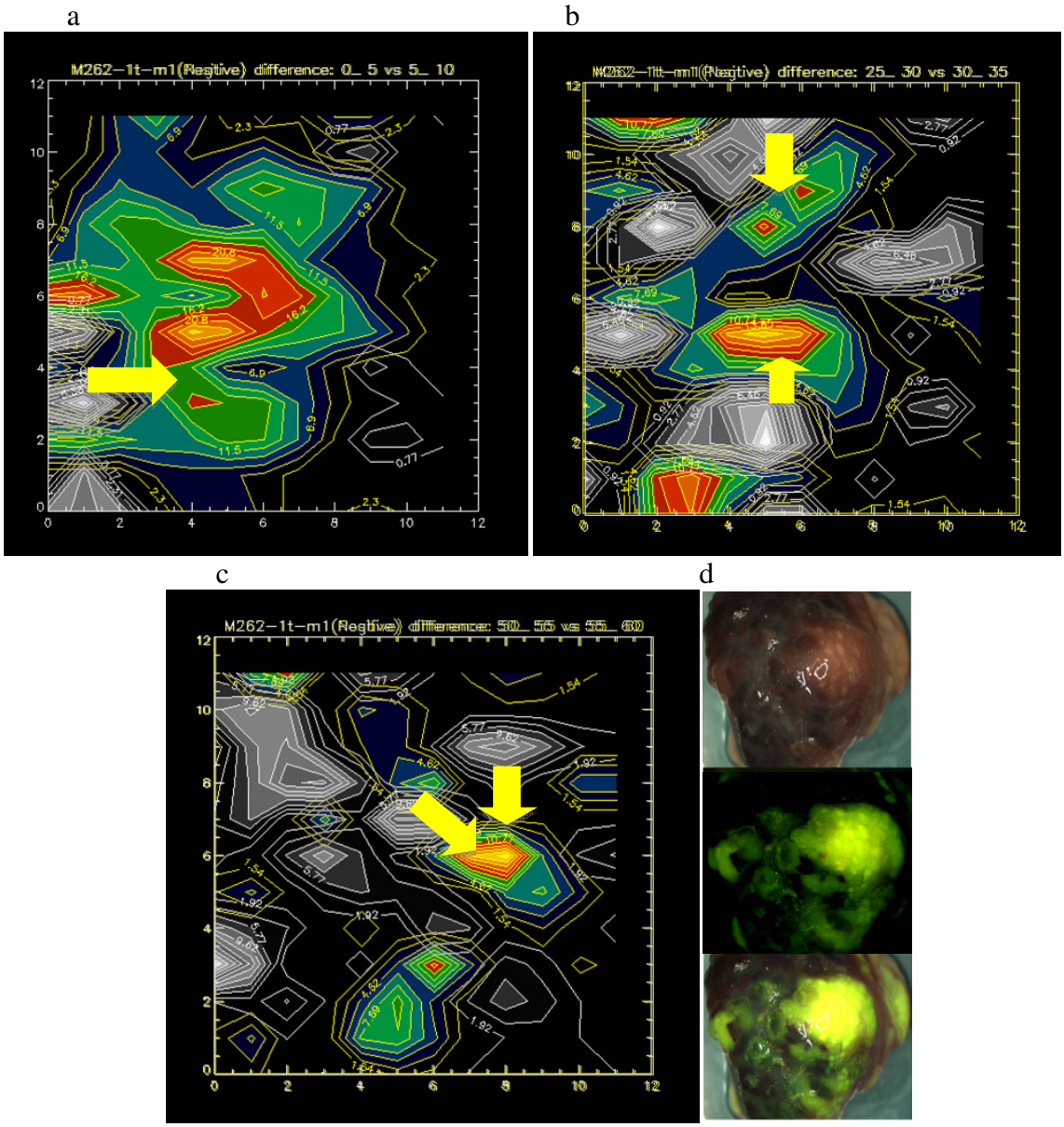

Figure 3.18. Contour plots of the change in radioactive counts within the MMTV tumor ROI. The color contour plots represent the gain of counts within the five minute time span. The gray scale contour plots represent the loss of counts within the same time span. (a) The 0-5 min vs. 5-10 min difference plot shows that early in the imaging period the tumor accumulates ^{125}I as it is presented. (b) The 25-30 min vs. 30-35 min difference plot shows more areas within the tumor are losing counts while others continue to gain. (c) The 50-55 min vs. 55-60 min difference plot shows the continuation of loss and gain that was demonstrated in (b). (d) NIS expression in this tumor shows discrete expression patterns that correlate with areas of active uptake in (a), (b), and (c). (The yellow arrows in (a), (b), and (c) represent the presumed pathway of ^{125}I transfer in a mammary tumor. The pattern shows ^{125}I transfer from the outer edge of the tumor toward the central mass of the tumor.)

TABLE 3.2. MMTV Tumor Development Study

Mouse (tumor location)	Initial Tumor Size (pixels)	Initial Pattern Type	Post Imaging (days)	Tumor Size (pixels)	Pattern Type	Change in Tumor Size (Δpixels)	Rate of Tumor Growth (Δpixels/days)
1 (RT)	13	C-E	7	23	C-E	10	1.4
2 (RI)	22	C-E	4	41	C-E	19	4.8
2 (LT)	39	M-S	4	69	M-S	30	7.5
3 (LT)	35	M-S	7	69	M-S	34	4.9
3 (RT)	33	M-S	7	94	M-S	61	8.7
4 (LT)	31	M-S	6	45	M-S	14	2.3
4 (RI)	68	M-S	6	65	M-S	-3	-0.5
5 (RT)	159	M-S	12	407	M-S	248	20.7
5 (LT)	13	C-E	12	23	M-S	10	0.8
6 (RT)	60	M-S	22	52	M-S	-8	-0.4
6 (RT)	52	M-S	27	58	M-S	5	0.2
7 (RT)	24	C-E	14	52	C-E	28	2.0
7 (RT)	52	C-E	21	107	M-S	55	2.6

(RT = right thoracic, RI = right inguinal, LT = left thoracic, C-E = center-to-edge, M-S = multi-spot)

a

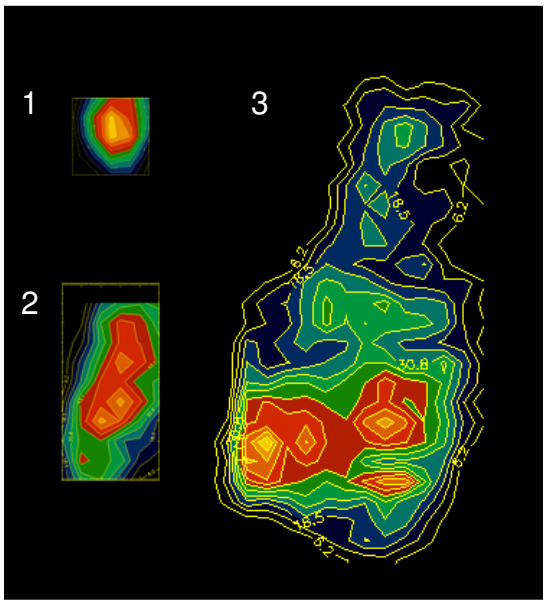

b

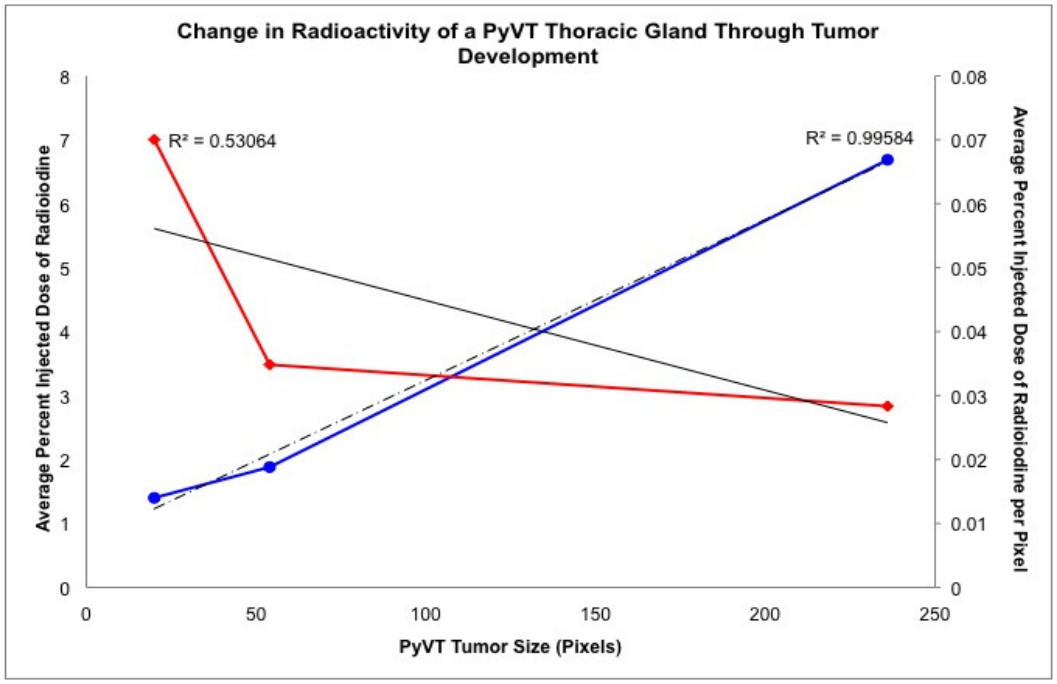

Figure 3.19. (a) Contour plots of a PyVT mouse imaged three times to monitor the change in tumor radioiodine uptake with tumor progression. Radioiodine uptake begins as a center to edge pattern (a1), which progresses to a multi-spot pattern (a2 and a3). Patterns in (a1 and a2) have been scaled down in relation to final tumor size (a3). (b) Analysis of PyVT tumor development with regard to tumor size and radioactivity in the mammary gland. There was a positive correlation (R^2 = 0.996) with tumor size (x-axis) and the percent of radioiodine the tumor accumulated (blue line, y-axis to the left). At the pixel level, which represents groups of cells in the tumor, there appears to be a negative relationship (R^2 = 0.531) between tumor size (x-axis) and the percent of radioiodine groups of cells of the tumor accumulated (red line, y-axis to the right).

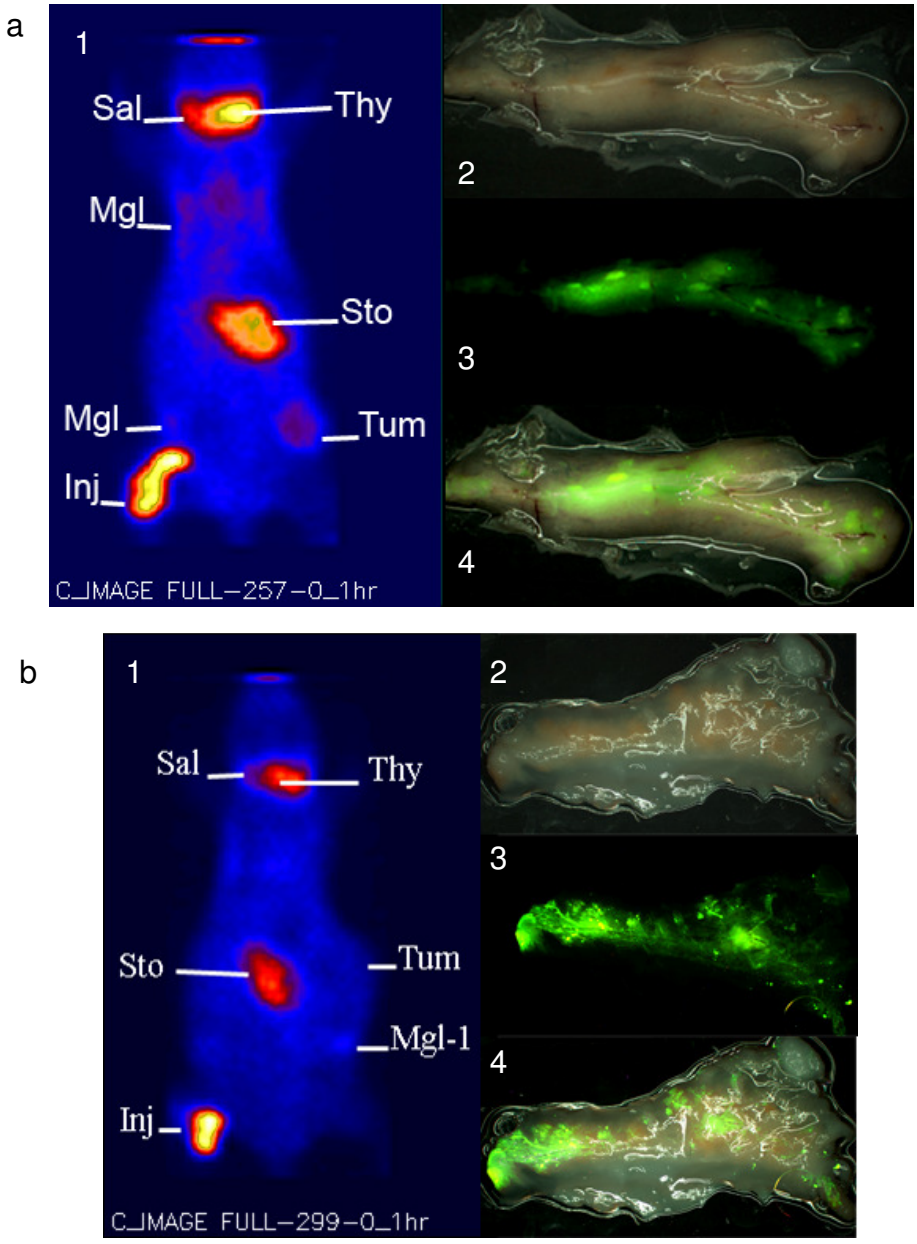

Figure 3.20. (a) The gamma image of a MMTV tumor bearing mouse shows ^{125}I accumulation in mammary glands other than the primary tumor (a1). The right inguinal mammary gland (a2 *ex vivo*) contralateral to the primary tumor was analyzed for NIS protein expression (a3). NIS protein localization was expressed in discrete patterns throughout the mammary gland (a3 and a4 overlay). (b) The gamma image of a non-mammary tumor shows no ^{125}I uptake in the tumor but in the left inguinal mammary gland below the tumor (Mgl-1 b1 and b2 *ex vivo*). Immunolocalization confirmed that NIS protein was expressed in the mammary gland in clusters throughout the mammary gland (b3 and b4 overlay). (Sal = salivary glands, Thy = thyroid, Mgl = mammary gland, Tum = tumor, Sto = stomach, Inj = injection site)

a

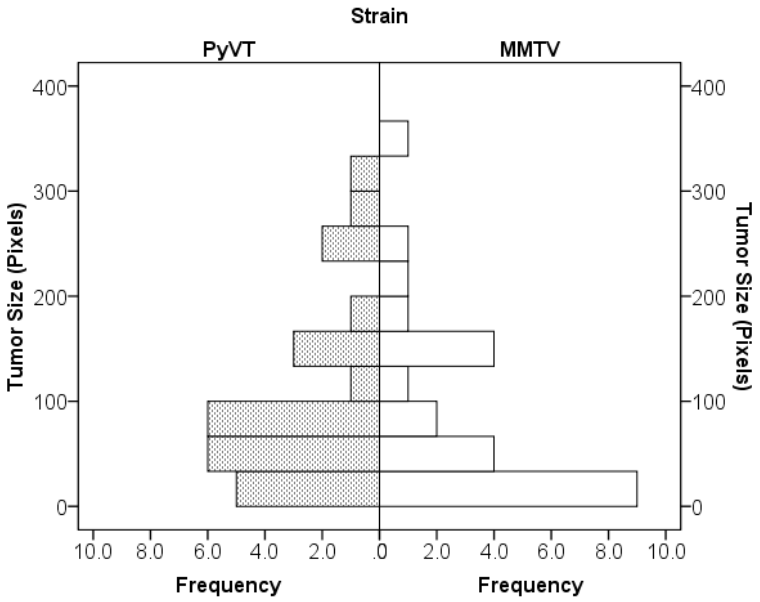

b

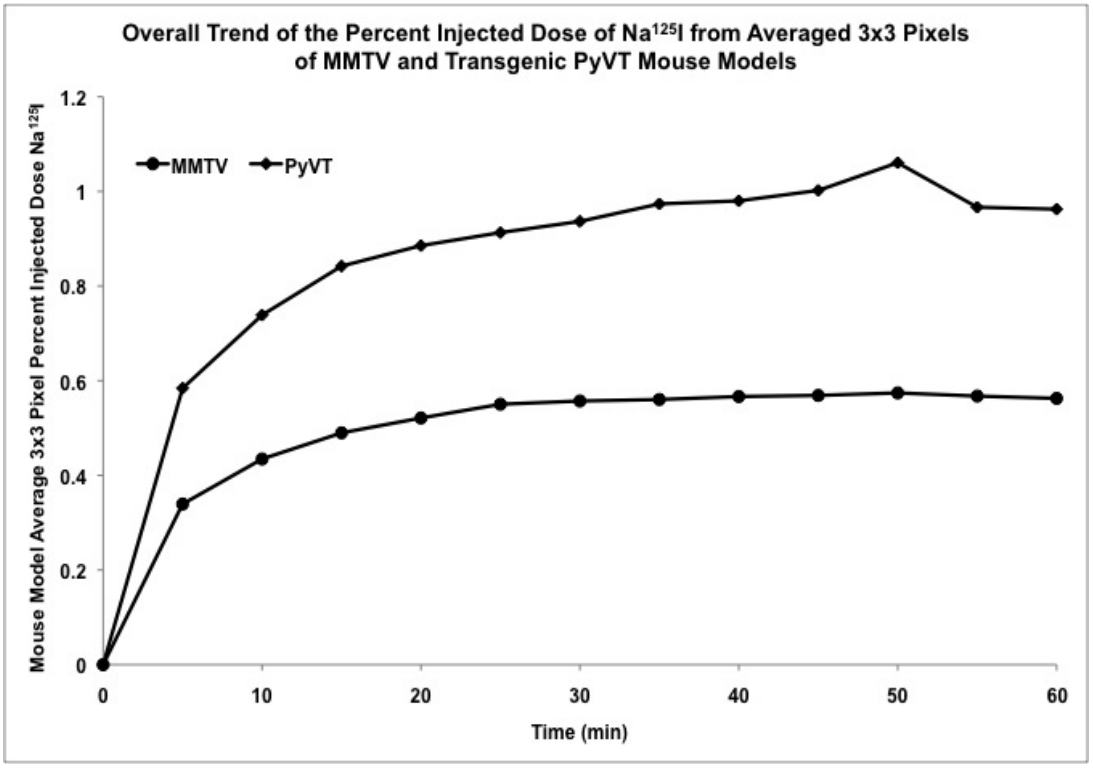

Figure 3.21. (a) For the comparison study, the distribution of MMTV and PyVT tumors were similar in size. (b) The overall average of the percent injected dose of ^{125}I in tumors of both models indicate radioiodine accumulation rates were significantly ($p<0.01$) higher in the PyVT model.

CHAPTER 4

DISCUSSION

In an effort to address the growing need for effective high-performance imaging modalities that are specifically designed for breast cancer imaging we tested our novel gamma camera to target the molecular function of NIS in the mammary tumors of MMTV and PyVT mice. These results indicated that the immunohistochemical expression of NIS was coincident with the patterns of radioiodine biodistribution in MMTV tumors as well as in PyVT tumors and normal mammary glands.

NIS expression in PyVT tumors was reported at the mRNA (Kogai et al., 2004) and protein level (Knostman et al., 2004), which was further supported in whole mount staining for NIS in PyVT tumors presented here. In the three dimensional comparison between optical NIS localization and the contour plot (see Fig. 3.5) there appeared to be more available NIS protein in the lower portion of the tumor which did not fully correlate with the amount of radioiodine accumulated in the same area. In human breast cancer there appears to be disparity between NIS expression and actual radioiodine uptake for treatment (Beyer et al., 2008; Renier et al., 2009). Specifically, Knostman et al. (2007) have found that in MCF7 cells PI3K activation of NIS leads to the expression of underglycosylated NIS which cannot traffic to the plasma membrane and PI3K inhibits radioiodine uptake of exogenous NIS. Since PyVT tumors both share similar morphological characteristics with human breast cancer and frequently have activated

PI3K pathway, this post translational processing may account for the slight discrepancy between the available NIS protein and the amount of radioiodine that was accumulated.

In lieu of performing tail snips for genetic screening, which could cause undue harm to neonates, PyVT mice were housed with their wild type littermates in order to examine if the gamma camera could identify transgenic mice and in effect image early tumor development. According to the study performed by Lin et al. (2003) roughly 60% of PyVT mice have premalignant hyperplasias by four to six weeks of age. Therefore, the screen at five and seven weeks of age matched well with the proposed critical period. Not only was the gamma camera able to screen animals effectively for potential genotype, but also very early tumor development was detected at the premalignant hyperplastic stage. Continued research is warranted as to the earliest the gamma camera can detect transgenic mice. Early screening at three weeks of age, as proposed by (Guy et al., 1992) when lesion may develop, may further validate the gamma camera's efficacy, but concerns over sedating such young animals will have to be addressed. What is unknown is whether the gamma camera can screen male transgenic mice for potential genotype. It has been reported that PyVT males do express the transgene and develop adenocarcinomas in their mammary glands and testes (Guy et al., 1992), therefore, more testing with the gamma camera could resolve whether lesions in the seminal vesicles accumulate iodine at detectable levels for male screening. Also for mouse husbandry purposes it would be advantageous to identify transgenic males for establishing breeding founders.

MMTV tumors have unique distribution patterns of radioiodine uptake that can be correlated with overall tumor size and radioactivity. The data indicated that small tumors

(<75 pixels) were primarily associated with a center to edge uptake pattern and also resulted in less total activity accumulation within the tumor. Moderate and large tumors (>200 pixels) all were associated with the multi-spot or ring (primarily in very large tumors) patterns which were statistically significantly correlated with tumors later in development. The observed radioiodine uptake patterns are likely due to not only to NIS expression, but also to a range of biochemical processes in the tumor. For example, small tumors with the center to edge uptake pattern are solid masses which give the uniform pattern. However, when the tumor becomes larger more areas become hypoxic and as a result parts of the tumor become necrotic which may contribute to the multi spot patterns of radioiodine accumulation and NIS patterning. Preliminary data from a multi-spot tumor stained for apoptosis and necrosis suggest that throughout the whole tumor there are discrete areas undergoing programmed cell death (Fig. 4.1). Furthermore, analyzing the marker associated with the response to hypoxic conditions within the tumor could reveal critical information of tumor pathology. HIF-1α in relation to NIS expression within a multi-spot tumor also suggests that both are expressed in discrete patterns within the tumor (Fig. 4.2d-f). Interestingly, whole mount immunolocalization for HIF-1α indicates that the protein is primarily expressed in putative normal tissues surrounding the primary tumor (Fig. 4.3). This supports current literature that suggests HIF-1α is expressed during tumorigenesis to immortalize cells (Han et al., 2008). In effect, HIF-1α expression in the normal gland attached to the primary tumor could indicate the portion of the gland that may be initiating tumorigenesis.

PyVT mice also have different patterns of radioiodine accumulation correlating with overall tumor size. The shift from a center to edge pattern at early stages of

premalignancy to multi-spot suggests that the gamma camera can detect the shift to malignancy. Maglione et al. (2001) described the topographical zones of the PyVT gland in which the zone closest to the nipple was the first to develop hyperplastic nodules. With gamma imaging it may be possible to identify these topographical zones by examining the contour plots of tumors in which multi-spot patterns of radioiodine uptake would suggests that the hyperplastic lesion had spread from the nipple into the mammary fat pad.

Moreover, a PyVT mouse that was imaged three times to monitor tumor progression exhibited both an increase in tumor size and radioiodide uptake in the whole tumor. However, at the pixel level which would represent clusters of cells there was a steady decrease in the radioiodine accumulation associated with tumor progression. It has been well established that as tumors develop in the PyVT model there are losses in estrogen and progesterone receptor status in the tumor (Lin et al., 2003). Recently, an estrogen responsive element that binds ERα was identified in the promoter region of the NIS gene (Alotaibi et al., 2006), which suggests that estrogen has a role the expression of the NIS gene. Our data suggest that the decrease in radioiodine accumulation per pixel in late stage PyVT tumors may be an indication of the loss of the ER which would affect NIS protein expression and radioiodine accumulation.

As an alternative to analyzing tumor pattern, size, or radioactivity the results implied that rates of radioiodine accumulation could be very informative in the case of moderate and large MMTV tumors. The data suggested that MMTV tumors had two fates that corresponded with tumor progression. The first trend was that as some tumors grew in size they steadily increased the amount of radioiodine they accumulated, in contrast

some other tumors with the same size range appeared to reach a plateau or lowered level of radioactivity. Cohorts from small, moderate, and large tumors that were associated with either trend were analyzed to get the average rate of radioiodine accumulation for "high" and "low" trend groups that were matched for size. The data implied that, in general, moderately large tumors (>100 pixels) that had a rate of accumulation by a factor of 2 more than the low group were correlated with the "high" trend group. These data suggest that in addition to size, pattern, and radioactivity, rates of radioiodine accumulation also can predict tumor type.

Considering the wealth of data that was collected from the 58 mice imaged in this study, a principal component analysis was used to reduce the data variables in order to observe any data relationships that may have been missed. The PCA analysis extracted three major components that accounted for over 60% of the variance in all the data. These components involved percent of radioiodine accumulated by the tumor, the pregnancy factor, and the body location of the primary tumor site. The principal component analysis confirmed our initial observations that tumor size and the percent injected dose accumulated were highly correlated. The association of pregnancy with the age of the animal demonstrated that tumorigenesis is specifically associated with old nulliparous or younger pregnant/previously pregnant mice is consistent with the earlier observations that chances of tumor development increases with parity due to hormone response (Cardiff and Kenney, 2007; Kordon, 2008). Additionally, the pregnancy component was also correlated with the number of tumors a mouse has at the time of imaging. The third component indicated that that the location of the mammary tumor was correlated with the body weight of the animal was unexpected. Based on the PCA scores, mice that have

cervical or upper thoracic tumors had a lower body weight than mice with tumors in the lower thoracic, inguinal, and abdominal regions. This could be influenced by the fact that inguinal tumors are harder to visually detect because these tumors are obscured ventrally until late in tumor development. Therefore, this correlation could be strongly influenced by current animal husbandry practices that restrict animal handling to cage changes every two weeks.

Difference plots have the potential to be very informative by indicating not only areas of radioactivity gain and loss within a tumor, but also the primary locations of functional NIS expression. The pathway of radioiodine transfer within a tumor likely defines the sites where the NIS protein is actively accumulating radioiodine. It is also possible that because NIS activity can be blocked with high doses of potassium iodide (KI) that saturate the thyroid gland with iodine (Hammond et al., 2007) the net loss of activity observed in difference plots could be due to NIS saturation. Once the protein is saturated any residual isotope would wash away and appear as a loss in activity. Furthermore, an hour imaging session may be long enough to detect radioiodine washout from the tumors. Early radioiodine washout also has been linked to poor prognosis of lesions because the therapeutic dose does not remain in targeted tissues (Hung et al., 2009).

Of note was the applicability of the gamma camera to detect radioiodine accumulation in putative normal mammary glands of tumor-bearing mice. Under normal conditions NIS expression is tightly regulated in order to add iodine to milk, and during this time is sensitive to radioiodine uptake (Tazebay et al., 2000). Therefore, these data suggest that when a tumor develops there may be a disregulation on gland tissue to

overexpress NIS. In the MMTV model Wnt, fibroblast growth factor (FGF), and notch signaling are activated during tumorigenesis (Theodorou et al., 2007), and genes specific to each pathway have been linked to regulating components of NIS expression the thyroid (Boelaert et al., 2007; Ferretti et al., 2008; Kim et al., 2007b). This suggests that the overexpression of either the Wnt, or FGF pathway in the MMTV model could cause a broad effect on other mammary glands. Furthermore, parous MMTV-infected mice form neoplastic hyperplastic alveolar nodules (HANs) that along with primary tumors can become independent of hormonal regulation (Kordon, 2008). Taken together, these data indicate that the gamma camera may detect early tumor states in the MMTV model.

The efficacy of gamma imaging to detect mammary metastasis requires further study as well. In the PyVT model the majority of females exhibit lung metastasis by three months of age (Guy et al., 1992). Due to the fact these metastasis are of mammary origin, metastatic radioiodine accumulation could possibly be detected with the gamma camera if the foci were large enough and not obstructed by the tumor proper. Recently, reports have indicated that the disruption of the src gene (SRC-1) in PyVT mice suppress metastasis but not tumor formation, suggesting that the src pathway which is also upregulated in the PyVT model is involved with the final migration of cancer cells to the lungs (Wang et al., 2009).

In comparison studies PyVT mice significantly accumulated more radioiodine and at a two times higher rate than spontaneous MMTV mice bearing multiple tumors. PyVT tumor histology has been reported to be different than that of spontaneous tumors induced by MMTV (Cardiff et al., 2000a). Our data suggest that biology behind the differences in tumor morphology can be detected *in vivo*. More comparative studies

between the two models would greatly resolve how naturally occurring tumors differ from tumors genetically engineered.

FUTURE DIRECTIONS

Using Other Iodinated Ligands for Gamma Imaging

There are many commercially available ligands that can be iodinated and imaged with the gamma camera. In preliminary trials we have imaged MMTV mice with iodinated 17β-estradiol, VEGF, and EGF. While our data do not show tumor specificity for estrogen or VEGF, there are promising results when imaging with EGF. Four hours after administration of the radioactive EGF gamma imaging revealed that the MMTV tumor had bound ligand (Fig. 4.4). In addition, immunohistochemical data suggest that amphiregulin (AREG), an EGF family member, is expressed in MMTV tumors along with NIS (Fig. 4.2a-c). AREG has been shown to be overexpressed in breast cancer and will bind to the EGF receptor (McBryan et al., 2008). This could be very informative with regard to the PyVT transgenic line which has been shown to increasingly overexpress the EGF receptor (HER2/neu) with tumor progression (Lin et al., 2003). Moreover, targeting the overexpression of HER2/neu in PyVT tumor progression with iodinated AREG or EGF would provide further *in vivo* information of the molecular process of breast cancer.

Microarray, Real-Time PCR and Gene Expression

An important aspect of continued molecular research with regard to *in vivo* imaging is the global expression of genes implicated in both mouse and human breast cancer. Custom designed microarray gene chips and real-time PCR arrays with genes associated with mouse breast cancer, estrogen receptor signaling, and breast cancer prognosis (SABiosciences) are available commercially. Employing these approaches would allow the investigation of which genes associated with breast cancer are expressed in MMTV and PyVT tumors. With that information a correlation could be made between our sodium iodide symporter real-time data in tumors to validate whether the sodium iodide symporter/activity could serve as a biomarker for murine breast cancer. These data would potentially provide a wealth of data particularly to those genes that are co-expressed with the sodium iodide symporter, and this would suggest which gene products might be iodinated for future *in vivo* gamma camera imaging.

Detailed earlier, once a putative gene has been identified for *in vivo* imaging, subsequent immunohistochemistry on corresponding proteins could be done on tumor tissues to derive the molecular pattern related by the gamma image. Assessment of the protein localization coincident with the sodium iodide symporter gamma camera position and pattern would provide great value to application of the camera in producing an *in vivo* molecular "signature" of tumorigenesis.

Computer Pattern Recognition Programs for *In Vivo* Studies

The *in vivo* study on MMTV mammary tumors has implicated that ^{125}I incorporation patterns correlate with overall tumor size. These patterns have the potential

to provide powerful information about the biology of the tumor at the time in which it was imaged. Unfortunately, a drawback to this process was that all uptake patterns were assigned manually. In an effort to reduce any type of bias in pattern assignment computer based programs could be designed to select the ^{125}I uptake pattern immediately after imaging.

In mammography and ultrasound automated segmentation of region of interest (ROI) identifies tumor mass morphology by factoring in edge gradient and pixel intensity in a contour plot (Cui et al., 2009; Song et al., 2009). In addition, tumor volume predictors using segmentation have been used in PET (Drever et al., 2007). In PET and SPECT the volume of interest (VOI) predicts and quantifies tumor size and radionuclide uptake based on designed algorithms (Blackwood et al., 2009; Wahl et al., 2009).

Current computer based pattern recognition programs regardless of imaging modality require calculated standards to assess tumor morphology patterns. Incorporating some form of computer based pattern recognition of ^{125}I uptake would only increase the validity of *in vivo* gamma imaging.

CONCLUSION

Here we describe the *in vivo* efficacy of a novel gamma camera to image ^{125}I metabolism in mammary tumors of the MMTV and PyVT mouse models. Our data suggest that ^{125}I accumulation, as detected by the gamma camera, is highly correlated to areas within tumors where the sodium iodide symporter is expressed. In addition, the gamma camera can be readily applied to genetically engineered mouse models, which share similar tumorigenesis pathways and histology with human breast cancer. Our

results also indicate that the classifiable heterogeneity present in dynamic gamma camera images may correlate with specific patterns or signatures of gene expression that, in turn, indicate tumor subtype and progression. These data may allow investigators to develop an effective and sensitive system of *in vivo* imaging of molecules and metabolism that reflect the molecular signature of a tumor in real time. Our system may provide a means for early detection, ideally even a precancerous state before malignancy develops, and a method to assess the overall state of a tumor with the goal of predicting the best therapeutic regime and following the efficacy of the therapy in real time by examining specific molecular targets.

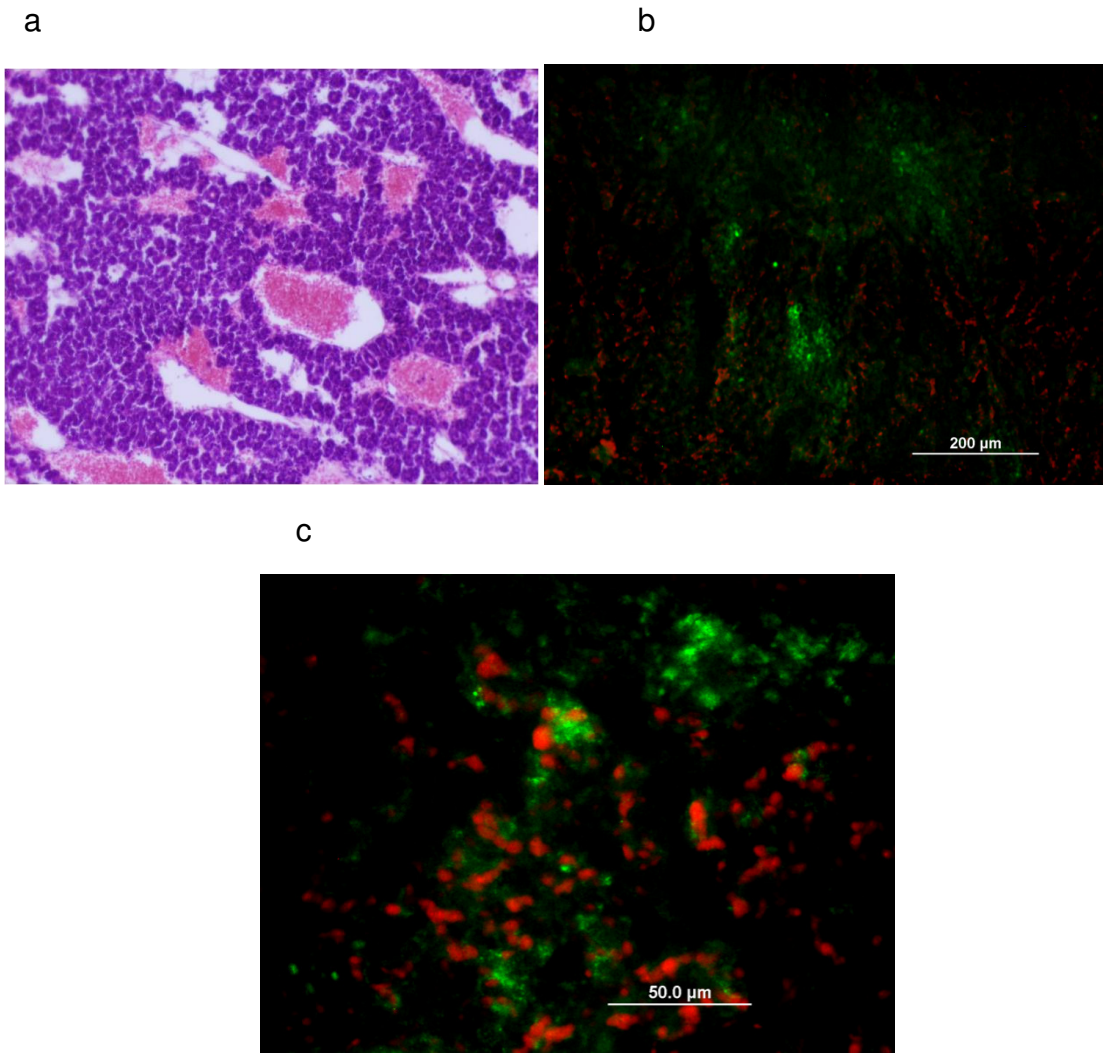

Figure 4.1. (a) Low power (10x) H&E stain of a cryosectioned multi-spot tumor showing necrotic pools (red stain) within the tumor tissue. (b) Low power (10x) apoptosis and necrosis stain on a cryosectioned multi-spot tumor showing discrete areas necrotic (red) and apoptotic (green) cells. (c) High power (40x) view of the apoptotic (green) and necrotic (necrotic) cells of a multi-spot tumor.

Figure 4.2. (see next page) (a) Low power (20x) immunohistochemical staining for AREG in a multi-spot tumor. (b) Low power (20x) localization of NIS protein in the same field of view as (a). (c) Overlay image of (a) and (b) showing the discrete expression patterns of AREG and NIS. (d) Low power (20x) localization of HIF-1α protein in a different multi-spot tumor. (e) Low power (20x) immunolocalization of NIS protein in the same field of view as (d). (f) Overlay image of (d) and (e) showing the discrete expression patterns of HIF-1α and NIS.

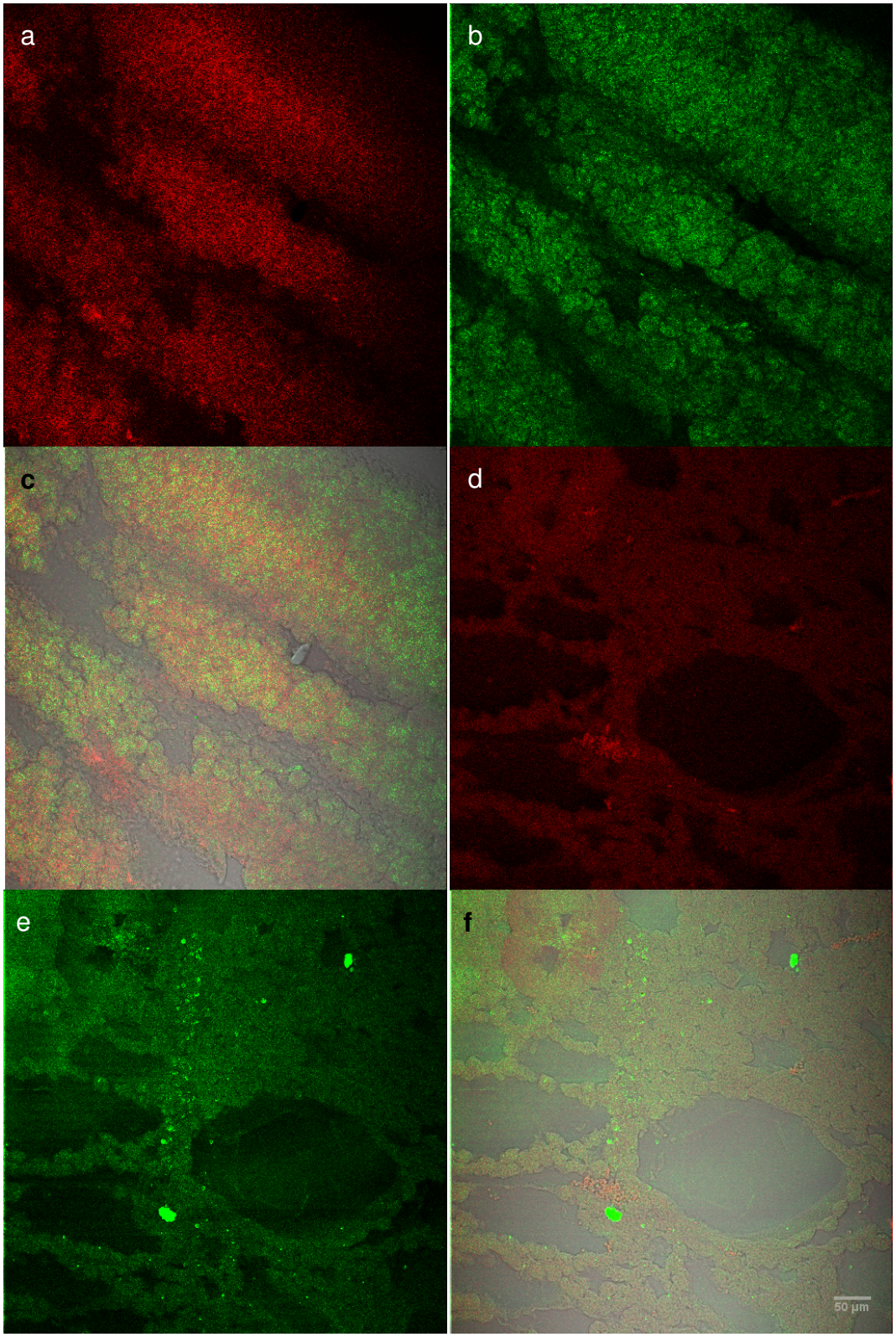
a
b
c
d
e
f
50 µm

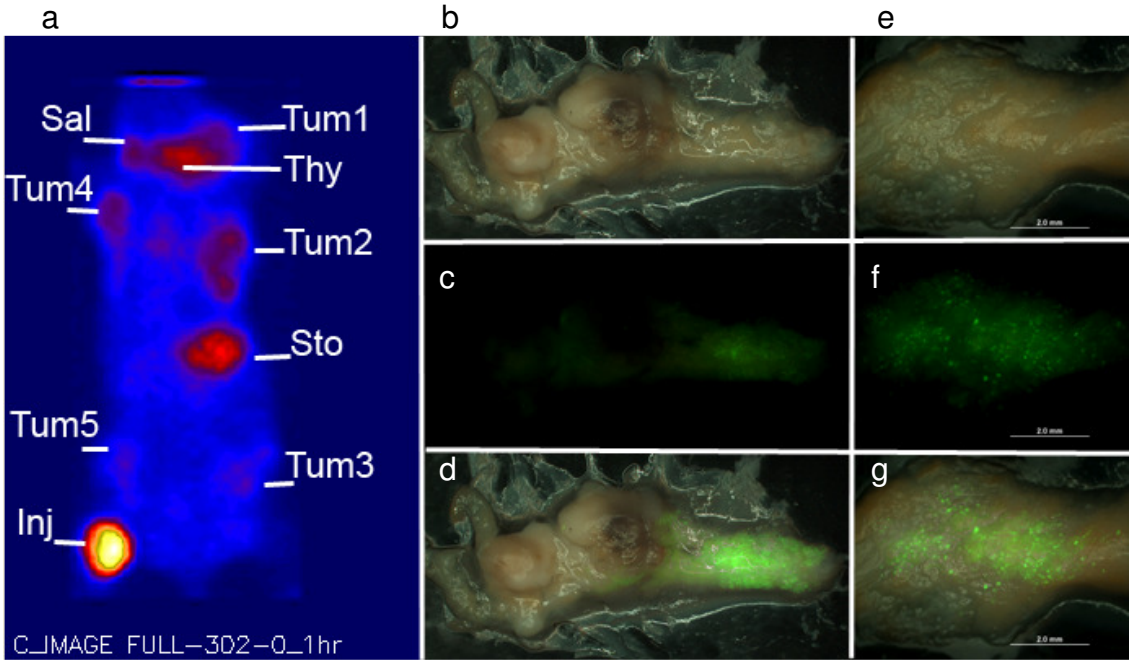

Figure 4.3. (a) Gamma camera detects five tumors in an MMTV animal. (b) Bright field image of the left inguinal tumor (a, Tum3). (c) Immunolocalization for the HIF-1α protein appears to be primarily expressed in the normal portion of the mammary gland next to the tumor. (d) Overlay image of (b) and (c) further shows that the putative normal gland next to the tumor is where HIF-1α is expressed. (e) 2x bright field image of the mammary gland next to the primary tumor. (f) 2x localization of HIF-1α protein in the mammary gland. (g) Overlay image of (e) and (f) showing the discrete expression pattern of HIF-1α in the mammary gland next to the primary tumor. (Sal = salivary glands, Thy = thyroid, Tum = tumor, Sto = stomach, Inj = injection site)

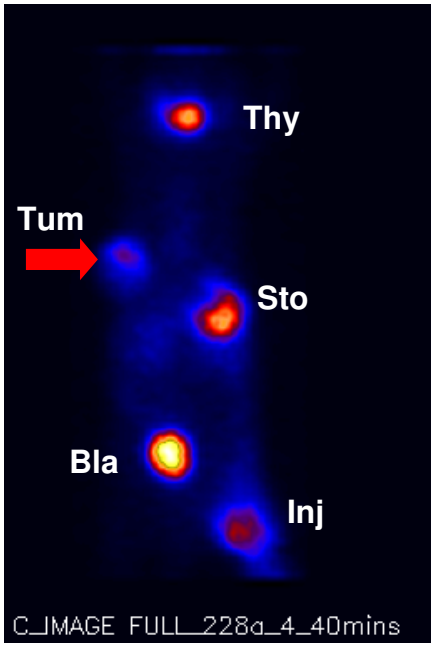

Figure 4.4. Gamma camera imaging of an MMTV animal 4 hours after the administration of iodinated EGF. The signal appears to be specific to the mammary tumor. (Thy = thyroid, Tum = tumor, Bla = bladder, Sto = stomach, Inj = injection site)

APPENDIX

IN VIVO IMAGING OF THE SODIUM IODIDE SYMPORTER ACTIVITY IN THE MOUSE THYROID USING MULTI-PINHOLE HELICAL SPECT

ABSTRACT

In vivo functional imaging of molecular processes in discrete organs is particularly challenging with small animals because non-damaging radiotracer dosage limitations can compromise image resolution and sensitivity. Imaging modalities designed to address this issue while maintaining high image quality have become a primary goal of molecular imaging research. An economical multi-pinhole helical SPECT (mphSPECT) system suitable for imaging the mouse thyroid with radioiodine (^{125}I) was developed requiring both high resolution and low radioactivity for *in vivo* imaging. The characteristic bilobal structure of the thyroid was resolved with minimal radioiodine dosage (7.4 MBq / 200 μCi). Also the expression of the sodium iodide symporter (NIS) was examined in the thyroid gland and validated the efficacy of mphSPECT for molecular targeting. The data suggest potential molecular imaging applications of mphSPECT for a variety of studies on NIS-expressing tissues in mice, such as thyroid, gastrointestinal tract or mammary tumors.

INTRODUCTION

The Sodium Iodide Symporter

The sodium iodide symporter (NIS) is a plasma membrane glycoprotein containing 13 transmembrane domains with extracellular (amino) and intracellular (carboxyl) termini (Levy et al., 1998; Smanik et al., 1997). NIS is responsible for the active transport of an iodide ion against its concentration gradient to be cotransported with two sodium ions generated by the gradient of the sodium/potassium ATPase. Iodide is transported by NIS from the blood into thyroid follicular cells, where it is organified for thyroid hormone synthesis. NIS specific expression in the thyroid gland is regulated by the thyroid stimulating hormone (TSH) secreted by the pituitary gland (Carrasco, 1993).

Other organs that endogenously express NIS and have the capacity to accumulate iodide include the salivary gland, nasolacrimal duct, placenta, gastric mucosa and the lactating mammary gland (Dai et al., 1996; Tazebay et al., 2000). NIS expression in the gastric and salivary gland suggests an avenue for iodide secretion into the gastrointestinal tract for reabsorption into the bloodstream for thyroid use (Josefsson et al., 2002). Mammary gland NIS expression occurs in response to circulating pregnancy hormones and used to supply iodide from the bloodstream to the milk substrate for neonatal thyroid development (Tazebay et al., 2000). Between species cloned NIS of the mouse was found to have 95% homology with that of rat and 81% homology with the human form (Perron et al., 2001).

The Thyroid Gland

The thyroid gland is an endocrine organ located in the cervical region and is responsible for the production of hormones that influence cellular metabolism and maintenance of the basal metabolic rate (Larsen et al., 1998). As needed, thyroid

releasing hormone (TRH) is released from the hypothalamus, stimulating the adenohypophysis of the pituitary gland to secrete thyroid stimulating hormone (TSH) into the bloodstream. TSH acts on thyroid acini or follicular cells to stimulate organification of iodine and secretion of thyroid hormones tri-iodothyronine (T3) and thyroxine (T4) into the bloodstream in order to modulate mitochondrial efficiency. Thyroid hormone precursors are stored in the colloidal region of each thyroid follicle in order to respond rapidly upon physiologic need or dietary depletion of iodine (Larsen et al., 1998).

The thyroid also contains parafollicular, or C, cells that secrete calcitonin hormone responsible for lowering blood calcium levels. Calcitonin specifically inhibits bone resorption by binding to osteoclasts, but may have a role in the central nervous system, testes, and skeletal muscle (reviewed in Elisei (2008)). C cells are oriented either individually or in clusters between thyroid follicles, and are derived from a different embryonic origin than follicular cells (Larsen et al., 1998).

The Mouse Thyroid Gland

Active biosynthesis and secretion of thyroid hormones are predominant in the mouse model. The embryonic mouse thyroid gland initiates iodine accumulation and hormone biosynthesis after 15 days post coitum (dpc) (Fagman et al., 2006; Postiglione et al., 2002), but function is subject to NIS expression (Szinnai et al., 2007). In addition, maximum levels of TSH and thyroid hormones correlate with the maximum iodine uptake between 30-60 days in different mouse lines which decrease with age (Sawitzke et al., 1988). Evidence also suggests a disparity in thyroid function between the sexes whereby females have greater ^{131}I uptake, which varies based on the estrus cycle (Chai, 1970). Environmental factors, metabolic rates and circadian rhythms are also linked to

mouse thyroid hyperactivity which ultimately correlates with decreased lifespans (Buffenstein and Pinto, 2009).

At the molecular level mice have increased thyroid activity compared to humans as well. Recently, differences between human and mouse NIS efficiency of iodide transport have been documented in transfected human embryonic kidney 293 cells. Immunolocalization comparisons between human and mouse NIS found that the mouse counterpart localized predominately to the cell membrane, while approximately two-fifths of cells transfected with human NIS had intracellular protein localization (Dayem et al., 2008). The majority of thyroid follicles in the mouse express NIS (Josefsson et al., 2002), by contrast at any particular time approximately one-fifth of human thyroid follicles express NIS (Faggiano et al., 2007). We have reported that the potassium iodide dosage required for the Wolf-Chaikoff blocking effect is higher in mice than the dose recommended for humans (Hammond et al., 2007).

Imaging the Discrete Lobes of the Mouse Thyroid

In vivo imaging strives to develop tools that follow molecular and physiological processes repeatedly and non-invasively over the lifetime of the organism. The two discrete lobes of the mouse thyroid are particularly challenging for *in vivo* imaging because of its small size and narrow (1-2 mm) lobe separation. Two studies (Hong et al., 2006; McElroy et al., 2002) have shown the capability of single-pinhole SPECT to resolve the bilobal structure of the mouse or rat thyroid using higher ^{125}I doses to the order of 37 MBq (1 mCi). There are reports of the successful resolution of the bilobal structure of the mouse thyroid using planar imaging with small pinholes (100-250 μm)

(Beekman et al., 2002) or coded apertures (Accorsi et al., 2008), which are accomplished with ^{125}I doses of about 10 MBq (270 μCi) to fit the pinhole or aperture dimension.

Radioactive Dose Considerations for Imaging

It is vital that small animal imaging experiments are designed to employ the lowest possible dose of radioactive material whenever medium or long-term *in vivo* studies are undertaken. While the long half-life (59.4 days) of ^{125}I is very useful for metabolic studies, it also raises concerns about excessive radiation exposure that could damage tissues sensitive to radioiodine such as the thyroid. Therefore, employing high radioactivity doses must be carefully considered (Hammond et al., 2007). Several studies have indicated growing concern over high-radiation doses employed in small animal studies (Acton, 2006; Difilippo, 2008; Funk et al., 2004; Kung and Kung, 2005; Liang et al., 2007; Peremans et al., 2005). Reducing the amount of radioactivity used in experiments makes *in vivo*, high-quality molecular imaging of small organs such as the mouse thyroid a challenge.

Multi-pinhole Single Photon Emission Computed Tomography (SPECT)

Multi-pinholed SPECT can be employed to address issues of image quality with reduced radioactivity, while also taking advantage of a large number of readily available ligands tagged with radionuclides such as ^{125}I and ^{99m}Tc (Beekman and van der Have, 2007; Beekman et al., 2005; Goertzen et al., 2005; Hesterman et al., 2007; Jansen and Vanderheyden, 2007; Kim et al., 2006; Meikle et al., 2002; Schramm et al., 2003; Vanhove et al., 2008). Both phantom and animal studies have demonstrated the value of multi-pinhole SPECT for small animal imaging (Forrer et al., 2006; Gotthardt et al.,

2006; Liu et al., 2008; Nuyts et al., 2009; Ostendorf et al., 2006; Pissarek et al., 2008; van der Have et al., 2008).

Hypothesis and Predictions

We have recently designed an economical multi-pinhole helical SPECT system for small animal imaging that is appropriate for a typical biology research laboratory (Qian et al., 2008). Our data, based on phantom studies, suggested multi-pinhole helical SPECT could be utilized to image small animal tissues with high-resolution and good sensitivity. As an *in vivo* proof-of-concept demonstration, multi-pinhole helical SPECT was used to image the living mouse thyroid gland while maintaining a relatively low-level dose of ^{125}I (7.4 MBq / 200 μCi). Herein, we aim to demonstrate the efficacy of our system for molecular targeting by examining the expression of NIS in the mouse thyroid gland. If multi-pinhole helical SPECT is capable of imaging and resolving the discrete lobes of the thyroid with ^{125}I, then we predict that the thyroid image produced will correlate with the expression of NIS protein, which facilitates iodine transport into thyroid cells.

MATERIALS AND METHODS

Multi-pinhole Helical SPECT Imaging System

Design and functional details of this system have been presented in an earlier report which employed only phantoms (Qian et al., 2008). Briefly, a 110 mm diameter circular detector based on a Hamamatsu R3292 position-sensitive photomultiplier tube

(PSPMT) mounted on a cylindrical gantry capable of 360° rotation was employed for gamma-ray imaging. The R3292 module was air-coupled to pixellated NaI(Tl) scintillators measuring 1×1×5 mm^3 separated by 0.2 mm reflective septa. A step-and-shoot helical orbit was effected by incorporating two computer-controlled stepping motors driving the rotation of the gantry around the axis of rotation (AOR) and the translation of the animal bed along the AOR. Each scan obtained projections at 120 angular positions with 3º intervals. A 5 mm thick, multi-pinhole brass collimator suitable for ^{125}I imaging was designed so that each pinhole is 1 mm in diameter with a 0.2 mm channel height and an opening angle of 90°. In the present work, two pinholes were employed by covering unused pinholes with 0.5 mm thick lead foil to block photons emitted from ^{125}I. The radius of rotation was 25 mm from the collimator with a magnifying factor of 3 (focal length: 75 mm) used in the studies. This setup resulted in a field of view with a diameter of ~ 51 mm. Previous measurements showed that a full-width at half maximum (FWHM) resolution of ~ 1.3 mm was achieved using two-pinhole helical SPECT with a sensitivity of 80.6 cps/MBq (Qian et al., 2008).

SPECT projection data in this study were acquired over 360°. Parameters for SPECT scans are variable and thus are stated for each specific case. The image reconstruction approaches were based on the iterative maximum likelihood-expectation maximization (ML-EM) algorithm extended from the method described by Li *et al* (Li et al., 1995) with Siddon's ray tracing technique implemented (Siddon, 1985). The reconstructed images were smoothed with a Hann filter. No attenuation correction was applied in this work. The reconstruction used 0.4-mm cubic voxels. Data collection from imaging was provided by collaborator Dr. Jianguo Qian.

Mouse Model

Two mice from the C57BL/6J strain (Jackson Laboratory, Bar Harbor, Maine) were selected to demonstrate the *in vivo* efficacy of the two-pinhole helical SPECT system. The first mouse was injected with 4.8 MBq (130 μCi) $Na^{125}I$, and imaged 24 hours after the dose was administered. The mouse expired during the third hour of imaging due to an adverse reaction to anesthesia, but imaging continued for four hours. The thyroid was resected at the end of the imaging period, and a direct measurement of the accumulated dose was taken with a Ludlum survey meter fitted with a scintillation probe.

The second mouse was imaged 24 hours after receiving a 7.4 MBq (200 μCi) dose of $Na^{125}I$ for two hours. The mouse was returned to its cage after imaging fully recovered. This study was performed in accordance with protocols approved by the College of William & Mary IACUC animal committee. Anesthesia of animals was performed using sodium pentobarbital (50-90 mg kg^{-1} body mass) injected into the *peritoneal cavity.*

Whole-mount Immunohistochemistry

Whole mount immunohistochemistry was modified from (Johnstone et al., 2000) and used to localize the NIS protein in the thyroid. The thyroid from the first mouse was excised along with the trachea and esophagus to preserve the natural anatomical bilobal structure. The tissue was fixed in 4% paraformaldehyde for 24 hours at 4 $^{\circ}C$. After fixation the tissue was briefly rinsed with phosphate buffered saline (PBS) and permeabilized with PBT (PBS + Triton X-100). Non-specific binding was blocked with

2% bovine serum albumin (BSA) in PBT for 6 hours. The whole thyroid was incubated with rabbit anti-rat NIS primary antibody (Alpha Diagnostic Int., San Antonio, Texas) for 60 hours at 4 °C, and then rinsed with 2% BSA in PBT. Finally, the thyroid tissue was incubated overnight at 4 °C with fluorescent-labeled goat anti-rabbit Alexa-488 secondary antibody (Invitrogen, Eugene, Oregon), and then rinsed in PBT. Bright field and fluorescent photographs (using a fluorescein filter) were taken with an Olympus MagnaFire DP71 camera and an overlay image was created using Adobe Photoshop 7.0.

Sectioning and Histology

Following whole-mount immunohistochemistry preparation the light sensitive thyroid was infiltrated with 1.6 M sucrose/PBS and incubated at 4°C overnight. The thyroid was then infiltrated with 50/50 solution of sucrose and O.C.T. freezing media (Triangle Biomedical Sciences Inc, Durham, NC) for four hours followed by two-hour incubation in O.C.T. media. The gland was transferred to a boat with fresh freezing media and placed on the freeze plate of the Minotome Plus (Triangle Biomedical Sciences Inc, Durham, NC) cryostat machine at -40°C until the freezing media solidified. The frozen tissue block was removed from the boat and mounted to a pin with excess freezing media. The frozen tissue was sectioned inside the Cryostat chamber at -22°C at a thickness of 10 µm.

Tissue slides were rinsed in PBS for five minutes, mounted with nuclear stain Vectorshield with DAPI (Vector Laboratories, Burlingame, CA), and stored at 4°C. Sections were photographed with an Olympus IX50 inverted fluorescent microscope equipped with an Evolution MP digital camera using fluorescein (488 nm). UV filtered

light was used also for DAPI visualization. Composite figures of fluorescent and DAPI images were created using Adobe Photoshop CS3 Extended Version 10.

A subset of thyroid sections were counterstained with hematoxylin and eosin, then subsequently dehydrated in graded alcohol series, cleared and mounted to assess thyroid histology.

RT-PCR

Total RNA was isolated from frozen tissues by RNeasy Midi and Maxi kits (QIAGEN, Valencia, CA). Ambion (Foster City, CA) DNA-free DNase I treatment was applied to the total RNA prior to cDNA synthesis. One microgram of total RNA was reverse transcribed using a Biorad iScript cDNA synthesis kit (Hercules, CA). Intron-spanning PCR primers for NIS were designed using Primer3 software (http://frodo.wi.mit.edu/) and confirmed to be highly specific for mouse NIS using nucleotide BLAST (http://www.ncbi.nlm.nih.gov/BLAST/). The primer sequences for NIS were the following:

sense 5' GCTCTCATTCATCTATGGCTCAAC 3';

anti-sense, 5' GGTGAAAGCGCCAAGGAGAG 3'.

Beta-actin primers (Perron et al., 2001) were used in a parallel reaction for an internal control. PCR was carried out using taq polymerase (New England Biolabs, Beverly, MA) following the manufacturer's protocol with the cycle parameters: 94°C hot start for 5 min, 40 cycles of denaturation at 94°C for 30 sec, annealing at 64°C for 1 min, and extension at 72°C for 2 min, followed by an extension at 72°C for 7 min. Liver was used as a negative tissue control for NIS mRNA expression. As a negative control for each PCR reaction, reverse transcriptase was replaced with H_2O in the cDNA synthesis

reaction. PCR products were separated on a 1.2% agarose gel and stained with ethidium bromide. Gels were visualized under UV light with a Biorad gel documentation system using Quantity One Software. Data for rt-PCR was provided by collaborator Stephen Schworer.

Data Analysis and Statistics

Images of the mouse thyroid from immunohistochemistry and mphSPECT imaging were converted to 32-bit grayscale and pixel intensity and luminescence was quantified using ImageJ 1.40g. The thyroid immunohistochemical image was resized to the scale of the mphSPECT image for analysis. Statistical analysis consisted of Student's t-test and was performed using Statistical Package for the Social Sciences (SPSS) software. Pixel intensity was compared between the left and right lobes of the thyroid.

RESULTS

Animal studies using *in vivo* multi-pinhole helical SPECT can resolve the two lobes of the mouse thyroid

Anatomically, the approximate separation between the two lobes of the C57BL/6J-derived mouse thyroid was between 1.8-2.5 mm, depending upon the position along the margin of the thyroid. Using an overall injection of 4.8 MBq (130 μCi) $Na^{125}I$ this relationship was demonstrated after 24 hours during the first imaging session with a 1.2 mm thick coronal image slice reconstructed from the 4-hour multi-pinhole helical SPECT scan (Fig. 1a). Direct measurement of the resected thyroid with a scintillation probe survey meter indicated that the radioactivity absorbed by the thyroid was about

0.37 MBq (10 μCi). From this measurement the final percent of the injected dose remaining in the thyroid gland was 7.7 %.

The second mouse was injected with 7.4 MBq (200 μCi) $Na^{125}I$ and imaged *in vivo* after 24 hours as well. The subtle bilobal structure of the thyroid was delineated with a 1-min multi-pinhole projection of the thyroid region. Fully covering the whole thyroid region of the mouse, the 4.8 mm thick coronal image from the same multi-pinhole helical SPECT scan correctly indicated the shape and separation of the lobes (Fig. 1b). Using region of interest (ROI) covering the thyroid indirectly measured the radioactivity to be approximately 0.7 MBq (18.9 μCi), which accounted for approximately 9.5% of the injected dose. The *in vivo* animal studies demonstrate that two-pinhole helical SPECT successfully resolved the fine structure of the mouse thyroid within two hours (summary in Table 4.1).

Multi-pinhole helical SPECT can detect the functional activity of the sodium iodide symporter

In order to validate whether mphSPECT imaging correlates with the molecular activity of the sodium iodide symporter ion channel, the macro protein expression of NIS was assessed in the thyroid of the first mouse via immunohistochemistry (Fig. 1c-e). NIS localization was indirectly detected with a fluorescent secondary antibody in the two lobular regions of the thyroid (Fig. 1d). The lobular regions of the thyroid were subsequently cryosectioned to further substantiate that whole-mount NIS localization was specific at the cellular level in the thyroid follicles (Fig. 1f-h). NIS was indeed shown to

be expressed in the thyroid follicular cells which are the site of iodide uptake for hormone biosynthesis (Fig. 1e). As expected, total RNA extracted from C57BL/6J thyroid tissue showed the expression of NIS mRNA for translation into functional protein (Fig. 1i).

Semi-quantitative measures of pixel intensity were analyzed for both the mphSPECT and the whole-mount immunohistochemical images for the first mouse. The images were converted to gray scale and the immunohistochemical image was scaled down to the size of the mphSPECT image. Based on ROI data of the whole thyroid both images followed the same trend of increased pixel intensity in the lobular regions (Fig. 2a). The three-dimensional pixel luminescence of both image types further delineated increased pixel intensity in the two lobes. Although the mphSPECT three-dimensional image appears uniform in luminescence intensity, the immunohistochemical three-dimensional image represents a more accurate luminescence scale because the peaks within the lobular regions become fused in the mphSPECT image (Fig. 2b). In order to assess whether there was a significant difference in pixel intensities between the left and right lobes of the thyroid, ROIs (8 x 40 pixels) were placed on each lobe of both image sources. The data suggest that both mphSPECT ($p<0.05$) and immunohistochemistry ($p<0.01$) images had significantly more pixel intensity in the left lobe of the thyroid compared to the right (Fig. 3). These results strongly demonstrate that multi-pinhole helical SPECT specifically detects the functional activity of NIS protein responsible for ^{125}I uptake in the living mouse thyroid gland.

DISCUSSION

Molecular imaging studies employing SPECT with small animals encounter trade-offs between high spatial resolution with the use of high doses of radio-labeled ligands and limiting the duration of exposure to radioactive materials which may damage tissue and compromise the health of the experimental subject (Funk et al., 2004; Kung and Kung, 2005; Peremans et al., 2005). For example, longitudinal *in vivo* studies suggest excessive iodine accumulation and retention can have significant pathological implications (Hammond et al., 2007) (Ronckers et al., 2006). However, this study demonstrates the application of our economical multi-pinhole helical SPECT that is effective for low-dose, high-quality *in vivo* molecular imaging. We found that 24 hours after administering a low dose of $Na^{125}I$ (7.4 MBq / 200 μCi) our detector was capable of reconstructing the discrete anatomical structure of the two lobes of the mouse thyroid which are separated by only 1-2 mm. Finally, e*x vivo* expression analysis of the sodium iodide symporter was shown to localize in the resected thyroid lobes in the same locations as the pattern of radioiodine distribution in the multi-pinhole helical SPECT images. Therefore, it appears that multi-pinhole helical SPECT effectively images the activity and location of the sodium iodide symporter, the target of radioiodine imaging in the thyroid gland.

Using two pinholes and a relatively high magnifying factor of three, the projections for the entire bilobal thyroid gland can be completely detected from either pinhole and at each detector position during the entire helical SPECT scan, even as the position of the mouse changes along the axis of rotation. For our study, additional pinholes did not significantly improve sensitivity or image quality since truncation

occurred when three or more pinholes were employed, though others have reported on the success of imaging with more than two pinholes (Ostendorf et al., 2006) (Funk et al., 2006). We anticipate that the design of a new multi-pinhole collimator with a more compact pinhole pattern coupled with an appropriate magnification factor will allow us to apply a greater number of pinholes in the system and thereby facilitate shorter scan time and an even lower injection dose.

Other examples of multi-pinhole helical SPECT systems have been developed (Difilippo, 2008; Lackas et al., 2004) and two commercial small animal imaging systems, the NanoSPECT (Koninklijke Philips Electronics 2009) and U-SPECT-II (MILabs 2008), have multi-pinhole and helical SPECT capability. A prior *in vivo* ^{125}I SPECT study was reported by McElroy *et al* (McElroy et al., 2002) using single-pinhole SPECT and an injected dose of 37 MBq (1 mCi) ^{125}I with a 16 min. imaging period. Compared to that study, our *in vivo* two-pinhole helical SPECT study has a lower dose and longer imaging time (2 hours). The longer imaging time in our study results from an approximately 1.8 reduction in sensitivity of our two-pinhole gamma camera compared with the LumaGEM detector used in the McElroy *et al* study (McElroy et al., 2002). Additionally, the McElroy team imaged the mouse 7.5 hours post injection, while we imaged a full 24 hours post injection. Longer times between injection and imaging are important for metabolic and functional studies of the thyroid (Meikle et al., 2005); though Ferreira *et al* (Ferreira et al., 2005) have suggested radioiodine content measured after 15 min. of administration can efficiently evaluate basolateral iodide transport. Taken together, our two-pinhole helical SPECT system achieved excellent image quality along with significant dose reduction.

Multi-pinhole helical SPECT has numerous biomedical applications with the thyroid. NIS expression is the driving force behind radioiodide treatment for thyroid cancer with targeted radioiodide uptake destruction of metastatic cells after thyroidectomy (Carrasco, 1993). Radioiodine imaging targeting NIS can be utilized for imaging the metabolic differences between hyper- and hypothyroidism (Chung, 2002; Dadachova and Carrasco, 2004). Likewise, our imaging system would be beneficial for imaging genetically engineered mouse models in order to characterize thyroid cancer (reviewed in Knostman et al. (2007a)). As NIS is generally under expressed in thyroid cancer, different methods for increasing its expression for radioiodine therapy could be evaluated using our system, along with imaging metastatic tumors post-treatment (Aide et al., 2009; Schipper et al., 2007; Spanu et al., 2009). The work presented here suggests the potential of employing multi-pinhole helical SPECT with other tissues expressing the sodium iodide symporter such as gastric and breast cancer studies (Dadachova and Carrasco, 2004; Dohan and Carrasco, 2003; Perron et al., 2001).

Table 1. Summary of imaging information for mice analyzed with mphSPECT.

Mouse	$Na^{125}I$ Dose	Image Lapse	Image Duration	%ID in Thyroid
1	130 μCi	24 hours	4 hours	7.7 % ID
2	200 μCi	24 hours	2 hours	9.5 % ID

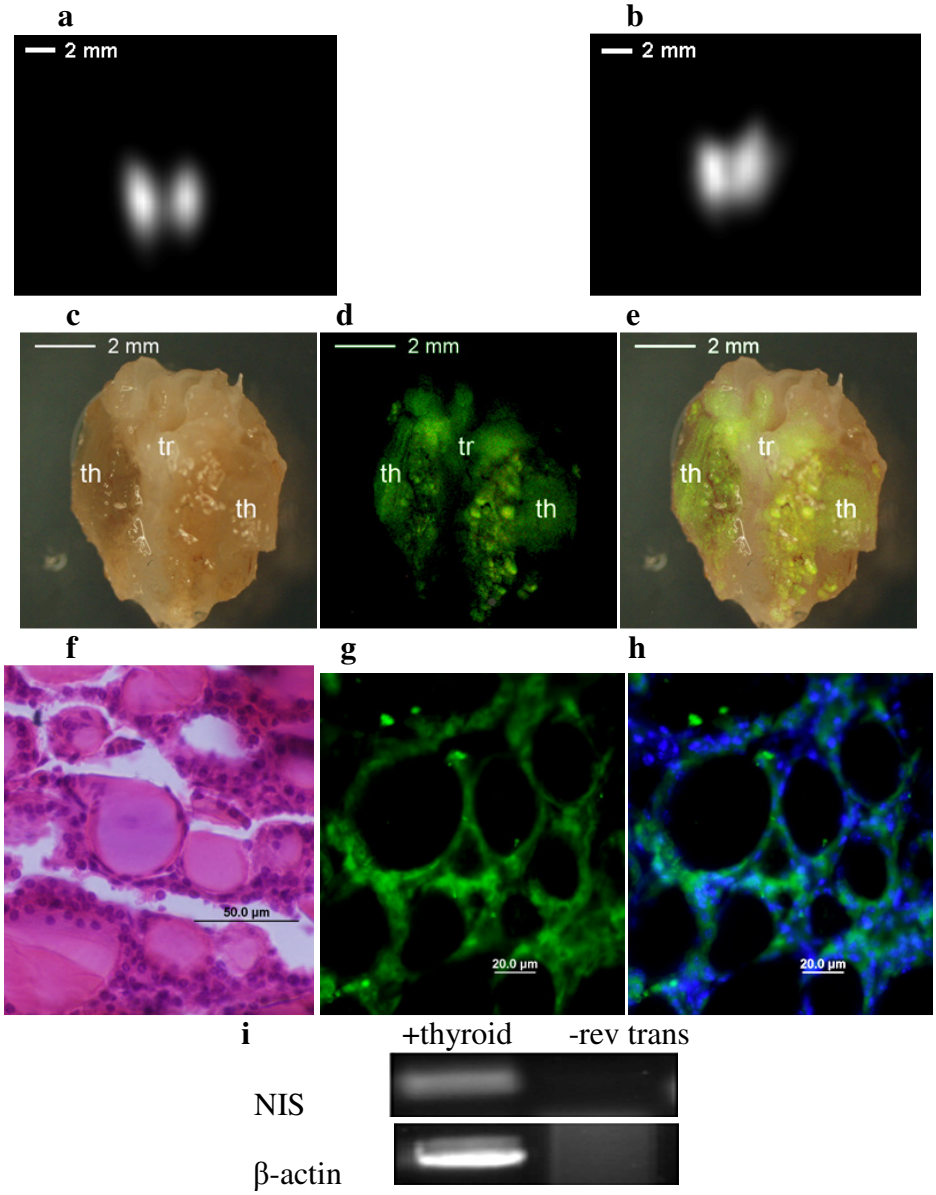

Figure 1. (a) A reconstructed coronal image from the 4 hour multi-pinhole projection image with the central pinhole near the thyroid region of the first mouse. (b) A reconstructed coronal image from the 2 hour multi-pinhole projection image with the central pinhole near the thyroid region of the second mouse. (c) Anatomy of the resected first mouse thyroid showing the lobes flanking the trachea. (d) Whole-mount immunolocalization of NIS protein (green signal) with anti-NIS primary antibody. (e) Overlay of (c) and (d) localizing NIS protein in the lobes of the thyroid. (f) Mouse thyroid histology (40x) identifying the circular follicles where NIS is expressed. (g) High power (40x) localization of NIS in mouse thyroid follicles from whole-mount tissue sections (c). (h) Overlay of (g) with DAPI counterstaining of follicular cell nuclei. (i) Total RNA extracted from mouse thyroid expresses NIS mRNA for functional protein translation. (th = thyroid, tr = trachea)

a

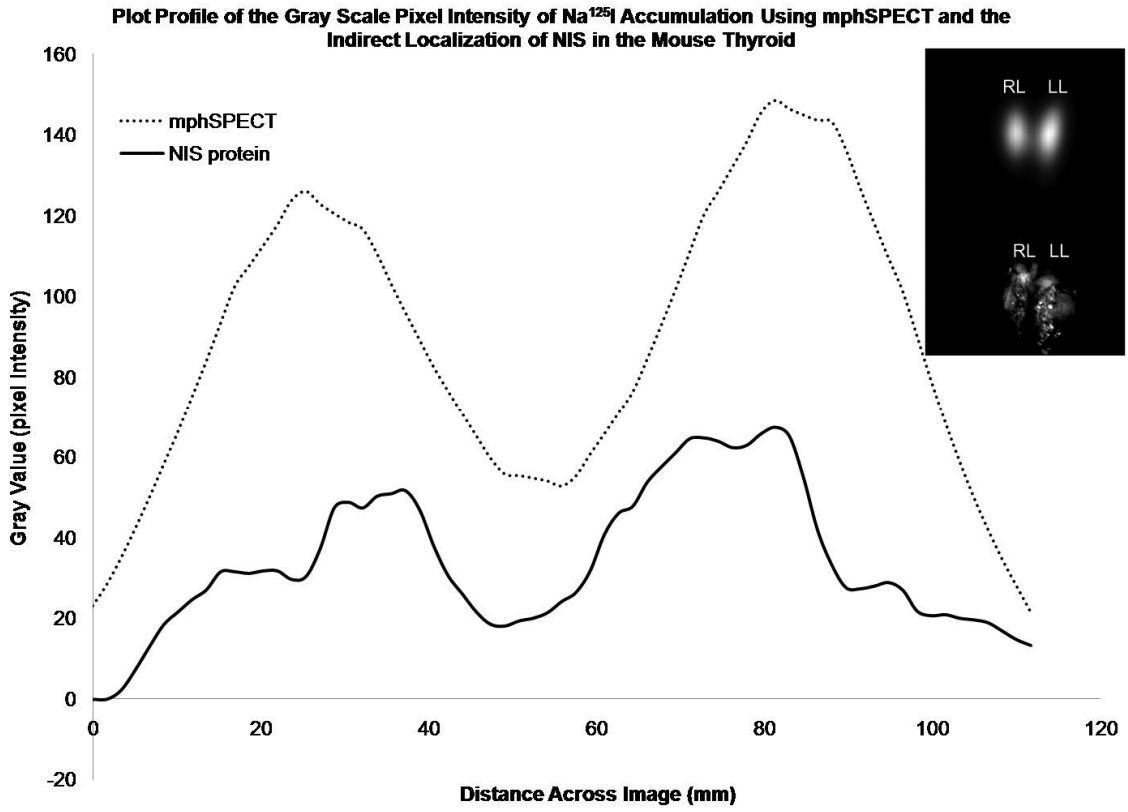

b

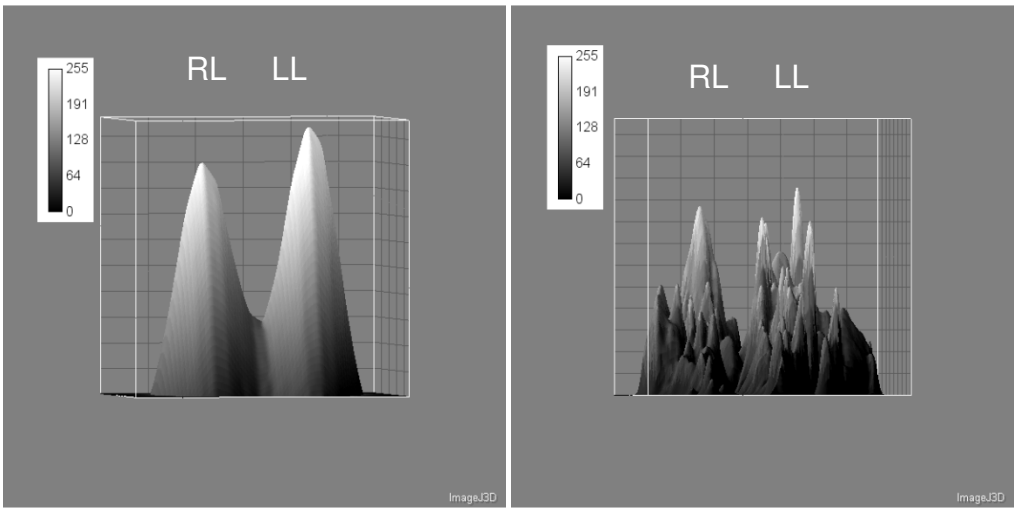

Figure 2. (a) Plot profiles of mphSPECT (dotted line) and NIS localization (solid line) images of the thyroid exhibit similar trends of pixel intensities (inset gray scale mphSPECT (top), NIS localization (bottom). (b) Gray scale three dimensional pixel luminescence profiles of mphSPECT (left) and NIS localization (right) images further indicate that the imaging modality and NIS activity are coincident in the mouse thyroid (inset luminescence scale). (RL = right lobe, LL = left lobe)

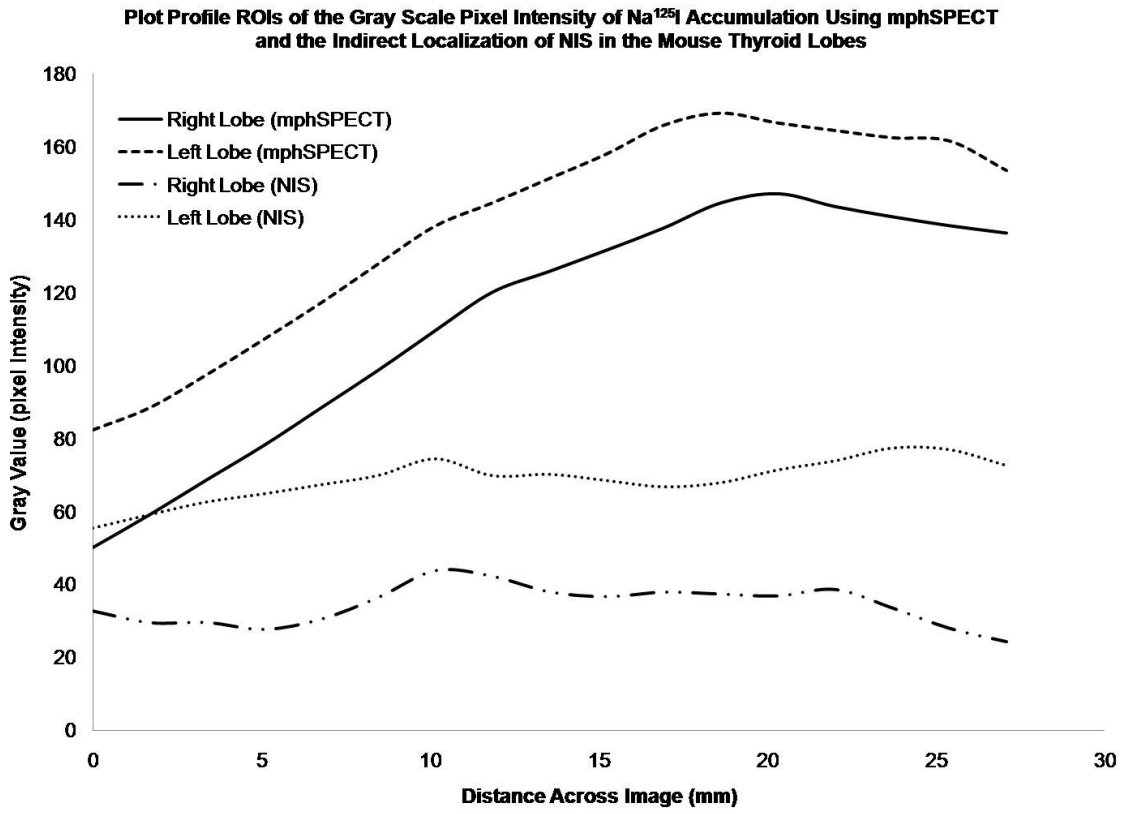

Figure 3. ROI analysis of the individual mouse thyroid lobes suggests a significant difference in gray scale pixel intensity between the two lobes in both $Na^{125}I$ uptake and NIS protein localization. ROIs (8 x 40 pixels) placed on each individual lobe of the thyroid whether using mphSPECT ($p < 0.05$) or NIS protein localization ($p < 0.01$) are significantly different in the gray scale pixel intensity. The data indicate that the left lobe of the C57 mouse accumulated more $Na^{125}I$ which can be attributed to increase in the amount of functional NIS protein.

DUAL MODALITY APPLICATION OF THE GAMMA CAMERA

Earlier our team developed a versatile apparatus capable of dual modality planar imaging with a first-generation gamma camera (described in (Weisenberger et al., 1998)) coupled with a Lixi fluoroscopic X-ray (Saha et al., 2003). This device was capable of monitoring radioiodine uptake in sensitive tissues, as well as providing anatomical information. We are currently working to expand dual modality imaging to include other modalities that can target molecular markers and events in tumorigenesis.

Currently, angiogenesis detection has become an area of active research for *in vivo* imaging application (Ahmadi et al., 2008; Almutairi et al., 2009; Lijowski et al., 2009). The premise being that for a tumor to proliferate and eventually metastasize there must be adequate blood supply. In particular, $\alpha v\beta 3$ integrins have been shown to be involved with angiogenesis in both normal and tumor tissue, and these behave as receptors for different ligands expressing arginine-glycine-aspartic acid (RGD) (Schottelius et al., 2009). Many have studied *in vivo* dual modality imaging of angiogenesis in relation to vascular endothelial growth factor receptor (VEGFR) using PET, SPECT, and optical imaging (reviewed in Cai and Chen (2008)).

In our preliminary *in vivo* study an economical SBIG-ST6 cooled CCD camera (Santa Barbara Instrument Group) has been used to image RGD-linked quantum dots (Q-dots) (Invitrogen, Eugene, OR) that target angiogenesis. These Q-dots emit photons at an 800 nm wavelength that can be detected when excited by blue light-emitting diodes (LEDs). In our preliminary work, Q-dot detection was combined with gamma camera

functional imaging of the sodium iodide symporter in MMTV tumor bearing mice (Fig. 4).

These initial results have suggested that in the MMTV model very little angiogenesis has taken place in a developed tumor compared to the inguinal mammary glands that did not show evidence of primary tumor. In comparison, the sodium iodide symporter activity was most pronounced in the primary tumor, but was also detected at lower levels in the non-involved mammary glands (Fig. 5). While the results appeared to be promising, more experimental work and analysis must be completed.

The natural beginning point would be to target VEGFR expression with the gamma camera while comparing the radioisotope uptake with Q-dot signal in order to validate whether both signals are coincident. For example, Fig. 5 (I-M) displays the unique distribution patterns of ^{125}I (Fig. 5I), RGD-Q-dot ($\alpha v\beta 3$ integrins, Fig. 5J), and sodium iodide symporter protein (fluorescent antibody signal, Fig. 5K) in the putative normal mammary gland of a MMTV tumor bearing mouse. As expected, the ^{125}I signal and protein expression correlate almost perfectly (Fig. 5M), but the RGD-Q-dot signal is not (Fig. 5L). These data validate that ^{125}I and RGD-Q-dots are sensitive molecular tracers that can be resolved with our imaging modalities. Therefore, it would be valuable to image the VEGFR coupled with RGD-Q-dots to observe whether the two angiogenesis markers have similar molecular targeting specificity.

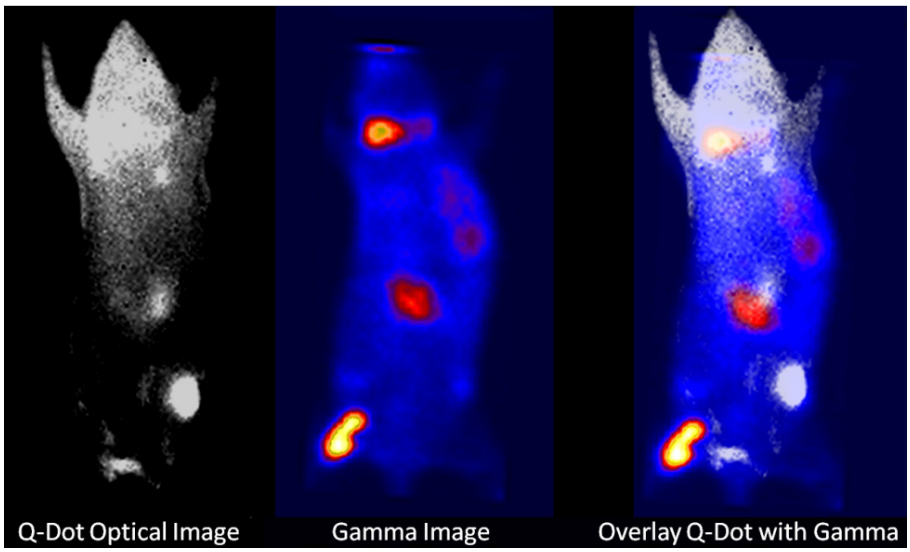

Figure 4. *In vivo* dual modality imaging of an MMTV mouse with a left thoracic primary tumor. Q-dot imaging (left panel) 12 hours after administration showed strong uptake in the right inguinal gland compared to the tumor area. Gamma camera imaging (center panel) showed ^{125}I accumulation not only in the primary tumor, but also in both inguinal glands. An overlay image of both modalities (right panel).

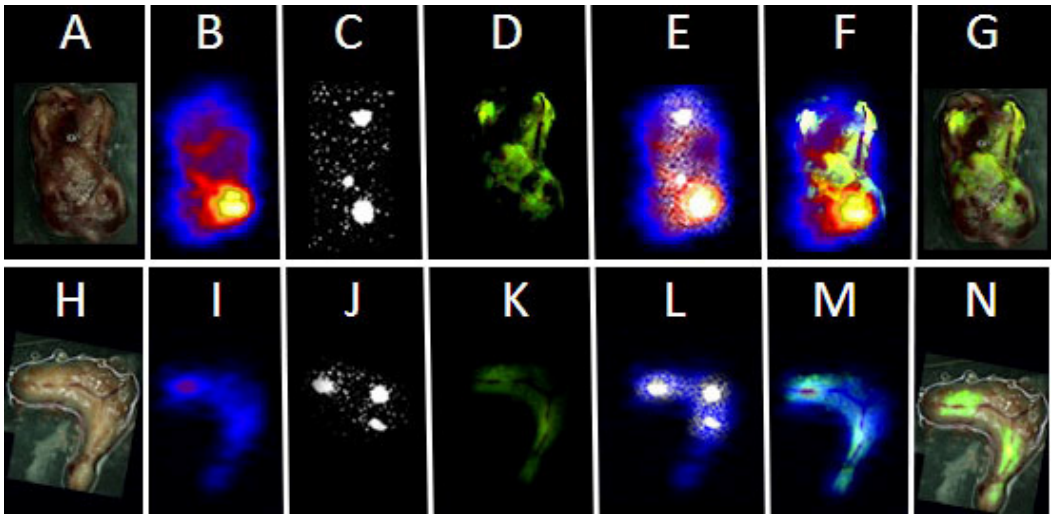

Figure 5. *Ex vivo* dual modality imaging analysis of a left thoracic and left inguinal mammary gland. (A and H) Whole mount image in bright field. (B and I) 5 minute gamma image. (C and J) 60 second Q-dot optical image. (D and K) Whole mount immunohistochemistry against NIS where the green signal represents NIS protein. (E and L) Composite of the gamma image with the Q-dot image. (F and M) Composite of the gamma image with NIS immunolocalization. (G and N) Composite of the bright field and NIS immunolocalization.

REFERENCES

Abbey, C. K., et al., 2006. Preclinical imaging of mammary intraepithelial neoplasia with positron emission tomography. J Mammary Gland Biol Neoplasia. 11**,** 137-49.

Accorsi, R., et al., 2008. High-Resolution 125I Small Animal Imaging With a Coded Aperture and a Hybrid Pixel Detector. IEEE Transactions on Nuclear Science. 55**,** 481-490.

Acha-Orbea, H., MacDonald, H. R., 1995. Superantigens of mouse mammary tumor virus. Annu Rev Immunol. 13**,** 459-86.

Acton, P. D., 2006. Animal Imaging Equipment: Recent Advances. Journal of Nuclear Medicine. 47**,** 52N-55N.

Ahmadi, M., et al., 2008. Chemical and Biological Evaluations of an (111) In-Labeled RGD-Peptide Targeting Integrin Alpha(V) Beta(3) in a Preclinical Tumor Model. Cancer Biother Radiopharm.

Aide, N., et al., 2009. Clinical relevance of SPECT-CT of the neck and thorax in post-ablation 131I scintigraphy for thyroid cancer. J Clin Endocrinol Metab.

Aliaga, A., et al., 2007. A small animal positron emission tomography study of the effect of chemotherapy and hormonal therapy on the uptake of 2-deoxy-2-[F-18]fluoro-D-glucose in murine models of breast cancer. Mol Imaging Biol. 9**,** 144-50.

Almubarak, M., et al., 2009. Role of positron-emission tomography scan in the diagnosis and management of breast cancer. Oncology (Williston Park). 23**,** 255-61.

Almutairi, A., et al., 2009. Biodegradable dendritic positron-emitting nanoprobes for the noninvasive imaging of angiogenesis. Proc Natl Acad Sci U S A. 106**,** 685-90.

Alotaibi, H., et al., 2006. Unliganded estrogen receptor-alpha activates transcription of the mammary gland Na+/I- symporter gene. Biochem Biophys Res Commun. 345**,** 1487-96.

Azizi, F., Smyth, P., 2009. Breastfeeding and maternal and infant iodine nutrition. Clin Endocrinol (Oxf). 70**,** 803-9.

Ballinger, J. R., 2008. Re: Planar and SPECT imaging in the era of PET and PET-CT: can it survive the test of time? Eur J Nucl Med Mol Imaging. 35**,** 2340.

Baranwal, S., Alahari, S. K., 2009. Molecular mechanisms controlling E-cadherin expression in breast cancer. Biochem Biophys Res Commun. 384**,** 6-11.

Bartella, L., et al., 2007. Imaging breast cancer. Radiol Clin North Am. 45**,** 45-67.

Basu, S., et al., 2008. Comparison of triple-negative and estrogen receptor-positive/progesterone receptor-positive/HER2-negative breast carcinoma using quantitative fluorine-18 fluorodeoxyglucose/positron emission tomography imaging parameters: a potentially useful method for disease characterization. Cancer. 112**,** 995-1000.

Beekman, F., van der Have, F., 2007. The pinhole: gateway to ultra-high-resolution three-dimensional radionuclide imaging. Eur J Nucl Med Mol Imaging. 34**,** 151-61.

Beekman, F. J., et al., 2002. Towards in vivo nuclear microscopy: iodine-125 imaging in mice using micro-pinholes. Eur J Nucl Med Mol Imaging. 29**,** 933-8.

Beekman, F. J., et al., 2005. U-SPECT-I: a novel system for submillimeter-resolution tomography with radiolabeled molecules in mice. J Nucl Med. 46**,** 1194-200.

Benard, F., Turcotte, E., 2005. Imaging in breast cancer: Single-photon computed tomography and positron-emission tomography. Breast Cancer Res. 7**,** 153-62.

Beutner, U., et al., 1994. B cells are essential for murine mammary tumor virus transmission, but not for presentation of endogenous superantigens. J Exp Med. 179**,** 1457-66.

Beyer, S. J., et al., 2008. Do cell surface trafficking impairments account for variable cell surface sodium iodide symporter levels in breast cancer? Breast Cancer Res Treat.

Blackwood, K. J., et al., 2009. In Vivo SPECT Quantification of Transplanted Cell Survival After Engraftment Using 111In-Tropolone in Infarcted Canine Myocardium. J Nucl Med. 50**,** 927-935.

Bocchinfuso, W. P., et al., 1999. A mouse mammary tumor virus-Wnt-1 transgene induces mammary gland hyperplasia and tumorigenesis in mice lacking estrogen receptor-alpha. Cancer Res. 59**,** 1869-76.

Boelaert, K., et al., 2007. PTTG and PBF repress the human sodium iodide symporter. Oncogene. 26**,** 4344-56.

Bouchalova, K., et al., 2009. Triple negative breast cancer--current status and prospective targeted treatment based on HER1 (EGFR), TOP2A and C-MYC gene assessment. Biomed Pap Med Fac Univ Palacky Olomouc Czech Repub. 153**,** 13-7.

Boyd, N. F., et al., 2009. Mammographic density: a heritable risk factor for breast cancer. Methods Mol Biol. 472**,** 343-60.

Bradley, E. L., et al., 2006. A compact gamma camera for biological imaging. IEEE Transactions on Nuclear Science. 53**,** 59-65.

Bradlow, H. L., et al., 1985. Estradiol 16 alpha-hydroxylation in the mouse correlates with mammary tumor incidence and presence of murine mammary tumor virus: a possible model for the hormonal etiology of breast cancer in humans. Proc Natl Acad Sci U S A. 82**,** 6295-9.

Brem, R. F., et al., 2008. Breast-specific gamma imaging as an adjunct imaging modality for the diagnosis of breast cancer. Radiology. 247**,** 651-7.

Brem, R. F., et al., 2007. Breast-specific gamma imaging with 99mTc-Sestamibi and magnetic resonance imaging in the diagnosis of breast cancer--a comparative study. Breast J. 13**,** 465-9.

Buck, A., et al., 2002. FDG uptake in breast cancer: correlation with biological and clinical prognostic parameters. Eur J Nucl Med Mol Imaging. 29**,** 1317-23.

Buffenstein, R., Pinto, M., 2009. Endocrine function in naturally long-living small mammals. Mol Cell Endocrinol. 299**,** 101-11.

Butt, A. J., et al., 2008. Cell cycle machinery: links with genesis and treatment of breast cancer. Adv Exp Med Biol. 630**,** 189-205.

Cai, W., Chen, X., 2008. Multimodality molecular imaging of tumor angiogenesis. J Nucl Med. 49 Suppl 2**,** 113S-28S.

Callahan, R., Smith, G. H., 2000. MMTV-induced mammary tumorigenesis: gene discovery, progression to malignancy and cellular pathways. Oncogene. 19**,** 992-1001.

Callahan, R., Smith, G. H., 2008. Common Integration Sites for MMTV in Viral Induced Mouse Mammary Tumors. J Mammary Gland Biol Neoplasia.

Cardiff, R. D., et al., 2000a. The mammary pathology of genetically engineered mice: the consensus report and recommendations from the Annapolis meeting. Oncogene. 19**,** 968-88.

Cardiff, R. D., Kenney, N., 2007. Mouse mammary tumor biology: a short history. Adv Cancer Res. 98**,** 53-116.

Cardiff, R. D., et al., 2000b. Genetically engineered mouse models of mammary intraepithelial neoplasia. J Mammary Gland Biol Neoplasia. 5**,** 421-37.

Cardiff, R. D., Wellings, S. R., 1999. The comparative pathology of human and mouse mammary glands. J Mammary Gland Biol Neoplasia. 4**,** 105-22.

Carrasco, N., 1993. Iodide transport in the thyroid gland. Biochim Biophys Acta. 1154**,** 65-82.

Cetin, I., et al., 2008. Infertility as a cancer risk factor - a review. Placenta. 29 Suppl B**,** 169-77.

Chai, C. K., 1970. Selective breeding for thyroid 131I uptake in mice. Genetics. 64**,** 29-40.

Chen, J. H., et al., 2008. Estrogen receptor and breast MR imaging features: A correlation study. J Magn Reson Imaging. 27**,** 825-33.

Chen, X., et al., 2004. MicroPET imaging of breast cancer alphav-integrin expression with 64Cu-labeled dimeric RGD peptides. Mol Imaging Biol. 6**,** 350-9.

Cho, J. Y., et al., 2000. Hormonal regulation of radioiodide uptake activity and Na+/I- symporter expression in mammary glands. J Clin Endocrinol Metab. 85**,** 2936-43.

Chung, J. K., 2002. Sodium iodide symporter: its role in nuclear medicine. J Nucl Med. 43**,** 1188-200.

Cleary, M. P., Grossmann, M. E., 2009. Minireview: Obesity and breast cancer: the estrogen connection. Endocrinology. 150**,** 2537-42.

Collingridge, D. R., et al., 2002. The development of [(124)I]iodinated-VG76e: a novel tracer for imaging vascular endothelial growth factor in vivo using positron emission tomography. Cancer Res. 62**,** 5912-9.

Crivellari, D., et al., 2007. Breast cancer in the elderly. J Clin Oncol. 25**,** 1882-90.

Cui, J., et al., 2009. A new automated method for the segmentation and characterization of breast masses on ultrasound images. Medical Physics. 36**,** 1553-1565.

Culver, J., et al., 2008. Multimodality molecular imaging with combined optical and SPECT/PET modalities. J Nucl Med. 49**,** 169-72.

Cwikla, J. B., et al., 1999. Correlation between uptake of Tc-99m sestaMIBI and prognostic factors of breast cancer. Anticancer Res. 19**,** 2299-304.

Dadachova, E., Carrasco, N., 2004. The Na/I symporter (NIS): imaging and therapeutic applications. Semin Nucl Med. 34**,** 23-31.

Dadachova, E., et al., 2005. Treatment with rhenium-188-perrhenate and iodine-131 of NIS-expressing mammary cancer in a mouse model remarkably inhibited tumor growth. Nucl Med Biol. 32**,** 695-700.

Dai, G., et al., 1996. Cloning and characterization of the thyroid iodide transporter. Nature. 379**,** 458-60.

Dayem, M., et al., 2008. Comparison of expressed human and mouse sodium/iodide symporters reveals differences in transport properties and subcellular localization. J Endocrinol. 197**,** 95-109.

Dehdashti, F., et al., 2009. PET-based estradiol challenge as a predictive biomarker of response to endocrine therapy in women with estrogen-receptor-positive breast cancer. Breast Cancer Res Treat. 113**,** 509-17.

Difilippo, F. P., 2008. Design and performance of a multi-pinhole collimation device for small animal imaging with clinical SPECT and SPECT-CT scanners. Phys Med Biol. 53**,** 4185-201.

Dijkers, E. C., et al., 2009. Development and Characterization of Clinical-Grade 89Zr-Trastuzumab for HER2/neu ImmunoPET Imaging. J Nucl Med. 50**,** 974-981.

Dohan, O., Carrasco, N., 2003. Advances in Na(+)/I(-) symporter (NIS) research in the thyroid and beyond. Mol Cell Endocrinol. 213**,** 59-70.

Dohan, O., et al., 2006. Hydrocortisone and purinergic signaling stimulate sodium/iodide symporter (NIS)-mediated iodide transport in breast cancer cells. Mol Endocrinol. 20**,** 1121-37.

Dohan, O., et al., 2003. The sodium/iodide Symporter (NIS): characterization, regulation, and medical significance. Endocr Rev. 24**,** 48-77.

Drever, L. A., et al., 2007. Comparison of three image segmentation techniques for target volume delineation in positron emission tomography. J Appl Clin Med Phys. 8**,** 93-109.

Elisei, R., 2008. Routine serum calcitonin measurement in the evaluation of thyroid nodules. Best Pract Res Clin Endocrinol Metab. 22**,** 941-53.

Faggiano, A., et al., 2007. Functional characterization of human thyroid tissue with immunohistochemistry. Thyroid. 17**,** 203-11.

Fagman, H., et al., 2006. The developing mouse thyroid: embryonic vessel contacts and parenchymal growth pattern during specification, budding, migration, and lobulation. Dev Dyn. 235**,** 444-55.

Fan, W., et al., 2004. [Experimental study of bio-distribution and tumor imaging of 131I in nude mice bearing human breast cancer]. Ai Zheng. 23**,** 808-11.

Fenchel, S., et al., 2002. Asymptomatic adnexal masses: correlation of FDG PET and histopathologic findings. Radiology. 223**,** 780-8.

Fernandes, C., et al., 2007. Radioiodination of new EGFR inhibitors as potential SPECT agents for molecular imaging of breast cancer. Bioorg Med Chem. 15**,** 3974-80.

Ferreira, A. C., et al., 2005. Rapid regulation of thyroid sodium-iodide symporter activity by thyrotrophin and iodine. J Endocrinol. 184**,** 69-76.

Ferretti, E., et al., 2008. Notch signaling is involved in expression of thyrocyte differentiation markers and is downregulated in thyroid tumors. J Clin Endocrinol Metab.

Fonsatti, E., et al., 2000. Endoglin is a suitable target for efficient imaging of solid tumors: in vivo evidence in a canine mammary carcinoma model. Clin Cancer Res. 6**,** 2037-43.

Forrer, F., et al., 2006. In vivo radionuclide uptake quantification using a multi-pinhole SPECT system to predict renal function in small animals. Eur J Nucl Med Mol Imaging. 33**,** 1214-7.

Freund, R., et al., 1992. Polyoma tumorigenesis in mice: evidence for dominant resistance and dominant susceptibility genes of the host. Virology. 191**,** 724-31.

Funk, T., et al., 2006. A multipinhole small animal SPECT system with submillimeter spatial resolution. Med Phys. 33**,** 1259-68.

Funk, T., et al., 2004. Radiation dose estimate in small animal SPECT and PET. Med Phys. 31**,** 2680-6.

Fuster, D., et al., 2002. Quantified 99mTc-MIBI scintigraphy for predicting chemotherapy response in breast cancer patients: factors that influence the level of 99m Tc-MIBI uptake. Nucl Med Commun. 23**,** 31-8.

Gabrielson, K., et al., In Vivo Imaging Mouse Models of Breast Cancer. In: M. G. Pomper, J. G. Gelovani, Eds.), Molecular Imaging in Oncology. Informa Health Care, New York, NY, 2008, pp. 357-375.

Garrood, T., et al., 2009. A novel model for the pre-clinical imaging of inflamed human synovial vasculature. Rheumatology (Oxford).

Geyer, F. C., et al., 2009. The role of molecular analysis in breast cancer. Pathology. 41**,** 77-88.

Goertzen, A. L., et al., 2005. First results from the high-resolution mouseSPECT annular scintillation camera. IEEE Transactions on Medical Imaging. 24**,** 863-867.

Golovkina, T. V., et al., 1994. Coexpression of exogenous and endogenous mouse mammary tumor virus RNA in vivo results in viral recombination and broadens the virus host range. J Virol. 68**,** 5019-26.

Golovkina, T. V., et al., 1997. Generation of a tumorigenic milk-borne mouse mammary tumor virus by recombination between endogenous and exogenous viruses. J Virol. 71**,** 3895-903.

Golubovskaya, V. M., et al., 2009. FAK overexpression and p53 mutations are highly correlated in human breast cancer. Int J Cancer.

Gommans, G. M., et al., 2007. (99M)Technetium-sestamibi scintimammography in non-palpable breast lesions found on screening X-ray mammography. Eur J Surg Oncol. 33**,** 23-7.

Gotthardt, M., et al., 2006. A new technique for in vivo imaging of specific GLP-1 binding sites: first results in small rodents. Regul Pept. 137**,** 162-7.

Gunzburg, W. H., Salmons, B., 1992. Factors controlling the expression of mouse mammary tumour virus. Biochem J. 283 (Pt 3)**,** 625-32.

Guy, C. T., et al., 1992. Induction of mammary tumors by expression of polyomavirus middle T oncogene: a transgenic mouse model for metastatic disease. Mol Cell Biol. 12**,** 954-61.

Guy, C. T., et al., 1994. Activation of the c-Src tyrosine kinase is required for the induction of mammary tumors in transgenic mice. Genes Dev. 8**,** 23-32.

Ha, M., et al., 2007. Smoking cigarettes before first childbirth and risk of breast cancer. Am J Epidemiol. 166**,** 55-61.

Hammond, W. T., et al., 2007. A gamma camera re-evaluation of potassium iodide blocking efficiency in mice. Health Phys. 92**,** 396-406.

Han, Z. B., et al., 2008. Hypoxia-inducible factor (HIF)-1{alpha} directly enhances the transcriptional activity of stem cell factor (SCF) in response to hypoxia and epidermal growth factor (EGF). Carcinogenesis.

Hesterman, J. Y., et al., 2007. The multi-module, multi-resolution system (M3R): a novel small-animal SPECT system. Med Phys. 34**,** 987-93.
Hong, K. J., et al., 2006. A Compact SPECT/CT System for Small Animal Imaging. IEEE Transactions on Nuclear Science. 53**,** 2601-2604.
Hook, L. M., et al., 2000. Genetics of mouse mammary tumor virus-induced mammary tumors: linkage of tumor induction to the gag gene. J Virol. 74**,** 8876-83.
Hruska, C. B., O'Connor, M. K., 2008. Quantification of lesion size, depth, and uptake using a dual-head molecular breast imaging system. Med Phys. 35**,** 1365-76.
Hsueh, W. A., et al., 2006. Predicting chemotherapy response to paclitaxel with 18F-Fluoropaclitaxel and PET. J Nucl Med. 47**,** 1995-9.
Hung, B. T., et al., 2009. Appropriate time for post-therapeutic I-131 whole body scan. Clin Nucl Med. 34**,** 339-42.
Jansen, F. P., Vanderheyden, J. L., 2007. The future of SPECT in a time of PET. Nucl Med Biol. 34**,** 733-5.
Jemal, A., et al., 2009. Cancer Statistics, 2009. CA Cancer J Clin.
Jin, W., et al., 2008. c-Src is required for tropomyosin receptor kinase C (TrkC)-induced activation of the phosphatidylinositol 3-kinase (PI3K)-AKT pathway. J Biol Chem. 283**,** 1391-400.
Johnstone, C. N., et al., 2000. Characterization of mouse A33 antigen, a definitive marker for basolateral surfaces of intestinal epithelial cells. Am J Physiol Gastrointest Liver Physiol. 279**,** G500-10.
Josefsson, M., et al., 2002. Sodium/iodide-symporter: distribution in different mammals and role in entero-thyroid circulation of iodide. Acta Physiol Scand. 175**,** 129-37.
Kenney, N. J., et al., 1996. Detection of amphiregulin and Cripto-1 in mammary tumors from transgenic mice. Mol Carcinog. 15**,** 44-56.
Kesner, A. L., et al., 2007. Biodistribution and predictive value of 18F-fluorocyclophosphamide in mice bearing human breast cancer xenografts. J Nucl Med. 48**,** 2021-7.
Kim, H., et al., 2007a. High-resolution single-photon emission computed tomography and X-ray computed tomography imaging of Tc-99m-labeled anti-DR5 antibody in breast tumor xenografts. Mol Cancer Ther. 6**,** 866-75.
Kim, H., et al., 2006. SemiSPECT: a small-animal single-photon emission computed tomography (SPECT) imager based on eight cadmium zinc telluride (CZT) detector arrays. Med Phys. 33**,** 465-74.
Kim, W. B., et al., 2007b. Overexpression of Wnt-1 in thyrocytes enhances cellular growth but suppresses transcription of the thyroperoxidase gene via different signaling mechanisms. J Endocrinol. 193**,** 93-106.
Knostman, K. A., et al., 2004. Signaling through 3',5'-cyclic adenosine monophosphate and phosphoinositide-3 kinase induces sodium/iodide symporter expression in breast cancer. J Clin Endocrinol Metab. 89**,** 5196-203.
Knostman, K. A., et al., 2007a. Genetic alterations in thyroid cancer: the role of mouse models. Vet Pathol. 44**,** 1-14.
Knostman, K. A., et al., 2007b. PI3K activation is associated with intracellular sodium/iodide symporter protein expression in breast cancer. BMC Cancer. 7**,** 137.

Kogai, T., et al., 2004. Systemic retinoic acid treatment induces sodium/iodide symporter expression and radioiodide uptake in mouse breast cancer models. Cancer Res. 64**,** 415-22.

Kogai, T., et al., 2008. Retinoic acid stimulation of the sodium/iodide symporter in MCF-7 breast cancer cells is mediated by the insulin growth factor-I/phosphatidylinositol 3-kinase and p38 mitogen-activated protein kinase signaling pathways. J Clin Endocrinol Metab. 93**,** 1884-92.

Kordon, E. C., 2008. MMTV-induced pregnancy-dependent mammary tumors : early history and new perspectives. J Mammary Gland Biol Neoplasia. 13**,** 289-97.

Kronblad, A., et al., 2006. Hypoxia inducible factor-1alpha is a prognostic marker in premenopausal patients with intermediate to highly differentiated breast cancer but not a predictive marker for tamoxifen response. Int J Cancer. 118**,** 2609-16.

Kung, M. P., Kung, H. F., 2005. Mass effect of injected dose in small rodent imaging by SPECT and PET. Nucl Med Biol. 32**,** 673-8.

Kurdziel, K. A., et al., 2007. Imaging multidrug resistance with 4-[(18)F]fluoropaclitaxel. Nucl Med Biol. 34**,** 823-31.

Lackas, C., et al., 2004. On the development of a high-resolution multi-pinhole SPECT/CT. 2004 IEEE Nuclear Science Symposium Conference Record. 6**,** 3893-3895.

Lamarca, H. L., Rosen, J. M., 2007. Estrogen regulation of mammary gland development and breast cancer: amphiregulin takes center stage. Breast Cancer Res. 9**,** 304.

Larsen, P. R., et al., The Thyroid Gland. In: J. D. Wilson, et al., Eds.), Williams' Textbook of Endocrinology, 9th Edition. W.B. Saunders Company, Philadelphia, 1998, pp. 389-515.

Lavayssiere, R., et al., 2009. Positron Emission Tomography (PET) and breast cancer in clinical practice. Eur J Radiol. 69**,** 50-8.

Lawson, J. S., 2009. Do viruses cause breast cancer? Methods Mol Biol. 471**,** 421-38.

Lawson, J. S., et al., 2001. From Bittner to Barr: a viral, diet and hormone breast cancer aetiology hypothesis. Breast Cancer Res. 3**,** 81-5.

Levy, O., et al., 1998. N-linked glycosylation of the thyroid Na+/I- symporter (NIS). Implications for its secondary structure model. J Biol Chem. 273**,** 22657-63.

Li, J., et al., 1995. Maximum likelihood reconstruction for pinhole SPECT with adisplaced center-of-rotation. IEEE Transactions on Medical Imaging. 14**,** 407-409.

Liang, H., et al., 2007. A microPET/CT system for in vivo small animal imaging. Phys Med Biol. 52**,** 3881-94.

Liao, D., et al., 2007. Hypoxia-inducible factor-1alpha is a key regulator of metastasis in a transgenic model of cancer initiation and progression. Cancer Res. 67**,** 563-72.

Lijowski, M., et al., 2009. High sensitivity: high-resolution SPECT-CT/MR molecular imaging of angiogenesis in the Vx2 model. Invest Radiol. 44**,** 15-22.

Lin, E. Y., et al., 2003. Progression to malignancy in the polyoma middle T oncoprotein mouse breast cancer model provides a reliable model for human diseases. Am J Pathol. 163**,** 2113-26.

Liu, G., et al., 2008. Pretargeting CWR22 prostate tumor in mice with MORF-B72.3 antibody and radiolabeled cMORF. Eur J Nucl Med Mol Imaging. 35**,** 272-80.

Lyons, S. K., 2005. Advances in imaging mouse tumour models in vivo. J Pathol. 205**,** 194-205.

Maglione, J. E., et al., 2001. Transgenic Polyoma middle-T mice model premalignant mammary disease. Cancer Res. 61**,** 8298-305.

Mandl, S. J., et al., 2004. Multi-modality imaging identifies key times for annexin V imaging as an early predictor of therapeutic outcome. Mol Imaging. 3**,** 1-8.

Marcotte, R., Muller, W. J., 2008. Signal transduction in transgenic mouse models of human breast cancer--implications for human breast cancer. J Mammary Gland Biol Neoplasia. 13**,** 323-35.

Mariani, G., et al., 2008. Is PET always an advantage versus planar and SPECT imaging? Eur J Nucl Med Mol Imaging. 35**,** 1560-5.

Matveeva, N., et al., 2009. Guidelines for high quality mammography screening. Prilozi. 29**,** 345-54.

Mavi, A., et al., 2007. The effects of estrogen, progesterone, and C-erbB-2 receptor states on 18F-FDG uptake of primary breast cancer lesions. J Nucl Med. 48**,** 1266-72.

Mavi, A., et al., 2006. Dual time point 18F-FDG PET imaging detects breast cancer with high sensitivity and correlates well with histologic subtypes. J Nucl Med. 47**,** 1440-6.

McBryan, J., et al., 2008. Amphiregulin: Role in Mammary Gland Development and Breast Cancer. J Mammary Gland Biol Neoplasia.

McElroy, D. P., et al., 2002. Performance evaluation of A-SPECT: a high resolution desktop pinhole SPECT system for imaging small animals. IEEE Transactions on Nuclear Science. 49**,** 2139-2147.

Medina, D., 2005. Mammary developmental fate and breast cancer risk. Endocr Relat Cancer. 12**,** 483-95.

Meikle, S. R., et al., 2005. Small animal SPECT and its place in the matrix of molecular imaging technologies. Phys Med Biol. 50**,** R45-61.

Meikle, S. R., et al., 2002. A prototype coded aperture detector for small animal SPECT. IEEE Transactions on Nuclear Science. 49**,** 2167-2171.

Mester, J., et al., 1987. Activation of int-1 and int-2 mammary oncogenes in hormone-dependent and -independent mammary tumors of GR mice. J Virol. 61**,** 1073-8.

Metcalfe, K. A., 2009. Oophorectomy for breast cancer prevention in women with BRCA1 or BRCA2 mutations. Womens Health (Lond Engl). 5**,** 63-8.

Michalides, R., et al., 1981. Mammary tumor virus proviral DNA in normal murine tissue and non-virally induced mammary tumors. J Virol. 39**,** 367-76.

Mink, S., et al., 1992. A mammary cell-specific enhancer in mouse mammary tumor virus DNA is composed of multiple regulatory elements including binding sites for CTF/NFI and a novel transcription factor, mammary cell-activating factor. Mol Cell Biol. 12**,** 4906-18.

Mitchell, G. S., Cherry, S. R., 2009. A high-sensitivity small animal SPECT system. Phys Med Biol. 54**,** 1291-1305.

Mok, E., et al., 1992. A mouse mammary tumor virus mammary gland enhancer confers tissue-specific but not lactation-dependent expression in transgenic mice. J Virol. 66**,** 7529-32.

Moon, D. H., et al., 2001. Correlation between 99mTc-pertechnetate uptakes and expressions of human sodium iodide symporter gene in breast tumor tissues. Nucl Med Biol. 28**,** 829-34.

Moon, H. G., et al., 2009. Age and HER2 expression status affect MRI accuracy in predicting residual tumor extent after neo-adjuvant systemic treatment. Ann Oncol. 20**,** 636-41.

Mortellaro, V. E., et al., 2009. Magnetic resonance imaging for axillary staging in patients with breast cancer. J Magn Reson Imaging.

Nayak, T. K., et al., 2008. Preclinical development of a neutral, estrogen receptor-targeted, tridentate 99mTc(I)-estradiol-pyridin-2-yl hydrazine derivative for imaging of breast and endometrial cancers. J Nucl Med. 49**,** 978-86.

Nevanlinna, H., Bartek, J., 2006. The CHEK2 gene and inherited breast cancer susceptibility. Oncogene. 25**,** 5912-9.

Normanno, N., et al., 1995. Expression of messenger RNA for amphiregulin, heregulin, and cripto-1, three new members of the epidermal growth factor family, in human breast carcinomas. Breast Cancer Res Treat. 35**,** 293-7.

Nusse, R., et al., 1984. Mode of proviral activation of a putative mammary oncogene (int-1) on mouse chromosome 15. Nature. 307**,** 131-6.

Nuyts, J., et al., 2009. Small animal imaging with multi-pinhole SPECT. Methods.

Ohashi, E., et al., 2009. Activation of the PI3 kinase pathway by retinoic acid mediates sodium/iodide symporter induction and iodide transport in MCF-7 breast cancer cells. Cancer Res. 69**,** 3443-50.

Orlova, A., et al., 2007. Pre-clinical evaluation of [111In]-benzyl-DOTA-Z(HER2:342), a potential agent for imaging of HER2 expression in malignant tumors. Int J Mol Med. 20**,** 397-404.

Ostendorf, B., et al., 2006. High-resolution multipinhole single-photon-emission computed tomography in experimental and human arthritis. Arthritis Rheum. 54**,** 1096-104.

Otten, A. D., et al., 1988. The MMTV LTR promoter is induced by progesterone and dihydrotestosterone but not by estrogen. Mol Endocrinol. 2**,** 143-7.

Parry, J. J., et al., 2009. PET imaging of heat-inducible suicide gene expression in mice bearing head and neck squamous cell carcinoma xenografts. Cancer Gene Ther. 16**,** 161-70.

Peremans, K., et al., 2005. A review of small animal imaging planar and pinhole spect Gamma camera imaging. Vet Radiol Ultrasound. 46**,** 162-70.

Perron, B., et al., 2001. Cloning of the mouse sodium iodide symporter and its expression in the mammary gland and other tissues. J Endocrinol. 170**,** 185-96.

Peterson, L. M., et al., 2008. Quantitative imaging of estrogen receptor expression in breast cancer with PET and 18F-fluoroestradiol. J Nucl Med. 49**,** 367-74.

Pissarek, M. B., et al., 2008. Challenge by the murine brain: multi-pinhole SPECT of 123I-labelled pharmaceuticals. J Neurosci Methods. 168**,** 282-92.

Politi, K., et al., 2004. Notch in mammary gland development and breast cancer. Semin Cancer Biol. 14**,** 341-7.

Ponta, H., et al., 1985. Mouse mammary tumour virus: a proviral gene contributes to the understanding of eukaryotic gene expression and mammary tumorigenesis. J Gen Virol. 66 (Pt 5), 931-43.

Postiglione, M. P., et al., 2002. Role of the thyroid-stimulating hormone receptor signaling in development and differentiation of the thyroid gland. Proc Natl Acad Sci U S A. 99, 15462-7.

Prasad, S. N., Houserkova, D., 2007. The role of various modalities in breast imaging. Biomed Pap Med Fac Univ Palacky Olomouc Czech Repub. 151, 209-18.

Pritchard, K. I., et al., 2008. HER-2 and topoisomerase II as predictors of response to chemotherapy. J Clin Oncol. 26, 736-44.

Pylayeva, Y., et al., 2009. Ras- and PI3K-dependent breast tumorigenesis in mice and humans requires focal adhesion kinase signaling. J Clin Invest. 119, 252-66.

Qian, J., et al., 2008. A small-animal imaging system capable of multipinhole circular/helical SPECT and parallel-hole SPECT. Nuclear Instruments and Methods in Physics Research Section A: Accelerators, Spectrometers, Detectors and Associated Equipment. 594, 102-110.

Rahmim, A., Zaidi, H., 2008. PET versus SPECT: strengths, limitations and challenges. Nucl Med Commun. 29, 193-207.

Renier, C., et al., 2009. Endogenous NIS Expression in Triple-Negative Breast Cancers. Ann Surg Oncol.

Robinson, J. D., et al., 2008. Breast cancer in men: a need for psychological intervention. J Clin Psychol Med Settings. 15, 134-9.

Ronckers, C. M., et al., 2006. Thyroid cancer in childhood cancer survivors: a detailed evaluation of radiation dose response and its modifiers. Radiat Res. 166, 618-28.

Ross, S. R., 2008. MMTV Infectious Cycle and the Contribution of Virus-encoded Proteins to Transformation of Mammary Tissue. J Mammary Gland Biol Neoplasia.

Ross, S. R., et al., 2002. Mouse transferrin receptor 1 is the cell entry receptor for mouse mammary tumor virus. Proc Natl Acad Sci U S A. 99, 12386-90.

Rowland, D. J., Cherry, S. R., 2008. Small-animal preclinical nuclear medicine instrumentation and methodology. Semin Nucl Med. 38, 209-22.

Saha, M. S., et al., 2003. Incorporation of a fluoroscopic X-ray Modality in a small animal imaging system. IEEE Transactions on Nuclear Science. 50, 333-38.

Sawitzke, A. L., et al., 1988. A comparison of thyroid function in DBA/2J and C57BL/6J mice. Epilepsia. 29, 514-22.

Schipper, M. L., et al., 2007. Efficacy of 99mTc pertechnetate and 131I radioisotope therapy in sodium/iodide symporter (NIS)-expressing neuroendocrine tumors in vivo. Eur J Nucl Med Mol Imaging. 34, 638-50.

Schottelius, M., et al., 2009. Ligands for Mapping alpha(v)beta(3)-Integrin Expression in Vivo. Acc Chem Res.

Schramm, N. U., et al., 2003. High-resolution SPECT using multipinhole collimation. IEEE Transactions on Nuclear Science. 50, 315-320.

Semenza, G. L., 2003. Targeting HIF-1 for cancer therapy. Nat Rev Cancer. 3, 721-32.

Shackleford, G. M., et al., 1993. Mouse mammary tumor virus infection accelerates mammary carcinogenesis in Wnt-1 transgenic mice by insertional activation of int-2/Fgf-3 and hst/Fgf-4. Proc Natl Acad Sci U S A. 90**,** 740-4.

Siddon, R. L., 1985. Fast calculation of the exact radiological path for a three-dimensional CT array. Med. Phys. 12**,** 252-55.

Sillitoe, R. V., Hawkes, R., 2002. Whole-mount immunohistochemistry: a high-throughput screen for patterning defects in the mouse cerebellum. J Histochem Cytochem. 50**,** 235-44.

Skaane, P., 2009. Studies comparing screen-film mammography and full-field digital mammography in breast cancer screening: updated review. Acta Radiol. 50**,** 3-14.

Smanik, P. A., et al., 1997. Expression, exon-intron organization, and chromosome mapping of the human sodium iodide symporter. Endocrinology. 138**,** 3555-8.

Song, E., et al., 2009. Breast Mass Segmentation in Mammography Using Plane Fitting and Dynamic Programming(1). Acad Radiol.

Spanu, A., et al., 2009. 131I SPECT/CT in the follow-up of differentiated thyroid carcinoma: incremental value versus planar imaging. J Nucl Med. 50**,** 184-90.

Spitzweg, C., Morris, J. C., 2002. The sodium iodide symporter: its pathophysiological and therapeutic implications. Clin Endocrinol (Oxf). 57**,** 559-74.

Stein, T., et al., 2009. A mouse mammary gland involution mRNA signature identifies biological pathways potentially associated with breast cancer metastasis. J Mammary Gland Biol Neoplasia. 14**,** 99-116.

Szinnai, G., et al., 2007. Sodium/iodide symporter (NIS) gene expression is the limiting step for the onset of thyroid function in the human fetus. J Clin Endocrinol Metab. 92**,** 70-6.

Tazebay, U. H., et al., 2000. The mammary gland iodide transporter is expressed during lactation and in breast cancer. Nat Med. 6**,** 871-8.

Theodorou, V., et al., 2007. MMTV insertional mutagenesis identifies genes, gene families and pathways involved in mammary cancer. Nat Genet. 39**,** 759-69.

Tiling, R., et al., 2004. Tissue-specific effects on uptake of 99mTc-sestamibi by breast lesions: a targeted analysis of false scintigraphic diagnoses. J Nucl Med. 45**,** 1822-8.

Tozaki, M., 2008. Proton MR spectroscopy of the breast. Breast Cancer.

Travaini, L. L., et al., 2007. Neoadjuvant therapy in locally advanced breast cancer: 99mTc-MIBI mammoscintigraphy is not a reliable technique to predict therapy response. Breast. 16**,** 262-70.

Unterholzner, S., et al., 2006. Dexamethasone stimulation of retinoic Acid-induced sodium iodide symporter expression and cytotoxicity of 131-I in breast cancer cells. J Clin Endocrinol Metab. 91**,** 69-78.

Upadhyay, G., et al., 2003. Functional expression of sodium iodide symporter (NIS) in human breast cancer tissue. Breast Cancer Res Treat. 77**,** 157-65.

Uyttendaele, H., et al., 1996. Notch4/int-3, a mammary proto-oncogene, is an endothelial cell-specific mammalian Notch gene. Development. 122**,** 2251-9.

van der Have, F., et al., 2009. U-SPECT-II: An Ultra-High-Resolution Device for Molecular Small-Animal Imaging. J Nucl Med. 50**,** 599-605.

van der Have, F., et al., 2008. System calibration and statistical image reconstruction for ultra-high resolution stationary pinhole SPECT. IEEE Transactions on Medical Imaging. 27**,** 960-971.

Vanhove, C., et al., 2008. Three-pinhole collimator to improve axial spatial resolution and sensitivity in pinhole SPECT. Eur J Nucl Med Mol Imaging. 35**,** 407-15.

Varmus, H. E., et al., 1972. Mammary tumour virus specific nucleotide sequences in mouse DNA. Nat New Biol. 238**,** 189-91.

Vinnicombe, S., et al., 2009. Full-field digital versus screen-film mammography: comparison within the UK breast screening program and systematic review of published data. Radiology. 251**,** 347-58.

Vivanco, I., Sawyers, C. L., 2002. The phosphatidylinositol 3-Kinase AKT pathway in human cancer. Nat Rev Cancer. 2**,** 489-501.

Wahl, R. L., et al., 2009. From RECIST to PERCIST: Evolving Considerations for PET Response Criteria in Solid Tumors. J Nucl Med. 50**,** 122S-150S.

Wang, S., et al., 2009. Disruption of the SRC-1 gene in mice suppresses breast cancer metastasis without affecting primary tumor formation. Proc Natl Acad Sci U S A. 106**,** 151-6.

Wapnir, I. L., et al., 2004. The Na+/I- symporter mediates iodide uptake in breast cancer metastases and can be selectively down-regulated in the thyroid. Clin Cancer Res. 10**,** 4294-302.

Wapnir, I. L., et al., 2003. Immunohistochemical profile of the sodium/iodide symporter in thyroid, breast, and other carcinomas using high density tissue microarrays and conventional sections. J Clin Endocrinol Metab. 88**,** 1880-8.

Wei, S., et al., 2009. Estrogen and Progesterone Receptor Expression is not Always Specific for Mammary and Gynecologic Carcinomas: A Tissue Microarray and Pooled Literature Review Study. Appl Immunohistochem Mol Morphol.

Weisenberger, A. G., et al., 1998. Design features and performance of a CsI(Na) array based gamma camera for small animal gene research. IEEE Transactions on Nuclear Science. 45**,** 3053-58.

Weisenberger, A. G., et al., 2003. SPECT-CT system for small animal imaging. IEEE Transactions on Nuclear Science. 50**,** 74-9.

Willhauck, M. J., et al., 2008. Functional sodium iodide symporter expression in breast cancer xenografts in vivo after systemic treatment with retinoic acid and dexamethasone. Breast Cancer Res Treat. 109**,** 263-72.

Zhou, M., et al., 2008. Real-world application of breast-specific gamma imaging, initial experience at a community breast center and its potential impact on clinical care. Am J Surg. 195**,** 631-5; discussion 635.

Zhung, H., Alavi, A., 2002. Fluorodeoxyglucose positron emission tomographic imaging in the detection and monitoring of infection and inflammation. Semin Nucl Med. 32**,** 47-59.

Zuckier, L. S., et al., 2001. The endogenous mammary gland Na(+)/I(-) symporter may mediate effective radioiodide therapy in breast cancer. J Nucl Med. 42**,** 987-8.

Zuckier, L. S., et al., 2004. Kinetics of perrhenate uptake and comparative biodistribution of perrhenate, pertechnetate, and iodide by NaI symporter-expressing tissues in vivo. J Nucl Med. 45**,** 500-7.

Zytoon, A. A., et al., 2008. Breast cancer with low FDG uptake: Characterization by means of dual-time point FDG-PET/CT. Eur J Radiol.

VITA

The author, Randall Eric Blue, was born on October 29, 1982 in Lumberton, North Carolina. He is also a member of the Lumbee Tribe of North Carolina, which is the largest Native American tribe to the east of the Mississippi River. Randall Eric Blue attended Purnell Swett High School in Pembroke, North Carolina and graduated as Valedictorian in 2001. He received his B.S. degree in Biology along with a Chemistry minor at the University of North Carolina at Chapel Hill in 2005.

The author was accepted into the College of William and Mary as a M.S. candidate in the Biology Department in August of 2006. During his term as a M.S. candidate Randall Eric Blue was a research assistant for Dr. Eric Bradley and Dr. Margaret Saha. Additionally, he had the opportunity to become a teaching assistant for the Biology Department. With the completion of this thesis and satisfaction of all other degree requirements, Randall Eric Blue received his M.S. degree in Biology in August 2009.